Master Thesis, Department of Geosciences

Development of photogrammetric methods for landslide analysis

Greg Saunders

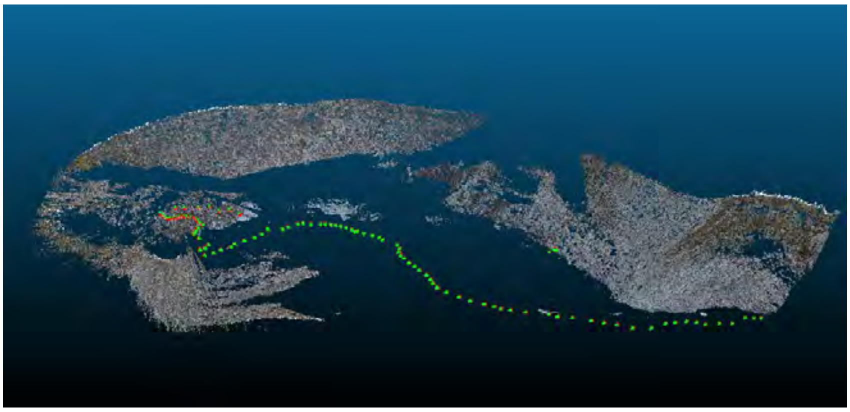

UNIVERSITY OF OSLO
FACULTY OF MATHEMATICS AND NATURAL SCIENCES

UNIVERSITY OF OSLO

MASTER'S THESIS

Development of photogrammetric methods for landslide analysis

Developing an Efficient Method to Create 3-Dimensional Models of Landslide Tracks

---

Author:
Greg SAUNDERS

Supervisor:
Dr. Karen MAIR

Co-Supervisor:
Dr. Olivier GALLAND

A thesis submitted in fulfilment of the requirements
for the degree of Master of Science

in the

Physics of Geological Processes
Institutt for Geofag

November 2014

UNIVERSITY OF OSLO

Abstract

Det matematisk-naturvitenskapelige fakultet
Institutt for Geofag

Master of Science

Development of photogrammetric methods for landslide analysis

by Greg SAUNDERS

This thesis assesses the accuracy and repeatability different image capture and analytical methods for photogrammetric analysis of landslides. An open source software called MicMac was used to create point clouds and orthoimages. Data from two sets of aerial surveys of a scree slope near Oslo, Norway act as the main data sets. The surveys took place a year apart. Different cameras and image capture methods were used. Despite the different methods, sub pixel accuracy was achieved when matching point clouds. The orthoimages were similar, but not as accurate as the point clouds. The orthoimages showed movement up to 31 cm/year in an area believed to be stable.

Grain size analysis was carried out to determine the quality of the orthoimages and point clouds. A clear relation between image resolution and particle size distribution was found. The higher the resolution the lower the particle size. A defined relationship has not been defined as more data is needed. A workflow has been set up for automated grain size analysis.

Preliminary surveys have been completed at a glacially dammed lake in the Fjaerland region of Norway. These surveys serve as a possible next step for this project.

Acknowledgements

I have too many people to thanks, so I'll just keep this short and sweet. First off I would like to thank my advisors Olivier Galland and Karen Mair for putting up with me and always encouraging me regardless of the situation.

Thanks to everyone who helped me with my thesis; Deuts for feeding me, Rikke for putting up with sitting next to me, Lis and Mirsini for waking me up when I needed to, and all my fellow students in PGP for providing laughs and good times. Especially Jen Porter for keeping me motivated and on the right track. Thanks for teaching me your loonie version of English. A big thanks to Luc and Boris for help with the field work, and Luc again for your help with MicMac.

I would like to acknowledge the Norwegian Glacier Museum and Paal Kjelland for helping me around Fjaerland.

And most importantly I need to thanks my family and friends. Without you all this would be impossible. Especially my mom, dad, and brother.

Greg Saunders

Contents

List of Figures

Chapter 1

Introduction

This thesis is focused on creating an efficient and robust method for analyzing landslide characteristics with photogrammetric analysis. Photogrammetry is the process of reconstructing 3-dimensional scenes from image data (Schenk, 2005). The drastic improvements in imaging and computer power in the recent years are opening up new doorways for scientific analysis. Traditional methods of landslide analysis required the acquisition of physical measurements in potentially harmful environments. The ability to safely collect high-resolution topographic data at little to no cost is making it possible to more accurately monitor the world around us.

Landslide research has benefited immensely from the advent of 3d modeling. More and more studies on landslide movement use 3D maps to determine regions of movement and potential hazard (Travelletti and Malet, 2010). Photogrammetry is not the only method for creating 3 dimensional maps over selected regions. Methods such as range imaging (Nitsche et al., 2013) and laser scanning (Bitelli et al. (2003),Heritage and Milan (2009),Goor (2011)) are also common. Research done with these modeling techniques gives insight into what is possible with photogrammetry. Unlike these methods; however, photogrammetry requires little equipment and surveys can be completed with minimal training.

Methods of landslide monitoring discussed in this thesis are based around grains size analysis and reproducibility. The size and shape of grains in a scree slope can potentially provide information on past slide dynamics. Temporal monitoring is extremely important in landslide monitoring. By testing various cameras and capture methods this study aims at finding limitations and advantages associated with photogrammetry. Taking these limitations into account, the end goal is to create a repeatable workflow for start to finish photogrammetric analysis.

Chapter 2

Background

This chapter will cover information needed for understanding the processes, methods, and motivation for this thesis.

2.1 Landslides

2.1.1 Definition

Landslides are defined as the downward movement of rock or soil due to gravity. They must also have a density at least 10% higher than the density of water (Blasio, 2011). Studying landslides is important for safety and economic reasons. People build and live in locations where sliding can and will occur. The risk is both in potential lives lost and infrastructure damage (Varnes, 1984). Varnes (1984) set the total risk for a region in terms of the vulnerability, natural hazard, specific risk and elements at risk. This classification of risk has been used and adapted and modified ever since (Westen et al., 2005). Understanding the processes and mechanics involved in landslide movement will help create a more accurate risk assessment. Forecasting the time of failure and the areas susceptible to damage is crucial in completing a proper risk analysis.

2.1.2 Basic mechanics

It is important to be able to classify the stability of a slope (Blasio, 2011). The factor of safety (F) is used for this (Equation 2.1). Figure 2.1 illustrates the basic landslide mechanical processes. The weight of the block is a vertical force. This force is broken down into a normal force and a driving force. The normal force acts normal to the failure plane and is used to calculate the friction (resisting force). In addition, cohesion and man-made devices can add to the resisting force. The driving force is the force parallel to the slope as seen in Figure 2.1.

$$\mathrm{F} = \frac{\text{resisting forces}}{\text{driving forces}} \tag{2.1}$$

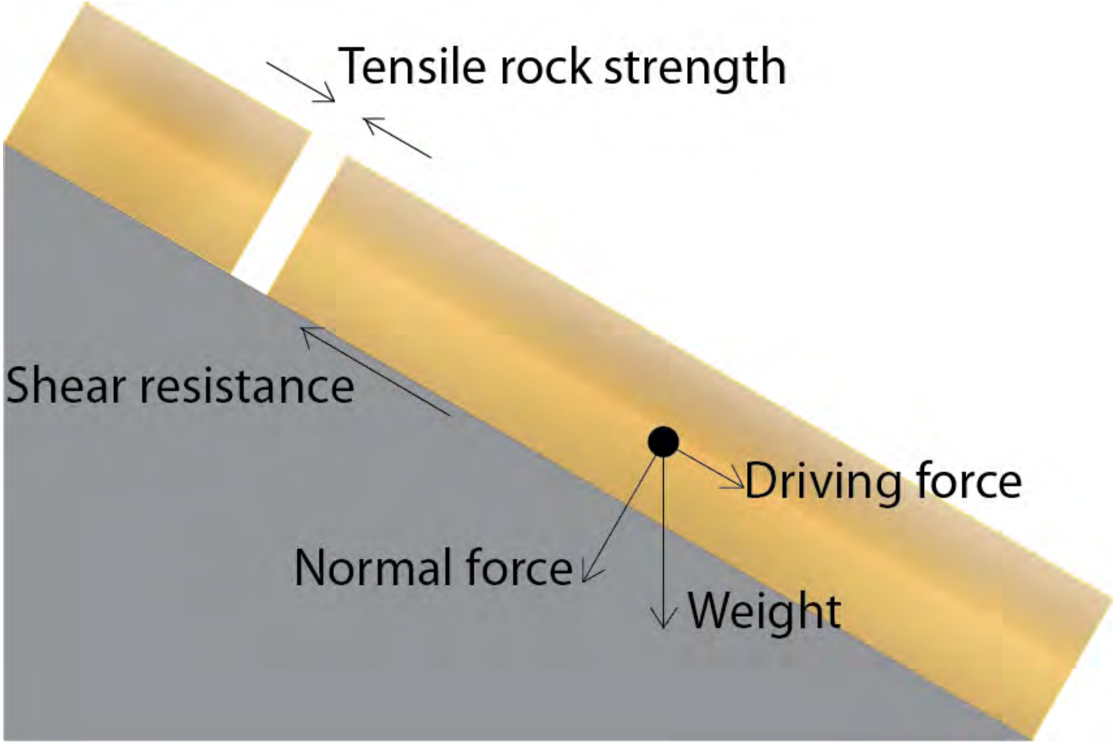

Figure 2.1: Simplified free body diagram of forces involved in landslides. The weight of the block is divided into a normal force on the sliding plane and a driving force. The normal force is used in calculating the frictional resisting force (shear resistance). The tensile strength of the rock can also be a factor.

In a dynamic loading situation there is a point at which the resisting force becomes less than the driving force and slope failure occurs. This is the same as a book beginning to slide on an increasingly inclined table. There is no movement until a certain angle is reached, after which failure occurs and the book begins to slide. However, in complex slides this is not the case. Complex landslides can exhibit small movements known as creep over a longer period of time (Blasio, 2011).

Detection of this creep has been the focus of numerous studies. Temporal data of creep movement makes it possible to set an estimate for when a landslide may occur (Komamura and Yamamori, 1988). Velocity exponentially increases as the slide begins to fail (Fig. 2.2). Komamura and Yamamori (1988) monitored the increasing velocity by using scaled laboratory experiments. Field monitoring of active slides by Petley (2004) confirms the laboratory results, as well as illustrates the effect of pore pressure on movement (Fig. 2.3). Further study of landslide creep presented in Petley et al.

(2005) suggests four different stages of landslide movement (Fig. 2.2). The stages of landslide movement can change from one landslide to another. Xu et al. (2011) suggest three phases instead of four stages. The differences in nomenclature are apparent, but both studies agree that movement accelerates up to the failure point.

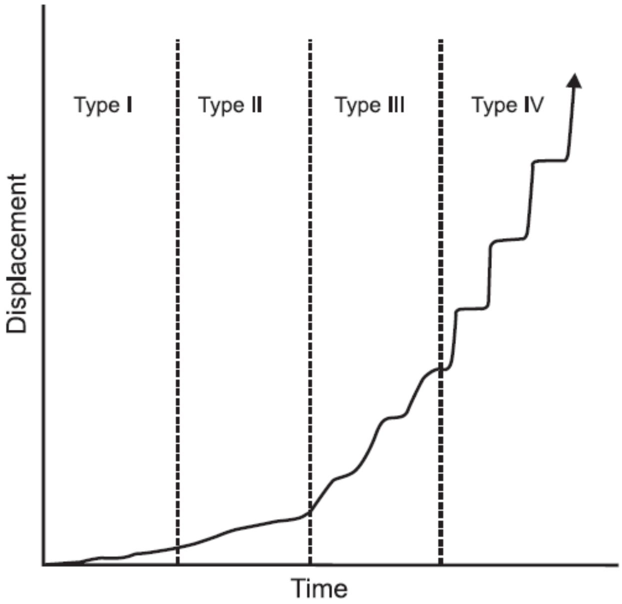

Figure 2.2: Graph of landslide movement with respect to time from Petley et al. (2005). The four "Types" represent four distinct stages in landslide movement. This curve represents the idealized movement of a landslide overtime. It was created from monitoring lab experiments.

Research is currently being conducted on active slides around the world. One such slide is the Aaknes slide in Norway (Oppikofer, 2009). The slide overlies the Tafjord fjord. A failure of the rock-mass could potentially result in a deadly tsunami. State of the art monitoring systems have been put in place to monitor this slide. With proper forecasting, lives and infrastructure can be saved.

The occurrence of landslide and rockfall events around the world and the associated hazards creates a need for research on the controlling mechanics and processes. Research has been completed on both macro and micro scales. The techniques, as presented in this thesis, are aimed at creating an accessible and repeatable method for monitoring potential slide movement and extracting data from 3-dimensional models of debris and landslide tracks.

2.2 Monitoring

In-field monitoring is crucial for determining the present state of a landslide (Angeli et al., 2000). Movement must be monitored at different points of the active sliding area

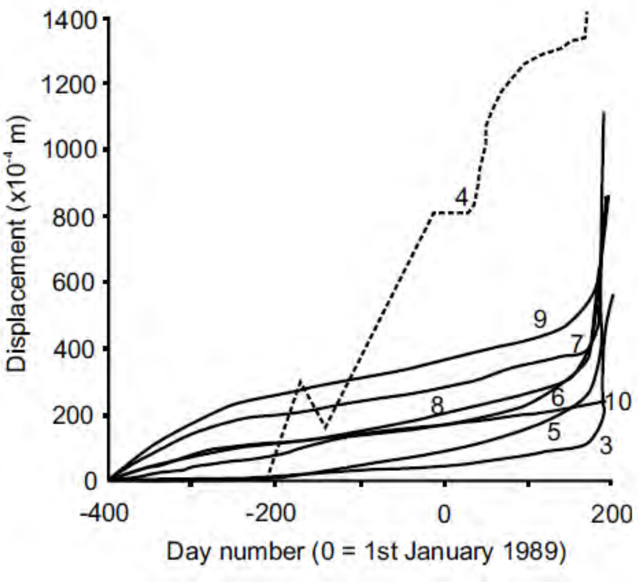

Figure 2.3: Graph of landslide movement with respect to time from Petley (2004). The data show the same exponential growth seen in Figure. 2.2. 0 time represents the initiation of pore pressure recharge in the environment. The lines represent data from equally spaced inclinometers from the top (3) to the bottom (10) of a slope. Line 4 shows great variation due to non-discussed reasons (Petley, 2004).

to determine the general movement of the slide. Frequency and position of monitoring stations proved important in field studies presented in Angeli et al. (2000). Cruden and Masoumzadeh (1987) show the necessity of real-time monitoring in order to predict failures of a coal mine. The positioning and coverage of physical monitoring stations proved to be a problem in Angeli et al. (2000) due to weight and access issues.

Remote analysis of landslide features allows for safe data collection. One method of acquiring remote data is by satellite as in Eckardt et al. (2009) and Pierrot-Deseilligny and Paparoditis (2006). These papers describe the resolution and accuracy of satellites for mapping surface features. A problem with this method can be the resolution. While satellites may be good for covering large regions, they may not have high enough resolution for accurately mapping small regions.

Abellán et al. (2009) discusses the advantages of terrestrial laser scanning (TLS) for landslide monitoring by showing the detection of millimetric deformation. Photogrammetric analysis of landslide events is proving to be capable of producing 3 dimensional point-clouds as robust as laser scanning Bitelli et al. (2003). Point-cloud analysis methods associated with laser scanning can potentially be used with photogrammetric data analysis. Comparison between the two methods has been an important part of numerous articles in the last 10 years (Lato and Vöge (2012), Bitelli et al. (2003), Lato et al. (2013), Corsini et al. (2009), Hodge et al. (2009), and Tonon and Kottenstette (2006)).

Thus it is important to explain the applications and problems associated with laser scanning to understand the potential power of photogrammetry. Physical monitoring must also be discussed as non-intrusive methods such as photogrammetry and TLS cannot completely replace physical measurements.

2.2.1 Physical monitoring

Measurement of landslide movement has long used physical monitoring systems. These systems are placed on the active sliding area to monitor movements. Physical monitoring of landslides provides immediate data relating to movement and size. The problem with this is the need for numerous data points to obtain an overview of a landslide's movement. For each data point a separate monitoring system must be used. Dense data surveys can become expensive. Additionally, the danger of physically placing the monitoring systems must also be taken into account.

Typical instruments used to monitor landslide movements are extensometers, inclinometers, and piezometers. Extensometers measure extension between a fixed point and a point on the active slide. Inclinometers, which measure changes in inclination, need to be installed in drill holes in the active slide. The data shows the slide dynamics at depth. Piezometers are used to determine water content. The data from extensometers and inclinometers can be determined using either TLS or photogrammetry. The data from piezometers cannot be collected from non-intrusive methods (Wieczorek and Snyder, 2009). There are other monitoring techniques for monitoring landslides, but like piezometers most other measurements require physical contact. This thesis focuses on remotely captured data.

2.2.2 Satellite

ADD STUFF HERE SOOOOOON

2.2.3 Terrestrial laser scanning

TLS uses a laser scanner to determine accurate source to feature distances. The output of a laser scan in a point-cloud composed of (x,y,z) coordinates. As noted by Abellán et al. (2009), TLS provides a comprehensive method of categorizing landslide movement and that further validation was required to ensure correct results. Other studies around world have been completed using TLS as a data source (Abellán et al. (2011), Lato et al. (2010), Buckley et al. (2008), and Heritage and Milan (2009)). This is a very short list of past TLS use in the geological setting. The main conclusion is that TLS provides an accurate method to collect data on static field areas from a safe distance. This is crucial as often physical measurements can be dangerous or difficult to complete (Lato et al., 2010).

One drawback commonly associated with TLS is line of sight (Fig. 2.4). This is a problem which occurs when the TLS scans a scene and misses data due to objects in the foreground. This can be rectified by using multiple scan locations, but this additional scanning takes time.

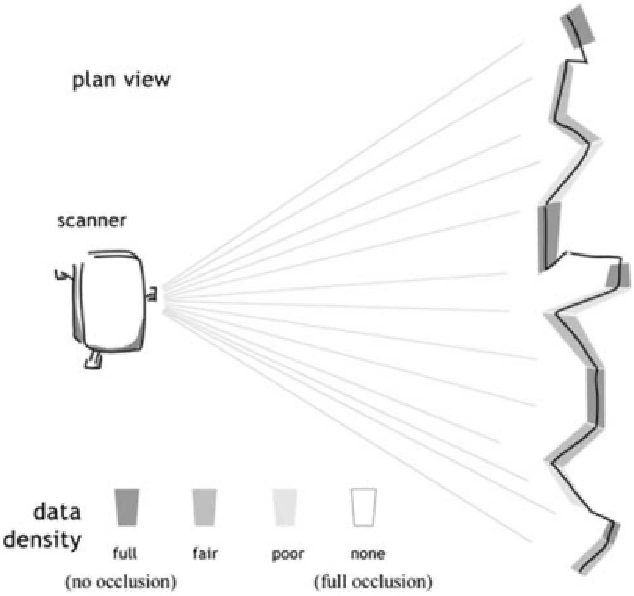

Figure 2.4: Diagram showing potential problems associated with a stationary scanning position. The line on the right represents a cross-section of a surface to be scanned. The varying darkness of the shading around the line represents data quality. For rough surfaces the quality of data decreases. Figure from Lato et al. (2010)

TLS has advantages and disadvantages. Some advantages of TLS are: the immediate construction of a point-cloud which can be directly analyzed, no lighting constraints on scan locations or times, and the ability to ”see” through vegetation (Bitelli et al., 2003). On the other hand, TLS systems are expensive to purchase or rent, heavy, and difficult to transport over rough terrain. They also do not allow for easy creation of orthoimages. Maximizing data coverage requires movement and the distance is limited by the specific model (Tonon and Kottenstette, 2006).

2.2.4 Photogrammetry

Photogrammetry is the process of gaining surface data from a region with use of image analysis instead of direct physical contact (Schenk, 2005). Photogrammetry uses image matching to create 3 dimensional scenes. The output is typically an orthoimage and a point-cloud. The image matching is done by triangulating points and sources from different images. The spatial relation of points between images allows for the calculation of scale invariant distances (Lowe, 2004). The concept is similar to eyesight. Acting as two cameras our eyes focus on one object. The slightly different angles of the "images" seen by out eyes allow us to estimate distance and see in 3D (Pandey, 1987).

2.2.4.1 History

Photogrammetry dates back to 1839. In the beginning, stereo photogrammetry was used. Images were taken from offset positions and viewed with stereoscopic equipment. With the invention of the airplane, this technique became more applicable. This was fine-tuned until the invention of the computer. Computational photogrammetry allowed for calculation of distances based on point matching algorithms (Schenk, 2005). The invention of digital cameras and faster computers has created the present state of photogrammetry. Processing techniques are speeding up and resolution and repeatability are increasing. The stages of photogrammetry are seen in Figure 2.5.

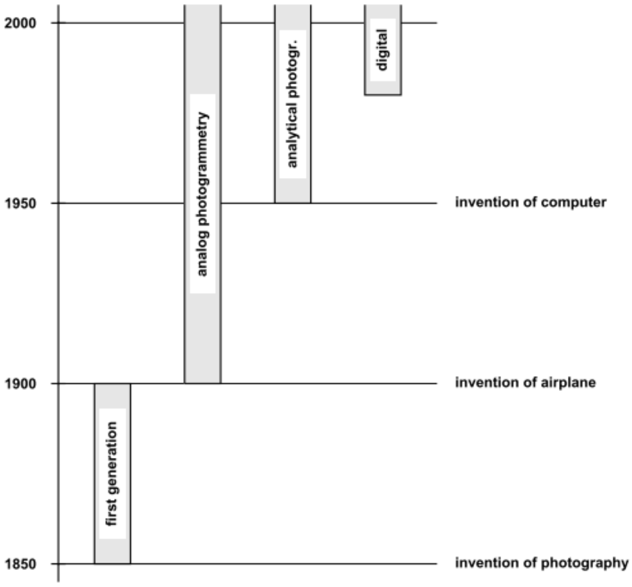

Figure 2.5: Plot showing the invention and use of different photogrammetrical methods with respect to time. Important inventions related to photogrammetric innovations are shown. Figure from Schenk (2005).

.

2.2.4.2 Applications

Photogrammetric applications are not limited to a specific field. Innovative software has been developed for various applications. Snavely et al. (2007) propose a method with which to use georeferenced images from internet photo collections to "model the world". This uses globally positioned images to reconstruct urban surface features. Accuracy is not crucial in this application. On the other side of the spectrum Koch and Kaehler (2009) describe a method of highly accurate surface reconstruction using photogrammetry and laser scanning. This technique resulted in a resolution of +/- 1 mm over a multi-meter long wall.

In landslide monitoring, photogrammetry is mainly used for two things. First, monitoring of landslide movement can use temporal photogrammetric data to track movement.. This is done by repeating surveys over time and comparing differences in the point-cloud and orthoimages. This can be read about in Bitelli et al. (2003), Mora et al. (2003), Niethammer et al. (2012), and Wieczorek and Snyder (2009). These studies cover different sized regions and image capture techniques. Second, photogrammetry is used for determining fracture orientation. This involves planar feature analysis for insitu rock faces (Lato et al. (2012),Lato et al. (2013), Wolter et al. (2014), and Collins and Stock (2012)). These studies use plane fitting algorithms to define potentially problematic joints, discontinuities, and slide planes (Collins and Stock, 2012). The advantages of photogrammetric surveys are becoming clear for their ability to increase safety and accuracy while limiting cost (Martín et al., 2013).

2.2.4.3 Grain size analysis

Aside from studies directly relating to landslides there are plenty of other applications for photogrammetric analysis in landslide-like environments. Tarolli (2014) mentions how photogrammetry and LiDAR (Light detection and ranging) can be used to monitor volcanoes, measure grain size, track morphogolical evolution, define landscapes, and evaluate engineered landscapes. Trevisani et al. (2009) describe a method for using LiDAR based digital terrain models (DTMs) to monitor surface feature characteristics of scree slopes.

Grain size analysis of riverbeds has been crucial for determining flow dynamics. River hydraulics are directly affected by grain size (Butler and Place, 2002). There are various methods for extracting grain size. The physical method of measuring specific grains in the field is time consuming. It is also difficult to gain sufficient spatial resolution. Verdú et al. (2005) used photogrammetry to create orthoimages from which textural variables and semivariograms were used to define grain size. This was calibrated using in-field measurements. The benefit of this type of study is the ability to extract accurate data from low resolution images. Buscombe (2013) used images for grain size analysis with a wavelet transform. This method does not separate specific grains, instead it uses image variations. Butler and Place (2002) combined texture operators from a digital elevation model ”DEM” and image thresholding from an orthoimage to define grain boundaries. Bertin et al. (2014) used a 3D printed gravel bed with known geometry to test photogrammetric methods. This study sets parameters for properly imaging an area to get the best results.

Further work is being done with the grain size analysis of riverbeds with laser scanning and range imaging (RIM) (Nitsche et al., 2013). With laser scanning it is possible only to use the DEM as no orthoimage is created (Hodge et al., 2009). Shadowing (Fig. 2.4) was present in this survey. The base has been set for grain size analysis of landslides and debris fields. Further study in angularity of grains and application in landslide dynamics is needed.

2.2.4.4 Structure from motion (SFM)

As mentioned above photogrammetric analysis began using analog photographs. With a minimum of two images, stereo viewing is possible. Algorithms have been created to analyze data from multiple images. The basis for these algorithms is the matching of similar feature points between images (Butler et al., 1998). With digital imagery and high power/low cost computers, research in refining these algorithms is common. Initially ground coordinates and camera coordinates were used to set parameters for image matching.

Current methods of photogrammetric bundle adjustment reconstruct scenes without the need for ground control points or camera positions (Triggs et al., 2000). The data will be scaleless The process begins with feature point selection (Pollefeys et al., 2001). Triggs et al. (2000) argue against claims of bundle adjustment being slow. This innovation makes it possible to reconstruct images from non-traditional field surveys. Analysis of imagery from handheld and UAV surveys is now both practical and accurate (Turner et al., 2012). The current use for accurate ground control points is geo-referencing to pre-existing maps, as scale can be determined by measured features or in-camera GPS.

One of the main methods in SMF analysis has been the Scale Invariant Feature Transform (SIFT) (Lowe, 2004). This method uses four steps for generating image features: Scale-space extrema detection, keypoint localization, orientation assignment, and keypoint descriptor. In short, the method selects points, orients them based on gradient directions, and sets parameters for what the point looks like when viewed from different viewpoints or illuminations (Fig. 2.6). Running systems like this can be very memory intensive, thus images are scaled down. Using an iterative process of adding keypoints and increasing resolution, position of points are determined (Lowe, 2004). When using the photogrammetry software MicMac, a modified version of SIFT (sift++) is used for extraction of tie points by default (Georgantas, 2012)

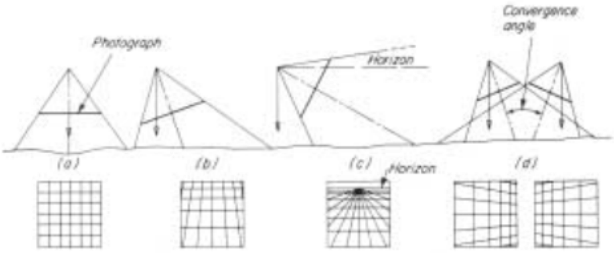

FIGURE 2.6: Diagram showing the effect of angular position on perceived image. The ground has a even grid which looks distorted from various positions. (Schenk, 1997)

For the purpose of this thesis, the details surrounding photogrammetry and SFM analysis will not be covered in great detail as it is the application of the tool which is the focus.

Chapter 3

Methods

3.1 Image capture

As mentioned in Section 2.2.4.2 there are different applications for photogrammetry. The desired accuracy of results relies on both image capture and data processing.

Resolution of an ortho-photo and density of a point-cloud are important parameters when selecting data capture and processing. Image scale is directly proportional to focal length of the camera as seen in Equation 3.1 (Burns, 1993). As seen in figure 3.1 the variables are: S=scale, f=focal length, H=flying height above datum, h=average terrain elevation, d=distance on photograph, and D=distance on ground (Burns, 1993) . The result "S" is the scale of the image. Scale is a ratio of image scale to actual scale. Focal length is typically given in mm. With digital cameras, this information is commonly stored in the exif data of an image (Snavely et al., 2007). Exif data is data stored in the image file of most digital cameras. It holds information such as, camera type, date, and time.

$$\mathrm{S} = \frac{\mathrm{f}}{\mathrm{H-h}} = \frac{\mathrm{d}}{\mathrm{D}} \tag{3.1}$$

If the desired resolution and focal length of the lens are known, the optimal imaging distance can be calculated. The processing of photogrammetric images uses the distances between tie points to triangulate the camera position and create a 3D model (Schenk, 1997). For this to work, the same points must be visible in multiple images. The amount of overlap between images is an important factor. Triggs et al. (2000) suggest that overlap between subsequent images (forward overlap) should be 50-70% and 10-20% overlap between line of images (side overlap). Additional overlap will create more data

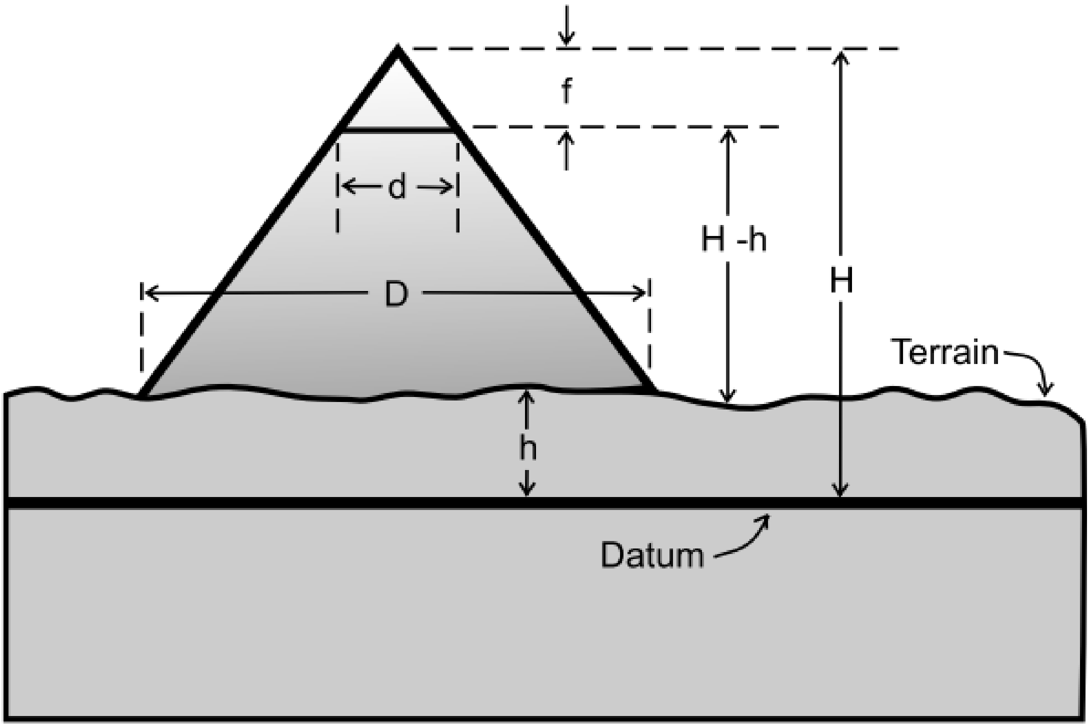

Figure 3.1: Diagram showing the variables associated with equation 3.1. The camera position is at the top of the triangle. The datum is selected by using a level lower than the lowest point on in the study area. D=ground distance, d=distance on photograph, H=height above datum, h=height of ground over datum, f=focal length. Figure from Burns (1993)

.

to analyze and longer processing times. Figure 3.2 displays a potential overlap map if both forward and side overlap were 75%

For stereo imaging, only two images are required. For digital photogrammetry analysis with the structure from motion (SFM 2.2.4.4) program MicMac, a minimum of three points must be visible in three images for georeferencing. Although this is the minimum, it is not advised. Additional images will allow for more accurate geometry reconstruction. Shooting images in a line with 75% overlap will result in 4 times overlap (Fig. 3.2). This should be seen a the minimum overlap when setting up photo surveys. Other studies use greater (Pierrot-deseilligny et al., 2011)-(80%) and lesser (Javernick et al., 2014)-(60%) is required. Pierrot-deseilligny et al. (2011) studied more angular objects than Javernick et al. (2014) so this may be a cause for the difference in suggested overlap. For the purpose of this study 75 % overlap is the goal.

It should be noted that when taking images for photogrammetry, a strict set of rules should be followed to ensure the best results (Butterworth (2012)). When photographing a region the focus, zoom, and exposure should not be changed. If the camera has an optical image stabilizer, it should be turned off. Each of these variables can cause

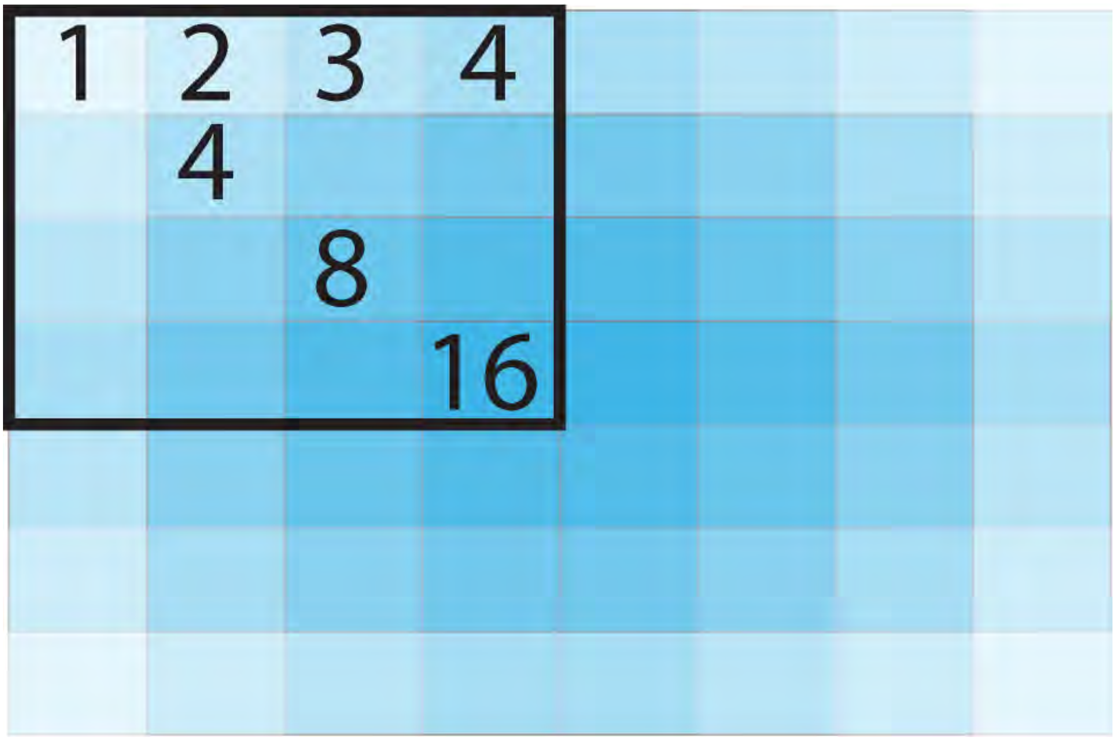

Figure 3.2: Image showing overlap between 20 images (5 horizontal x 4 vertical) taken with 25% overlap. The black box outlines the upper left image. The numbers show the increase in number of times each region has been photographed. Darker areas show greater overlap. The maximum overlap occurs near the center with 16x overlap.

problems in processing. When processing with SFM programs, such as MicMac, it is common for the program to set a fixed distortion constant for all images. A change in focus or zoom affects this distortion. The image stabilizer can potentially cause distortion as the sensor may change its position relative to the lens (Butterworth, 2012).

When photographing a planar environment, obtaining the image overlap described above will be sufficient for image capturing. This method is called aerial analysis (Fig. 3.3). For round objects or corners, a different strategy is needed. The strategy is to shoot converging images around a central image (Fig. 3.3). At least four images should be linked to each master image. Pierrot-desseilligny and Clery (2008) suggest that 15 degree rotation around central point between images allows for proper overlap.

When capturing images, it is important to note scale. This can be by measuring the distance between two points in the field (Georgantas, 2012) . This will allow for an accurate scale to be determined in the ortho-photo and point-cloud. For georeferenced scenes, ground control points (GCPs) are needed. Using SFM algorithms creates a scaleless point-cloud. By inputing GCP positions, the scaleless point-cloud can be georeferenced. This can be done in the processing steps by linking GCP location to exact pixels in images (Pierrot-Deseilligny, 2013). The user interface for MicMac warns that the accuracy of the georeferencing is dependent on accuracy in matching and final noise (Clery, 2013)

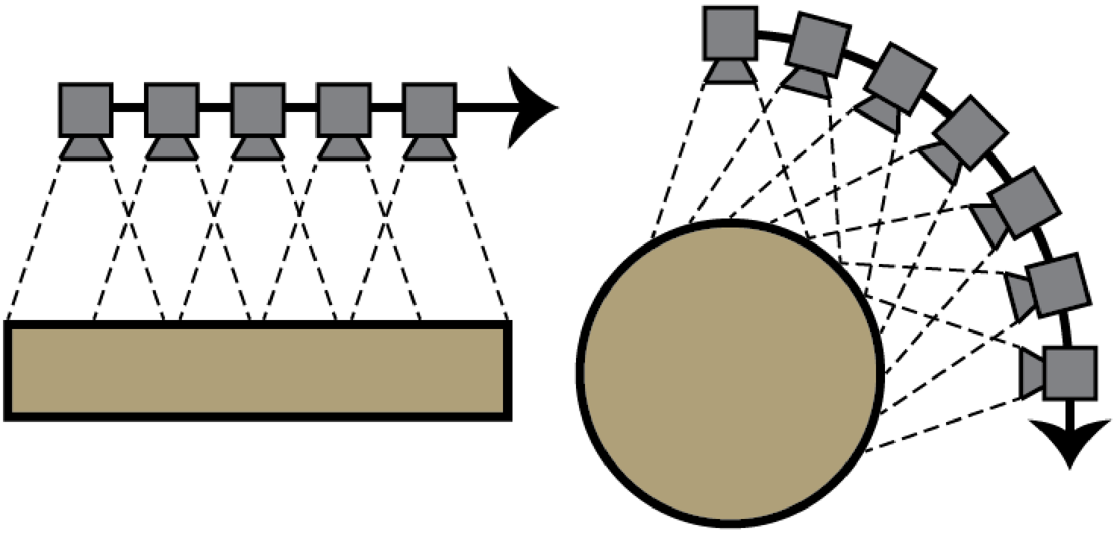

Figure 3.3: Two diagrams showing photo capture methods for photogrammetry. The camera positions are sequential in the direction of the arrow. The left is known as "Arial". Photos should be taken at a constant distance and spacing. The right is "Converging". Images are taken at a constant distance from the surface with 15 degrees of rotation of the camera between images.

Proper use of the controllable variables will increase the accuracy of the final result. There are some variables which are harder to control. Lighting can present some problems. The ideal conditions for capture are overcast. Shadows cause problems when imaging outside. Triggs et al. (2000) note that shadows may cause errors in point cloud creation. Stumpf et al. (2013) notes that, when comparing time steps from a temporal study of surface deformation, lighting condition changes make radiometric correction techniques for complex and changing surfaces difficult. Shadows also may cause problems in post processing. Yen (2003) note that strong shadows can be improperly identified as an edge using edge detection algorithms. This being said, it is important to realize the problems associated with image capture under direct sunlight.

3.2 Data organization and processing

After collection of data, it is important that it is manually organized and filtered. Organizing refers to labeling the files in logical numerical order, and filtering refers to the removal of blurry or obstructed images. The result of not doing this was noticed in a trial survey of a brick wall. One photo was blurry due to camera movement. In processing, this image was not removed from the series. This resulted in a blurred section on the ortho-image seen in Figure 3.4. If analysis of the ortho-image required a certain resolution the blurred section could cause potential problems. Additionally ,images which have high levels of vegetation may also cause a problem as the vegetation may move between images. Thd effect of vegetation on surrounding points is discussed in Javernick et al. (2014). Using MicMac images with over 75% vegetation caused processing problems. Excess vegetation once caused MicMac to crash. Images should be limited to in-focus images which cover the study region.

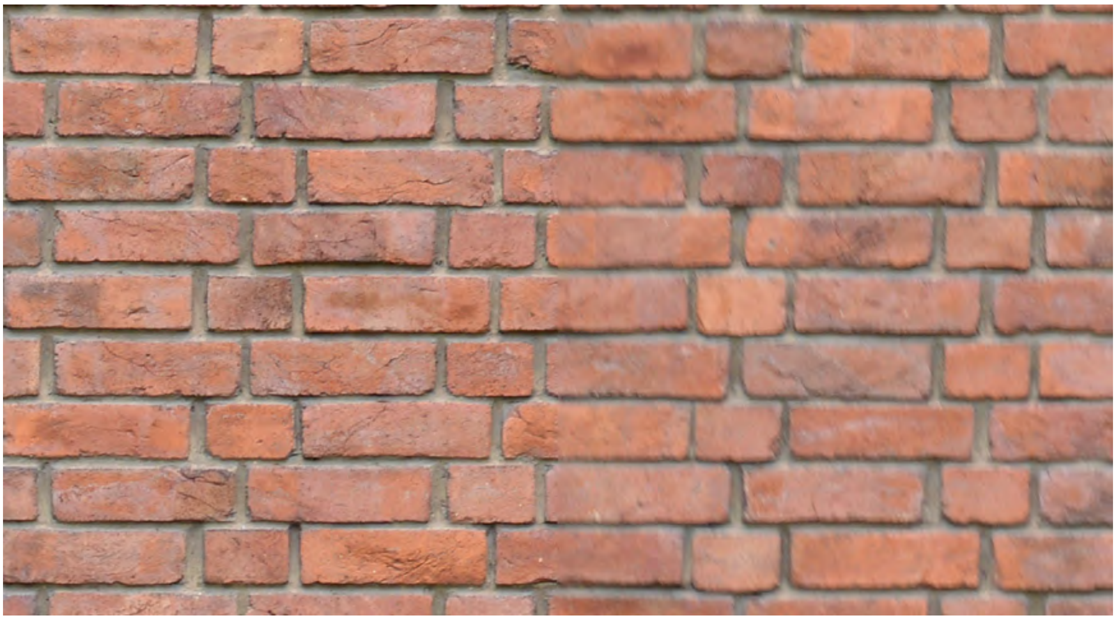

FIGURE 3.4: This figure shows an ortho-photo composed of a mosaic of the original images. The image used for the right hand portion was out of focus. A total of 4 images were used in the processing.

After a set of images is chosen to be analyzed, the photogrammetry software MicMac is used to process the images.

3.3 MicMac

MicMac is an open sourced photogrammetry software. Unlike other open source 3D reconstruction software, MicMac is focused on creating repeatable and precise 3D reconstructions. Other open sourced software typically create good visual representation, but the results lack detail and accuracy (Pierrot-deseilligny et al., 2011). The process is automated; however, there is plenty of room for user input. The two workflows outlined here are by no means the only ways to process images using MicMac, they are a suggestion for how to quickly and repeatably produce results. The steps in processing images after they have been captured and sorted are straight forward, see Figure 3.5.

As seen in Figure 3.5, there are four main steps for processing image data with a fifth step option for geo-referencing. In this thesis, two main workflows are used. The ”aerial” workflow is designed for a set of images which are all roughly taken from the same

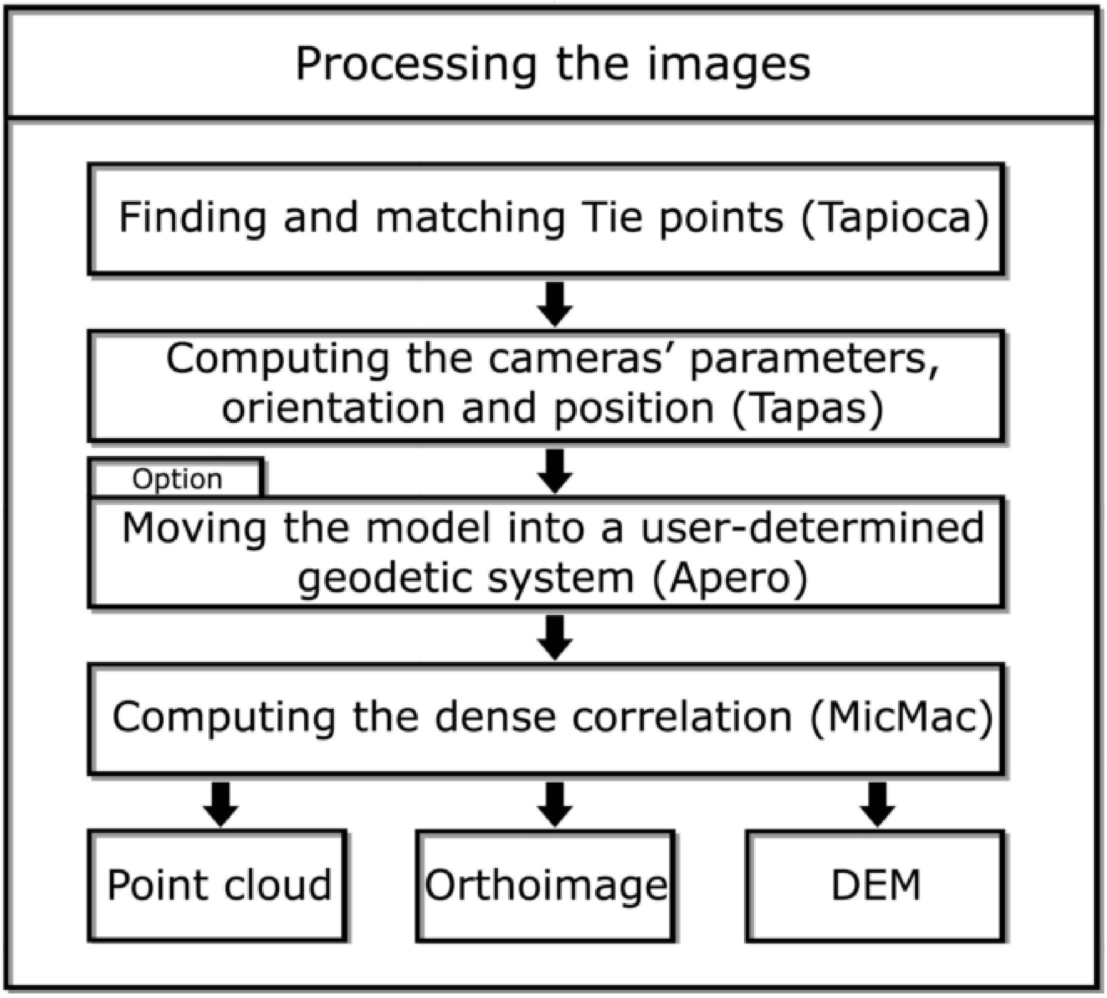

Figure 3.5: This figure shows the basic MicMac workflow , adapted from Girod (2012). The step Apero is optional since it is only used if georeferencing is done.

distance and angle. A basic example of this kind of survey is a plane flying over a field. The ”converging” workflow is designed for images converging around a point (ie. a corner). The two workflows are detailed below.

3.3.1 Aerial workflow

As stated above, the aerial workflow images should in practice be taken with lines of sight, overlap should be around 75% and no camera setting should be changed during the survey.

3.3.1.1 Tapioca

Tapioca is the first step in processing image data. The goal of Tapioca is to select tie points from the separate images by using a SIFT command (Lowe, 2004). For full scale

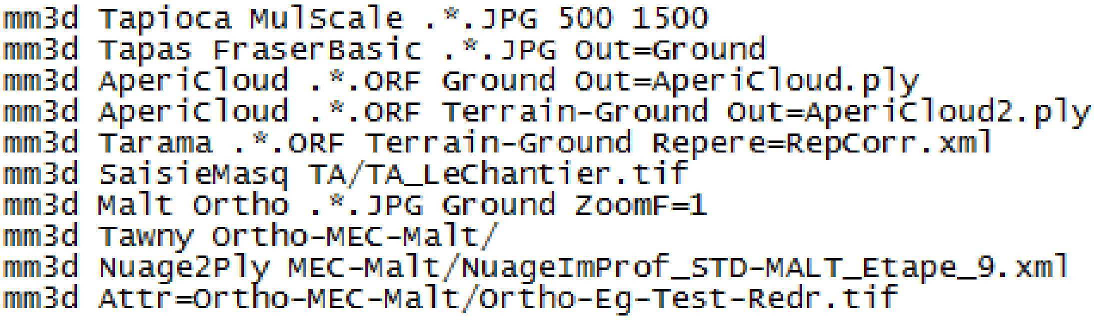

```
mm3d Tapioca MulScale .*.JPG 500 1500
mm3d Tapas FraserBasic .*.JPG Out=Ground
mm3d AperiCloud .*.ORF Ground Out=AperiCloud.ply
mm3d AperiCloud .*.ORF Terrain-Ground Out=AperiCloud2.ply
mm3d Tarama .*.ORF Terrain-Ground Repere=RepCorr.xml
mm3d SaisieMasq TA/TA_LeChantier.tif
mm3d Malt Ortho .*.JPG Ground ZoomF=1
mm3d Tawny Ortho-MEC-Malt/
mm3d Nuage2Ply MEC-Malt/NuageImProf_STD-MALT_Etape_9.xml
mm3d Attr=Ortho-MEC-Malt/Ortho-Eg-Test-Redr.tif
```

FIGURE 3.6: This is the basic aerial workflow used for this thesis. The specifics are discussed below.

images this may be time consuming. There are options for speeding up the process. Using a MulScale (multiple scale) approach the images are resized before the tie points are calculated. The problem with choosing a MulScale approach is the loss of data. With few tie points the final result may be compromised. To test this, two workflows were run on identical datasets consisting of four images of a brick wall. One was completed at full resolution and the other used a MulScale approach. The full scale approach took 21.38 minutes. The mulscale approach took 1.56 minutes. The immediate advantage of using the MulScale approach is apparent. The two tests continued with the first using the maximum degrees of freedom in the next step (Tapas), and the second used limited degrees of freedom. After this, the process was the same. The total time for the accurate version was 40.91 minutes and the reduced quality time was 20.34 minutes. These times were gathered from the output file named mm3d-LogFile.txt. The reduction in quality saved lot of computer processing time. The resulting point clouds were compared using methods described in Section 3.6.1. The results of this comparison are seen in Figures 3.7 and 3.8. The differences here are absolute distances. There is a clear pattern. From this analysis it is impossible to tell which cloud is more accurate. The patterned variations show that depth resolution under half a pixel is not reliable.

Based on these observations, the time needed for full resolution processing is not needed. The use of MulScale in Tapioca cuts the processing time nearly in half while producing very similar results. The non-uniform noise in Figure 3.8 is centered mostly around the edges of the bricks. A slight outline of a brick can be seen on the right hand side of the image. It is not known which processing method most correctly created the point cloud. An experiment similar to the 3D printed gravel experiment by Bertin et al. (2014) is needed to assess this.

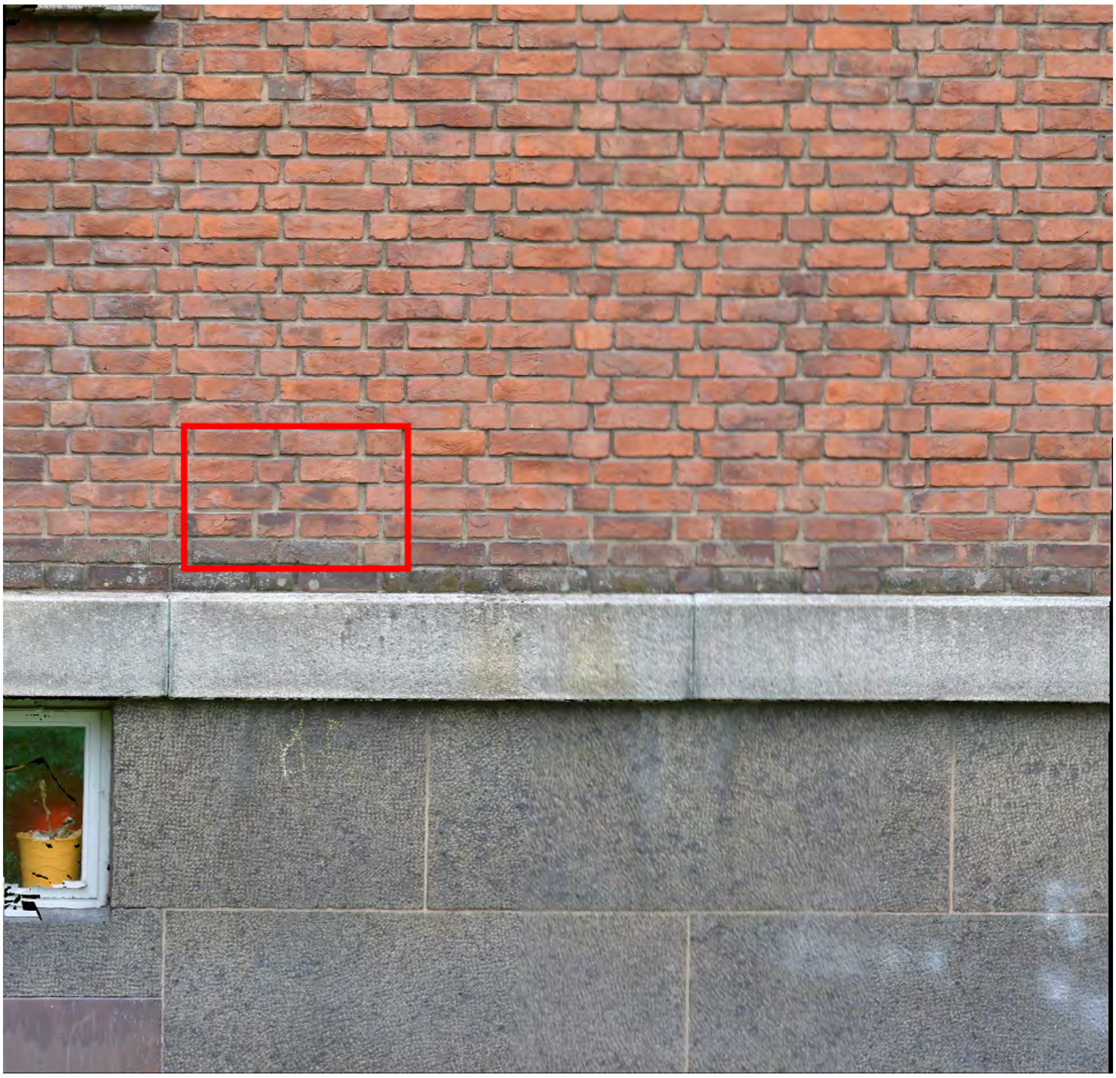

Figure 3.7: Resulting ortho-photo from the test for speed vs. quality. The section highlighted in red was used for point cloud analysis.

3.3.1.2 Tapas

Tapas is a tool which extracts camera data from the exif file of an image. This data gives information on the focal length and type of lens used. From this, the distortion in the images is known and the program can properly calculate the positions of the cameras and points. The output from this step is a series in scale invarient points. Based on the test run on the Tapioca and Tapas settings, it is recommended to use the option of FraserBasic when using Tapas. This limits the degrees of freedom when calculating camera positions. By creating the system of points an cameras Tapas also creates a scale-less coordinate system. This coordinate system should be saved for future use.

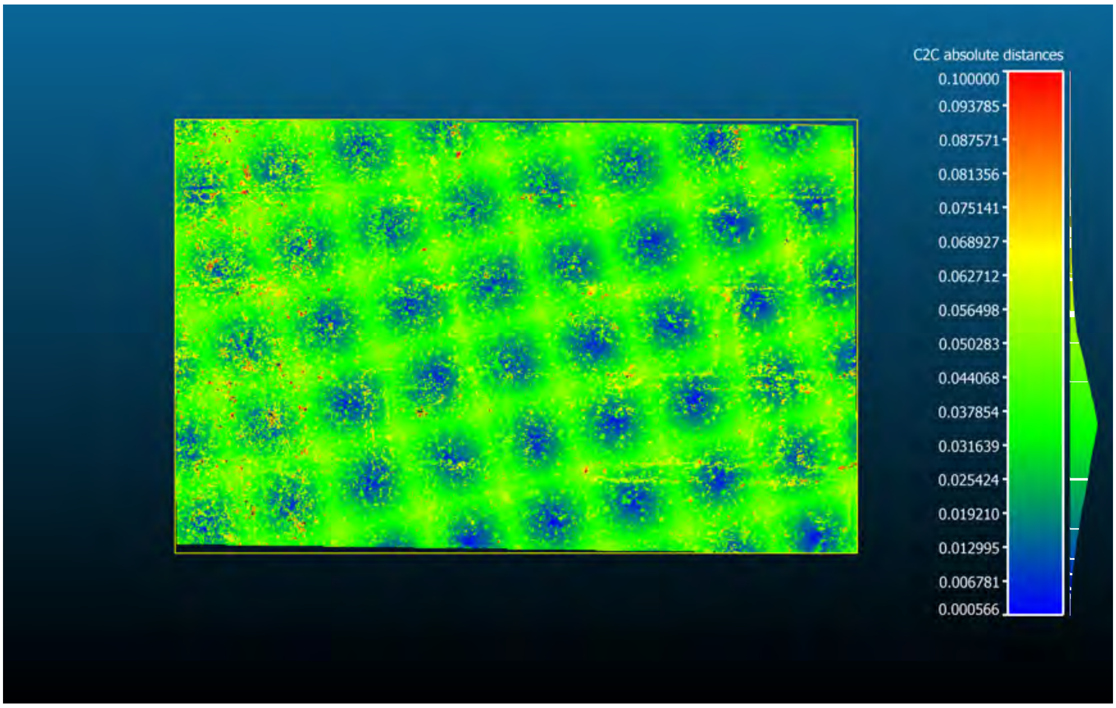

FIGURE 3.8: Point cloud comparison between the high resolution and low resolution tests. The scale is in cm. The resolution of the input images was 1pixel=0.074cm. The average error between the two point clouds is roughly half a pixel in distance.

3.3.1.3 Apericloud

This step is not required in the processing of image data; however, the output can be useful for ensuring the proper completion of the first steps and as a visual aid. The output is a scale invariant display of the tie points and camera positions. A quick glance at the cloud will make it clear if the processing has failed. Figure 3.9 shows camera positions for a terrestrial survey of a glacial moraine in Fjaerland, Norway. The camera positions match the path taken (not shown). This cloud shows that the survey is on the right track. The cloud is dense in the regions of interest and the positions are correct. Figure 3.10 shows a failed apericloud of a classmates head. Some of the camera positions are correct, but the full circle of images is not seen. The point cloud, composed of tie points, is very sparse. This suggests the final high density point cloud may not be accurate. Failure by this point is most likely due to poor survey quality. In the case of the head, the survey probably failed due to subject movement.

3.3.1.4 Georeferencing and orienting

The georeferencing process is explained clearly in the MicMac documentation (Pierrot-Deseilligny, 2013). There are no user input parameters for changing the output or speeding up the process. This step will not be explained here. A sample workflow

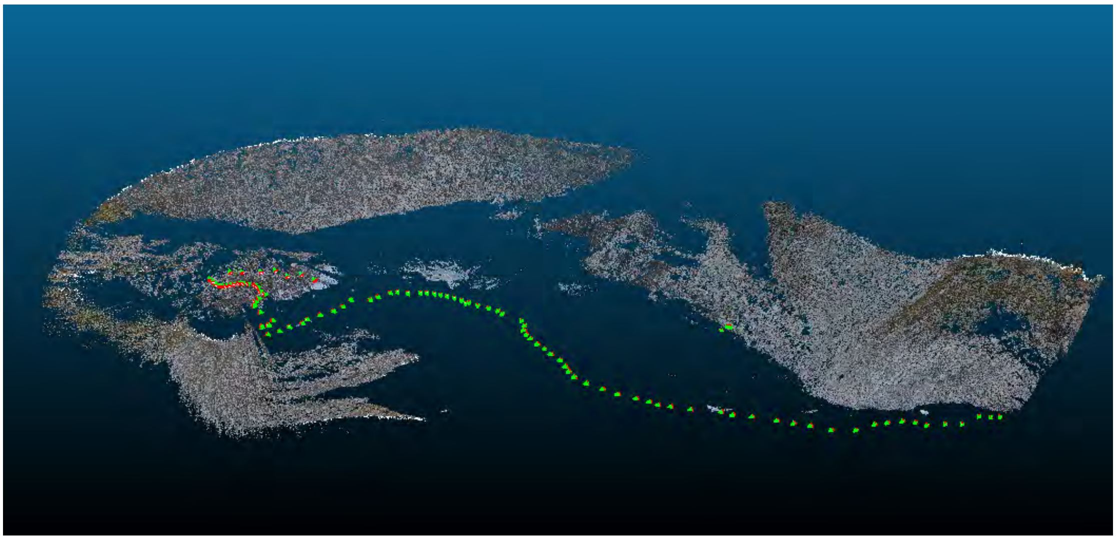

Figure 3.9: This is an example of an apericloud. The camera positions (green/red) all appear to be correct and the point cloud is dense on the moraine which was the subject of this survey.

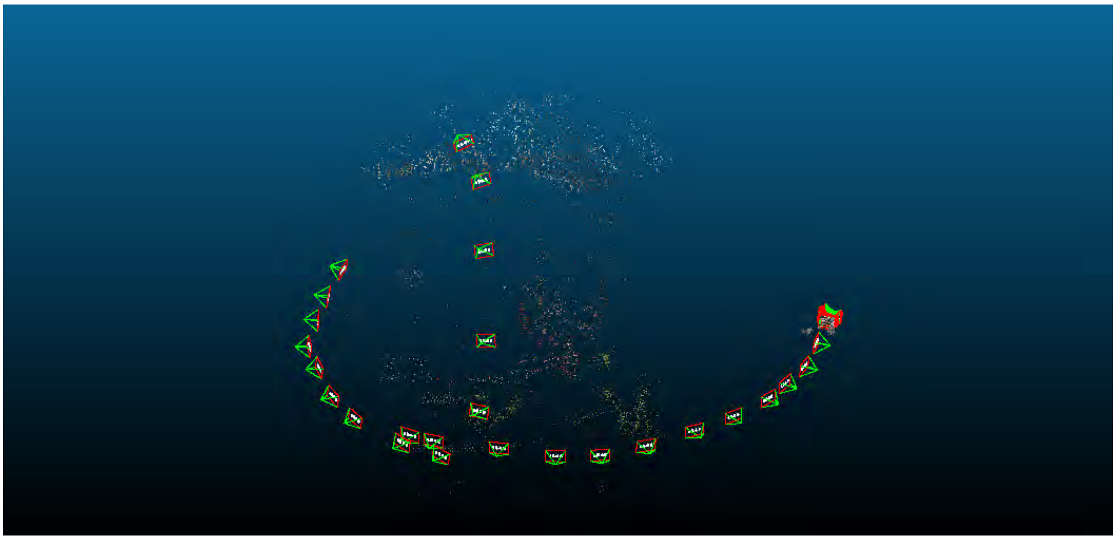

Figure 3.10: This is an example of a poor apericloud. The survey was of a classmate's head. The tie point cloud is very sparse, and the camera positions should circle the head completely. This suggests future problems in the creation of a high resolution point cloud.

with georeferencing steps is in the appendix for reference. It should be noted that when importing GCPs, the maximum number of figures in a coordinate is 6. When using UTM coordinates the largest numbers can be removed and the scene will maintain the same geometry. If the point-cloud needs to be placed on a georeferenced map, an additional transformation is needed to properly orient the image to make up for removed digits.

3.3.1.5 Tarama

Once the scene is positioned, Tarama is used to create a simple ortho-rectified image. This image is used for cropping the scene for high resolution processing. A binary mask (TA_LeChantier_Masq.tif) must be created to select the region to be used for the orthophoto and point cloud. It is important to only select the region of interest so as to minimize processing time. An example of a Tarama output is seen in Figure 3.11. The mask is seen on the right.

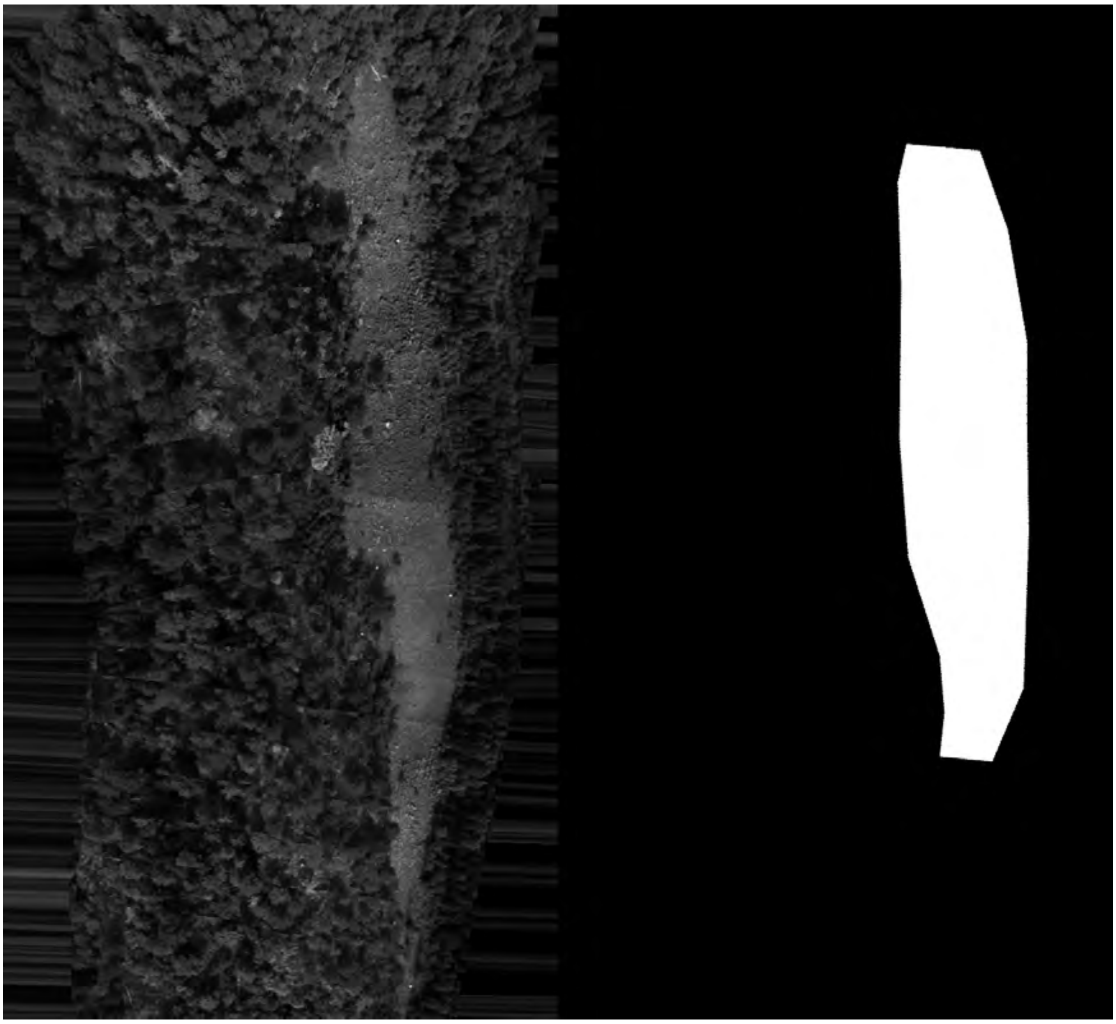

Figure 3.11: This is an example of the output from Tarama. The rectified image on the left and the user created binary mask on the right. The region inside the mask will be processed. This mask was chosen to ensure the resulting orthophotos and point clouds would include at least three of the georeferencing points.

3.3.1.6 Creation of the ortho-photo and point-cloud

The last three steps (Malt, Tawny, and Nuage2ply) for the aerial survey are straight forward but time consuming. In the low resolution brick survey, above 85% of the processing time was used on these steps. There is no way to speed up this process. The workflow for these steps are in Figure 3.12.

3.3.2 Converging workflow

The initial steps of a converging survey are the same as for the aerial survey until the completion of AperiCloud. After this point there, is no need to create an ortho-image as the study area is not flat. If the surveying technique of taking a minimum of one photo every 15 degrees was completed, then there should be sufficient photos for analysis. At this point the user needs to select master images. A mask needs to be created for each of these images. It is important when masking the images to select faces nearly normal to the camera, and to avoid cropping over outside the feature. This causes improperly oriented points to appear. The user must also select which images to pair the masters with. This limits the total processing time as only selected images are compared with each other. A minimum of four images should be paired to each master. Images can be paired to more than one master. .xml files will also need to be created for the individual master images and one combined .xml file for the masters and the images they are paired with. More on this is found in the user guide (Pierrot-Deseilligny, 2013). Masking should be done with care. As seen in Figure 3.13, over masking can result in artifacts.

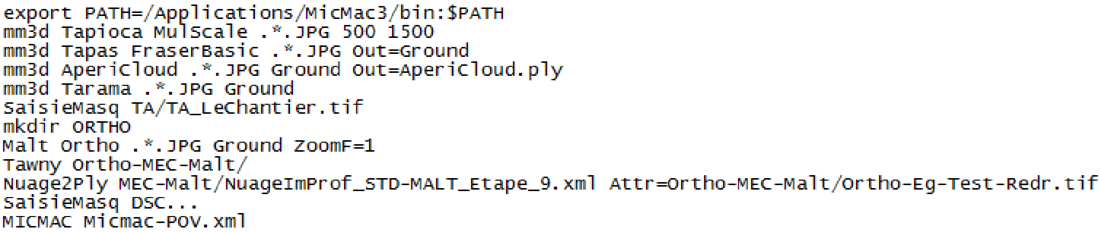

```
export PATH=/Applications/MicMac3/bin:$PATH
mm3d Tapioca MulScale .*.JPG 500 1500
mm3d Tapas FraserBasic .*.JPG Out=Ground
mm3d AperiCloud .*.JPG Ground Out=AperiCloud.ply
mm3d Tarama .*.JPG Ground
SaisieMasq TA/TA_LeChantier.tif
mkdir ORTHO
Malt Ortho .*.JPG Ground ZoomF=1
Tawny Ortho-MEC-Malt/
Nuage2Ply MEC-Malt/NuageImProf_STD-MALT_Etape_9.xml Attr=Ortho-MEC-Malt/Ortho-Eg-Test-Redr.tif
SaisieMasq DSC...
MICMAC Micmac-POV.xml
```

FIGURE 3.12: This is the basic converging workflow used for this thesis. The initial steps are the same as for aerial. The user must make masks for selected ”master images”. These images must be input into the Micmac-POV.xml file. SaisieMasq DSC... refers to masking the master images.

After the masking is complete, the point-cloud can be created. The syntax can be seen in the appendix.

3.4 Potential Problems with MicMac

Over the course of this work, certain problems arose when using MicMac. One common problem was the effect of vignetting. The effect may not be noticeable on small scale surveys, but on aerial surveys consisting of hundreds of images, the effects of vignetting on of the original photos multiplies. Luckily MicMac has a solution for this. The tool,

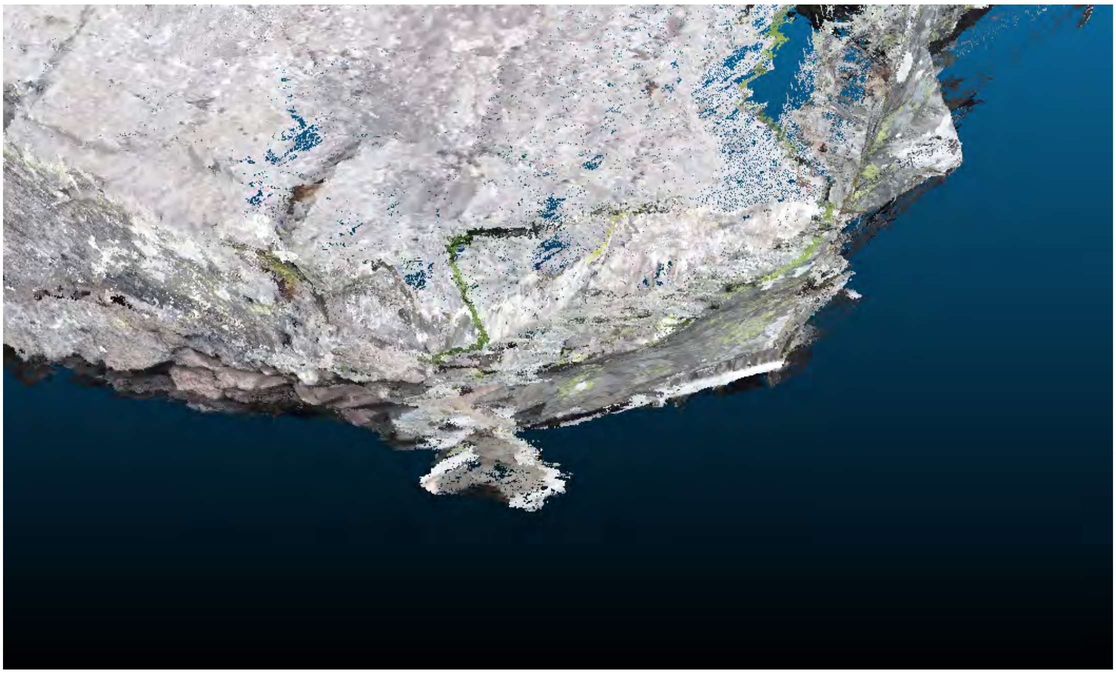

Figure 3.13: Image showing a corner of the boulder used in the terrestrial survey. Due to improper cropping of the "master" images to be used in the convergent micmac workflow, artifacts such as this appear. The boulder did not have this shape.

Vodka, creates a mask for multiplication against the images before they are used in the final steps. The problem with vignetting is that when hundreds of images are complied the effects show up drastically on the edges. This was apparent in the Kolsaas data.

Figure 3.14: The upper images is an orthophoto generated before Vodka use. The bottoms image shows the effect of Vodka on the processing. Although this does not effect the point cloud geometry, vignetted images makes intensity based image filtering difficult.

Another problem associated with MicMac is the need for correctly captured data. This only became an issue when dealing with large images sets with high amounts of vertical camera movement. This occurred when the drone did not stay a fixed distance away from the surface in the fall 2014 study of Kolsaas. The sporadic images caused MicMac to crash when attempts were made to process many images at the same time.

3.5 Grain size analysis

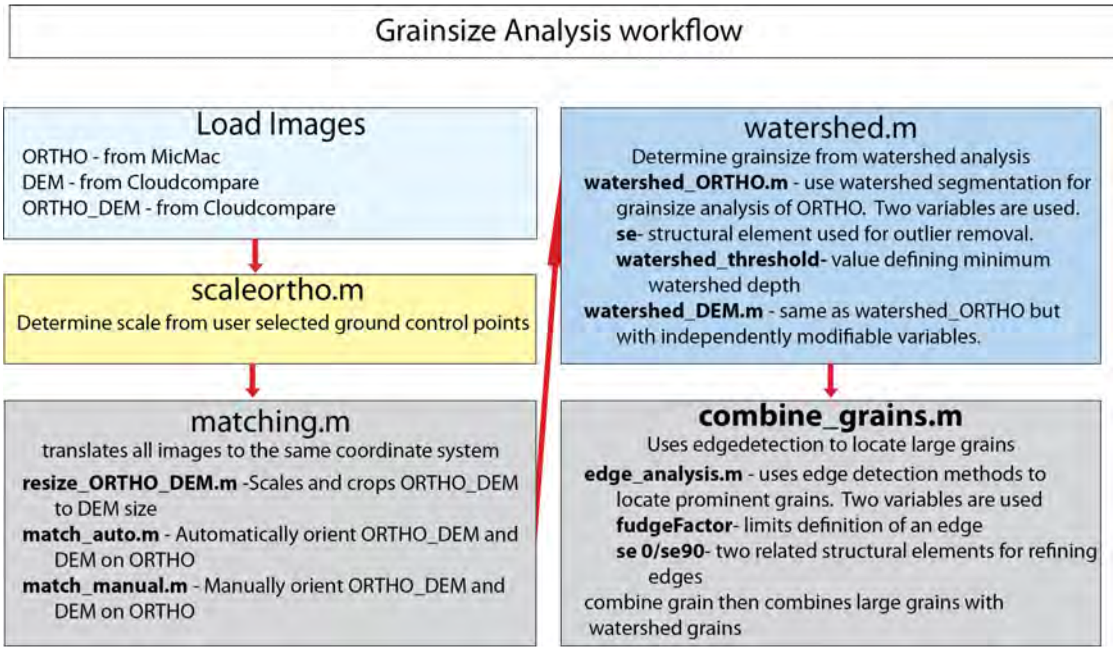

FIGURE 3.15: Workflow showing the steps in the grainsize analysis MatLab package. The variables used in refining the grainsize analysis are shown. The outputs are grain overlay images, grainsize statistics, and detail maps of selected regions.

For grain size analysis a few methods were used. The programs used for this task were MATLAB, cloudcompard, photoshop, and MIP4 student. Matlab was used to run image analysis code created for this thesis. Matlab was selected due to the pre-exisiting set of image analysis tool specifically the Image Processing Toolbox. This toolbox consists of tools for segmentation, morphology, statistics, and measurement (MathWorks (2014)). Cloudcompare was used to create a digital elevation model (DEM) based on the point cloud of a selected region. Photoshop was used for manual image analysis. MIP4 student is an image analysis program with automated grainsize analysis built in. This was used as a comparison for results from the Matlab generated code.

3.5.1 CloudCompare

CloudCompare is a point cloud analysis software. It accepts a wide range of point cloud types and is open sourced. There is an active online community available for problems (www.cloudcompare.org/forum).

For the purpose of grain size analysis cloud compare was used to import point clouds from the aerial surveys. The data was then checked for accuracy between point clouds. If differences existed a planar and rotational translation was used to match point clouds.

Once the point clouds were oriented a the region for analysis was selected. This was done by finding a region between point clouds which had no holes and a sufficient amount of data for analysis. Typically the largest central region was selected. Further segmentation occurs in MATLAB if needed. This step is completely user controlled. With the regions selected a best fit plane is fitted and they are rotated to horizontal. This allows for the creation of an ortho image and height map to be created. Without planar rotation the height map would show values based on elevation instead of highlighting grain shape. The scale of the selected region remains constant.

A height map (DEM) is then created using the "Height grid generation" tool. When exporting the DEM image file it is important to also export a text file. This file will show the range of values. If the point cloud has been georeferenced in MicMac this will be in the same scale used when georeferencing. The DEM is grayscale with values from 0-256. Dividing the range in values in the text file by 256 the scale can be found. In post processing in MatLab it is important to take these values into consideration.

The ortho image from CloudCompare is exported using "Render to file" when the camera positions are all set to "0". Resolution can be selected here. I suggest a value of 4 times. This outputs an ortho-photo of the scene roughly the same dimension as the DEM.For the ortho-photo the bounding box should be left on for the MatLab analysis. This serves as a bounding box used in cropping the images. The ortho is known as ORTHO_DEM in MATLAB. This image is the same shape as the DEM and used for matching the DEM to the ortho-photo exported by MicMac.

If desired a roughness map can be generated. Kernel size is the manual input. If the point clouds are georeferenced this will be in the scale of the image. For the purposes of this thesis the roughness maps were not used, but they may provide important data relating to slide characteristics.

3.5.2 MATLAB

Unless otherwise specified the MATLAB code presented in this section was created for use in this thesis. The MATLAB code for grain size analysis was first broken into separate sections. One for extracting grain size data from ortho-photos and the other for gathering data from the DEM. This was done to find the benefits and drawbacks of each technique. They were then combined to form the ideal results.

The full code is found in the appendix. The code is broken into functions for specific tasks. The separate functions are compiled in one all inclusive operating file. The required input for the code to function are (parenthesized names are the names used in Matlab):

Ortho image(ORTHO) This is the direct output from MicMac

DEM (DEM) This file is created in CloudCompare 3.5.1

Ortho of the DEM region(ORTHO_DEM) Created in CloudCompare3.5.1

Georeferencing points (p1,p2...) Minimum of 3 points are used for scale.

3.5.2.1 scaleortho.m

The first step is to determine the scale of the ortho-photos. This requires the ortho-photo and the three ground control points. The user is prompted to select the ground control points from the ortho-photo. The distance between selected points is compared to the input points. There is also a two point version for ortho-photos with only two points. The advantage of the three point version is further verification of the actual scale. If the scale of the ortho-photo is already known this step can be skipped.

3.5.2.2 matching.m

This function allows for matching of ortho-photos and DEMs. The first step is to match ORTHO_DEM to the DEM. This is done by cropping, scaling, and matching ORTHO_DEM. The DEM is not scaled to preserve the highest data quality. The scale of ORTHO_DEM is not important as it is just used for matching purposes. A function called resize_ORTHO_DEM.m is used for the sizing and positioning of ORTHO_DEM. This function removes the background from the ORTHO_DEM and creates a binary composite image to be used as a mask for ORTHO_DEM. The yellow box, discussed in section 3.5.1, is then used as a bounding box. Everything outside the box is removed. The image is then scaled to the same size as DEM.

Next the matched DEM and ORTHO_DEM are matched with ORTHO. There is both an automated function for this and a manual. It is recommended to check the output of the automated matching before continuing on. The automated matching (match_auto.m) creates feature points and attempts to match them between the two input images (ORTHO_DEM and ORTHO). Proper output should look similar to figure 3.16. Improper matching usually has less than ten functioning tie points. The option to view this figure is commented in match_auto.m. With improper matching the option to manually select tie points is available through match_manual.m. This uses the same transformation function with manually input tie points. A minimum of three are required. Accuracy in this step is crucial. Combining of the DEM and ORTHO grain size results requires perfectly matched images. Offset could lead to off set results and improper data. The output images are cropped to the maximum extent of the selected region.

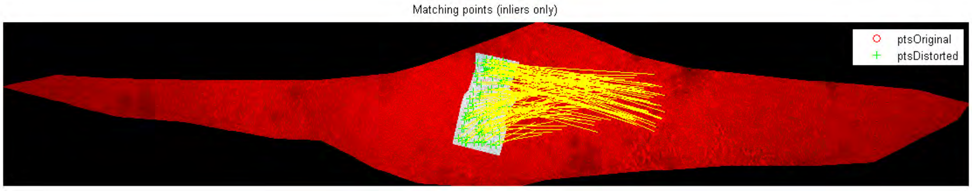

Figure 3.16: Figure showing the results of successful match_auto.m matching. The red image is ORTHO. The red are feature points found but not used in matching. The light colored part of the image represents the original location of ORTHO_DEM. THe green points are feature points used for matching. The yellow lines connect matching feature points on ORTHO and ORTHO_DEM.

3.5.2.3 watershed_analysis.m

This function is the first step of grain size analysis. Using the watershed function built into the image analysis toolbox in MATLAB. There are multiple outputs from this step. The main output is a map of separated grains. The functionality of this step is based on brightness levels of the ORTHO image. Watershed analysis works by separating images by the highest lines of brightness Barraud (2006). The levels were elevation the image are split in to separate regions where water collects. The brightness on top of the grains is greater than that in the shadowed regions surrounding then. For this reason a negative of the ORTHO was used. This made the grains the darkest and the surrounding areas the lightest. Originally watershed was over segmenting the grains. This was due to imperfections on the grain surfaces.

Over large regions looking at individual grains will not be visually representative of grain-size over the region. For this reason grainanaly.m (function in watershed_analysis.m) breaks the ORTHO image into pixels. The area of these pixels is user defined. It is recommended to make them square. The size of the image must also be divisible by the size of the pixel. Once segmented each pixel is assigned an average value for mean grain size area. Grains boarding the edge are removed. The result is a visual representation of changing average grain sizes over the ORTHO. Variables in grainanaly.m may be manually changed to fine tune the results.

It is also an option to analyze a specific region (grainpix.m) to clearly see the grain boundaries. This function uses the same parameters as grainanaly.m over a smaller area. It is a good idea to find tune the variables here before running the full analysis.

There are also matching codes set up for the analysis of the DEM. The same variables are used as for the ORTHO image.

One easily noticeable problem with this technique is the over segmentation of larger grains. Changing the variables does little to fix this (Fig. 3.17). The smaller grains in are apparently segmented properly.

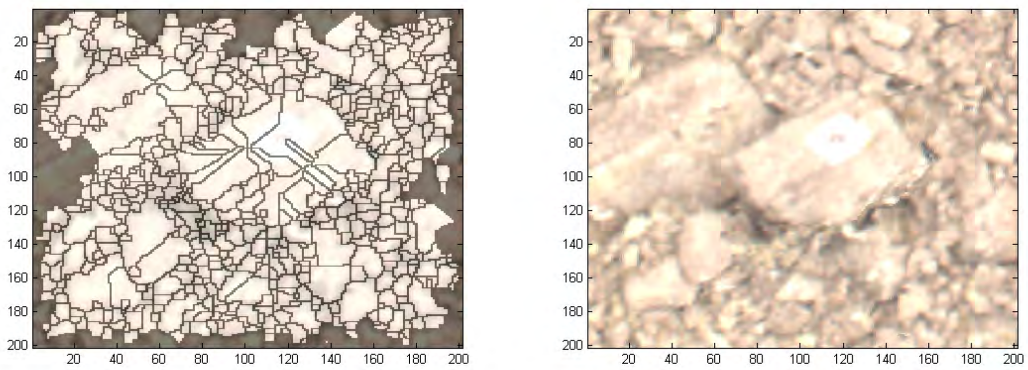

Figure 3.17: Seen here is the watershed segmentation of the ORTHO image. The original image is on the right. As is easily evident. Over segmentation is occurring over the larger grains

3.5.3 edge_detect_.m

This function uses edge detection instead of watershed. This allows for the detection of grains based on gradient changes in the image brightness. The image toolbox has two built in edge detection algorithm: sobel and canny. These are good for grain boundaries. They are not however easily modifiable and result in rough boarders for the edges Yen (2003). For the purpose of this project they are sufficient.

When testing the two detection algorithms sobel returned more accurate results. Canny seemed to under segment the image. Edge detection worked well at initially segmenting the large grains, but the smaller grains were not well segmented. To solve this problem the large grains were stored as shapes on a binary image. This image was then multiplied against the original ortho-photo to create a new image for edge detecting. Watershed was used for its ability to define the small grains as stated in 3.5.2.3.

3.5.4 Analyzing the grain data

To analyze the grain data a select area was chosen for analysis. Various techniques were used to fine tune the processing. Once the processing reaches a sufficient level the results were compared between the flights. Ideally the result should be the same. The main tool for assessing validity of the results was a visual analysis of the region. It is clear when the analysis is not correct. The attempt is to create a workflow that can produce statistically significant results between different data sources.

3.6 Further analysis

3.6.1 Comparing point clouds

The comparison of point clouds is done using CloudCompare. Living up to its name, CloudCompare can measure the difference between point clouds. The georeferencing should limit differences between the point clouds. The small differences can be corrected for by matching the clouds and preforming a transformation. This transformation should not skew or scale the data. This can be done by manually selecting points of by automatically alignment. Manual alignment is useful for surveys in which movement may have occurred. With automatic alignment the best fit match can be made. From here the point clouds can be compared for similarities.

3.6.2 Orthoimage comparison

The ability to reproduce an accurate and repeatable orthoimage is key to this experiment. Being able to extract the same results from different surveys of the same features will be a validation of this project. To Compare the orthoimages they are matched using either manual or automated matching (similar to Fig. 3.16). After this the movement of pixels is monitored using the motion detecting function normxcorr2.m Analysis of the resulting vectors will show if the accuracy of the orthoimages is sufficient. The MATLAB codes for this can be found in the Appendix .One problem with this code is it is memory intensive when automatically matching points between two orthoimages. This resulted in the crashing of MATLAB To work around this a manual matching tool was created. A minimum of three points are required for the manual matching.

The offset is displayed as a group of vectors. Each vector represents the average displacement vector for a 50 pixel x 50 pixel surrounding region.

3.6.3 Roughness

Even though the values for roughness will not be analyzed in this thesis the ability to reproduce them is important. To ensure similar roughness measurements can be repeated a roughness map will be made for each of the three flights. A quick visual inspection of these roughness maps will show if the values are easily repeatable.

Chapter 4

Kolsaas

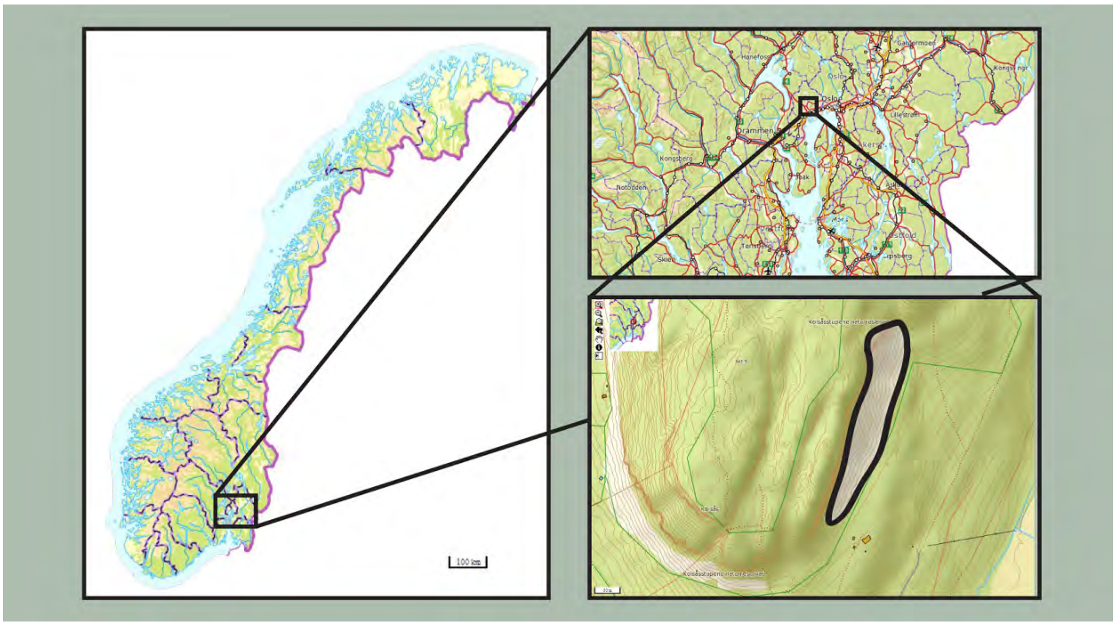

Figure 4.1: Map showing the location of the Kolsaas scree slop in Norway. The scree slope is outlined in black in the lower right hand image.

A scree slope located in Kolsaas Norway (Fig. 4.1) is the main study area for this thesis. The slope was selected for multiple reasons. The slope lays beneath a cliff composed of near horizontal layers of multiple rock types. The lateral and vertical changes in composition cause the scree to have near homogeneous and mixed grain sizes throughout. In addition to varying composition the scree slope is hard to access as the bottom is surrounded by trees and the top of the cliff is hazardous without proper equipment. These sort of access problems can be very common when dealing with slide tracks in wooded or highly topographic terrain making Kolsaas an ideal location for developing a workflow for landslide track analysis.

4.1 Geological Setting

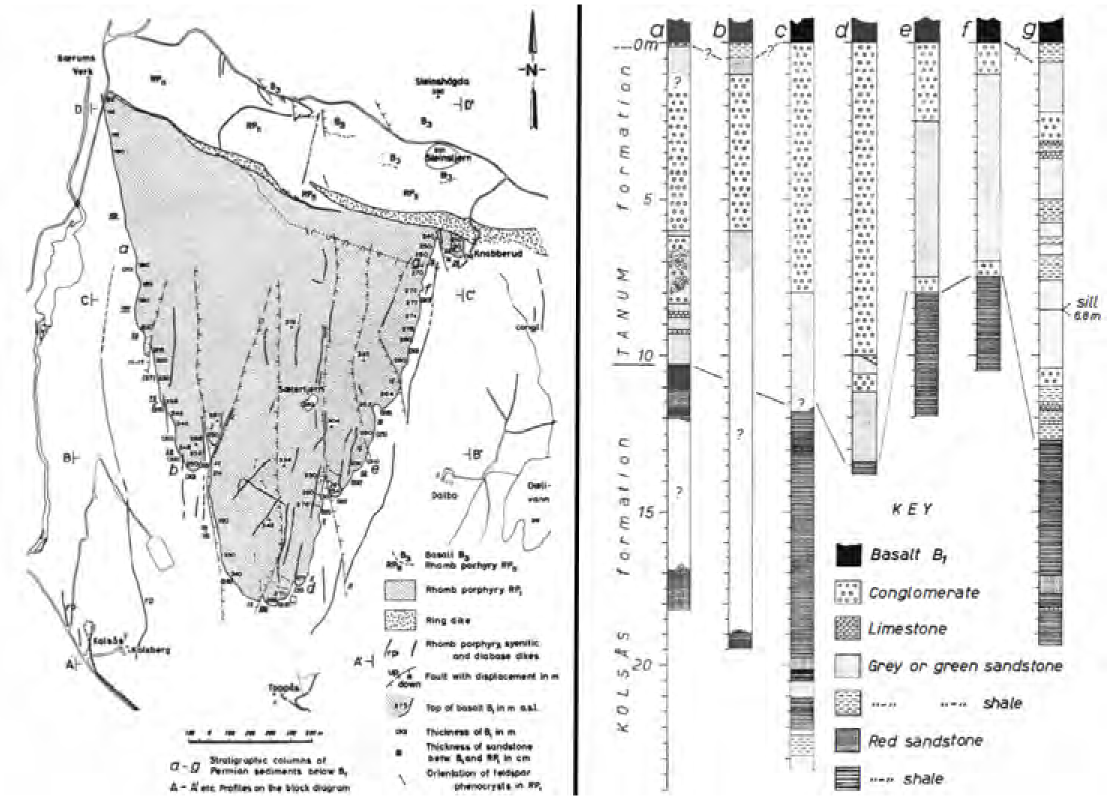

FIGURE 4.2: Geologic map (left) and bore hole data (right) as presented in Dons and Gyory (1967). This The map shows the extent of the porphyry on the mountain. The geologic map covers approximately the same region as the bottom right image in fig. 4.1. The bore hole data shows the presence of The Kolsaas Formation

Kolsaas is an easy to access hill located 10 kilometers from the center of Oslo. The site is a popular outdoor destination and geology tour groups commonly frequent the region due to the ease of access and exposed outcrops (Dons and Gyory, 1967). Located in the Oslo rift the geology of Kolsaas consists of both sedimentary and igneous rocks. The hill of Kolsaas is also a popular climbing destination with multiple cliffs. The cliff and scree presented in this thesis are located on the eastern side of Kolsaas (fig.4.1). The region was geomorphologically shaped by glaciers during the past glaciations. The stratigraphy of the region consists of multiple groups (fig.4.2). At the base of Kolsaas the Asker group is found. This group, permian in age, consists of three formations. The Kolsaas Formation is the lowest member of the Asker group ((Dons and Gyory, 1967). This formation is overlain by the Tanum formation. The Tanum formation is dominated by quartz grain with mica, limestone, and schist also found (Larsen et al., 2008). The Skaugum Formation, which is the top formation in the Asker Group, is not clearly defined in the Kolsaas area (citepTidsskrift)

The Asker group is then covered by a basalt flow. The flow was one of the first dating around 300 ma. With a thickness of 20 to 30 meters this is one of the dominating layers in the study area. The basaltic layer known as B1 in literature is believed to have been created by a single flow. Following the B1 flow a sandstone of irregular thickness and composition was deposited. Above this sandstone is a Rhomb-porphyry lava or RP_1 (Dons and Gyory, 1967). This layer is the result of volcanic eruptions associated with the Oslo Rift. This layer was very thick at the time of deposition with a thickness of up to 100m in the Oslo region (Larsen et al., 2008). Today at Kolsaas this layer has been eroded to around 40m varying laterally. The durability of the basaltic layer (B1) is a main reason for the local topographic prominence of the Kolsaas region (Dons and Gyory, 1967). For this project the geologic setting can be broken down into the cliff and the scree.

4.1.1 Cliff

The cliff overlying the scree slope varies laterally in height, composition, and basal elevation. The layers are predominantly flat. On the southern end of the cliff the conglomerate of the Tanum formation is seen at the base. The B1 basalt is above the conglomerate is the B1 basalt. This basalt continues laterally covering most of the cliff. The basalt appears columnar in some regions;however, a distinct fracture pattern is not easily recognized. Above this is the Rhomb-porphyry. This layer continues to the top of the cliff.

4.1.2 Scree

The lateral changes in the composition of the cliff have a direct effect on the underlying scree. The scree is mainly composed of basalt and Rhomb-porphyry. Conglomerate grains are not as common since the conglomerate is only present on the southern end of the cliff.

4.1.3 Relation to other regions

The formations and terrain types seen in the Kolsaas cliff and scree can be compared to those found in active or recent slide regions. The scree slope can be compared to scree slopes in regions with active rock fall. The cliff is composed of various rocktypes and can thus give information on processing techniques needed to extract data such as possible failure planes or existing fractures. The scree changes from homogeneous particle sizes to non-homogeneous laterally. This allows for the development of techniques to analyze both types of fields. The difficulty of terrestrial access to the Kolsaas slope is also similar to possible field localities in which ground surveys could be difficult or dangerous. The Kolsaas locality acts as a learning and process development site for future in-field applications of aerial and terrestrial photogrammetry.

4.2 Data Collection

FIGURE 4.3: Photos from the June 2013 field work. The drone seen in the left image had 8 propellers. This location is 30 m east of the scree slope.

Data analysis at Kolsaas consisted of four aerial surveys and one terrestrial survey. Three aerial surveys were completed in June of 2013. These surveys were completed with the help of Bygg Control AS (fig.4.3). The fourth aerial survey was completed with the help of Luc Girod and Boris Leroux in June 2014 along with the terrestrial survey. The reason for repetitive testing was to acquire an adequate amount of data to determine the effects of camera quality, image resolution and camera position on the final results.

4.2.1 Aerial photography

This section will discuss the methods used for image acquisition. The data from the aerial surveys serves as the main source of data for the Kolsaas study area. The scree slope runs roughly north south and is surrounded by trees to the east and a cliff to the west. These features make terrestrial access difficult. Combined with the length of the slope (400m north-south) make land based data acquisition nearly impossible. Aerial surveys allow for safe access and improved image coverage.

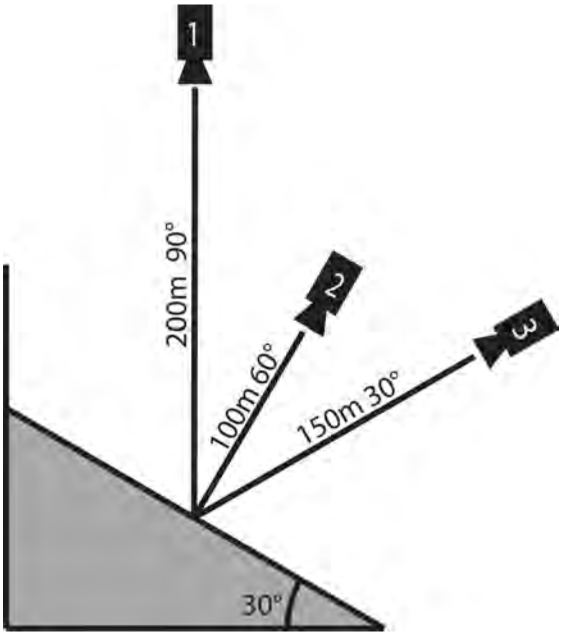

Figure 4.4: Diagram showing a cross sectional view of the three aerial surveys completed in June 2013. The UAV flew the camera with different aspects and distances from the slope. The surveys are labeled with numbers on the cameras.

4.2.1.1 Aerial surveys June 2013

The three first aerial surveys were completed in June of 2013. These surveys used an eight rotor unmanned aerial vehicle (UAV) operated by Bygg Control AS. The camera was an Olympus E-PM 2. This camera records .ORF images with a size of 3024 x 4032 pixels. When operated from 100m the resolution is roughly 2.7 cm/pixel. The resolution was calculated using ground control points and a image from the second aerial survey which flew at 100m normal to the slope (fig.4.4).

In order to quantify the results an array of ground control points (GCPs) was set up. This array consisted of 9 points. These points were marked using 1x1m markers. The markers were white with a black center. This makes them easily distinguishable from aerial photographs. The locations of the points were measured by a high-accuracy GPS operated by Bygg Control AS.

The survey paths and photo overlap were decided prior to flying and an autopilot system was used to fly the UAV. This allowed for the position of the UAV to be known however using Structure From Motion (SFM) techniques these positions were not used in analysis. The ideal overlap between images is 75%. This overlap when used horizontally and vertically allow for up to a 16 times overlap in the center of the study (3.2). During these surveys the number of lateral passes over the scree limited maximum overlap. More overlap improves results but SFM programs can deliver accurate results with as few as 4 photos.

FIGURE 4.5: Photo taken from the UAV in June of 2013 of two ground control points (GCPs) survey of Kolsaas. The GCPs are 1x1m in size.

The surveys consisted of multiple lengthwise passes over the scree slope during which the UAV would pause and take photographs. The spacing of photography was determined by the hight and desired overlap. The surveys consisted of 3-4 passes over the slope. The second survey (fig.4.4) required more passes to adequately cover the entire slope with the desired 75% overlap. Figure 4.6 displays a sparse point cloud composed of tie points. This is one of the first outputs when using MicMac. The camera positions are seen as red/green markers. This is the third survey and the three passes are clearly seen.

The first survey consisted of only two passed over the scree. This was due to the height and image cover of the scree. The resolution for this survey was roughly 4.7cm/pix depending on slight fluctuations in altitude of the UAV and the relation of the camera to the selected point on the scree. Points at the bottom of the scree would have lower resolution as they are further from the lens. The lighting conditions were sunny. Sunny lighting can potentially cause issues when using photogrammety if the survey takes a significant amount of time. A significant amount of time can be defined as sufficient time for shadows to move causing possible offset of tie points. Since this survey consisted of a low number of images which were taken in a short period of time, this was not an issue. Due to the height of the flight the resolution of the scree slope was not too high. No real clear definition could be seen on between the smaller boulders (fig. 4.7). The images also seemed to be slightly out of focus

The second and third surveys were completed with cloud cover. This is ideal for image capturing as high variations in brightness between shadows and sun exposed areas will not result in missing data. The time constraint caused by moving shadows is also removed. Flight 2 showed 2.7 cm/pix resolution. As the camera was normal to the scree slope this resolution was roughly constant throughout the image depending on distortion from the lens. The resolution of third filght was 4 cm/pix. As with flight 1 this value also changes with respect to position of the camera and the scree slope.

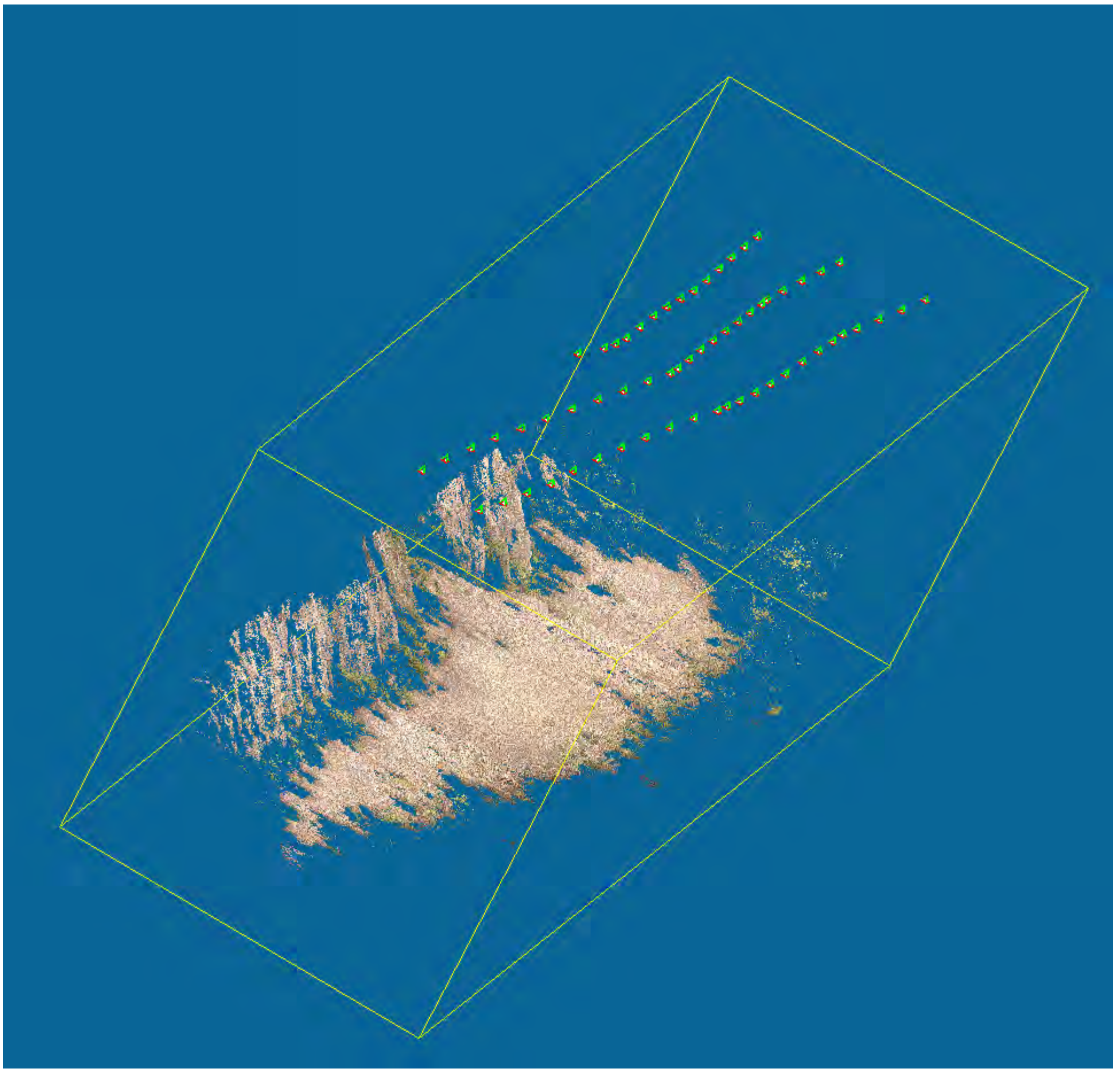

Figure 4.6: Preliminary point cloud showing tie-points and camera positions. Shown as green/red markers (oriented in the same direction as the camera) are the positions of the UAV during survey 3 of the June 2013 surveys completed at Kolsaas. The coordinate system is scaleless thus no scale bar is shown. The length of the scree slope is roughly 500 m.

The second and third aerial surveys not only covered the scree, but they also imaged the overlying cliff. The first survey did not cover a significant area of the cliff due to the vertical camera angle. To properly image the cliff a flight with a horizontal camera position would have been idea. However, the main goal was to image the scree. The autopilot setup and the nearby trees also presented a problem as the UAV operators did not feel comfortable flying the UAV in the proximity of potential flight hazards. A manually controlled flight may have accommodated cliff imaging. During the June 2014 surveys the focus was on the scree so imaging of the cliff was not completed.

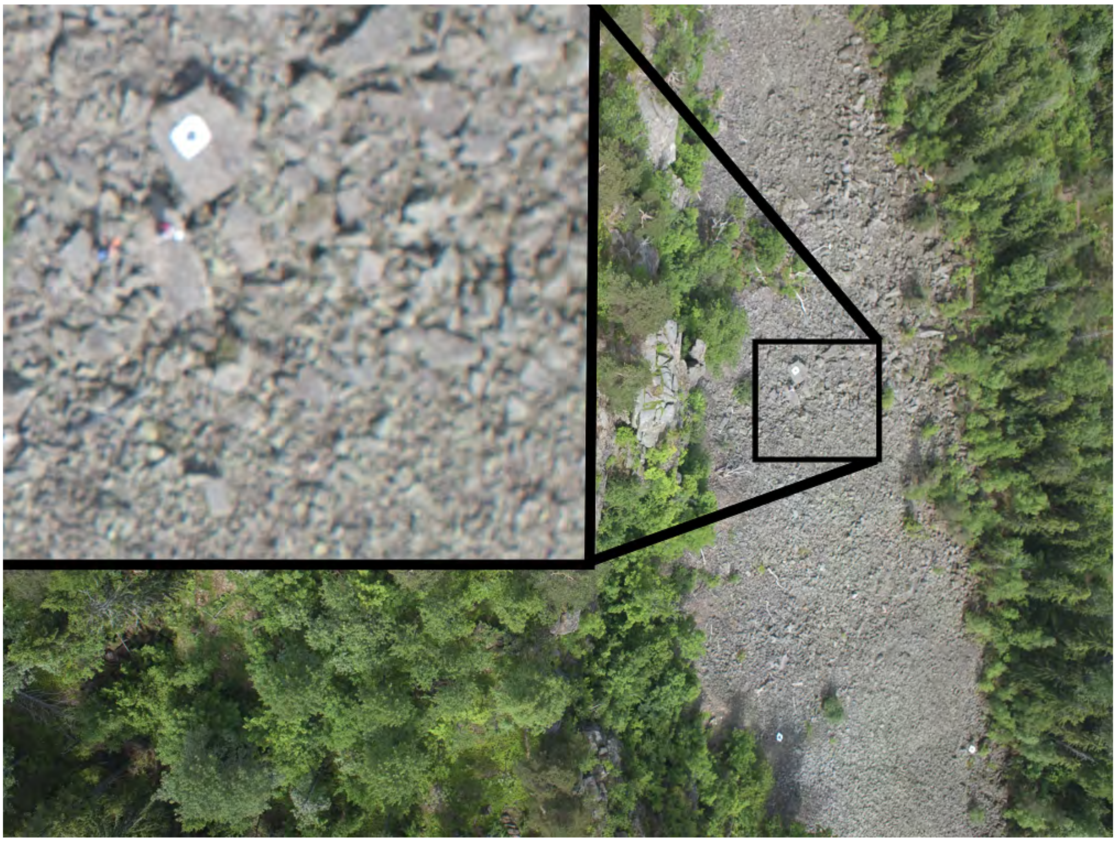

FIGURE 4.7: Image showing the resolution of the flight 1 images. Seen in the zoomed in section is a ground control point measuring 1x1 m and a few people for scale. The images also appears to be slightly out of focus.

4.2.1.2 Aerial surveys June 2014

In June 2014 a second set of tests were completed with a different UAV. The drone used was the DJI Phantom 2 Vision+. This drone is consumer priced at 1099 euro (in July, 2014), roughly 7000 euro cheaper than the UAV flown in 2013. The reason for this test was to attempt to focus on selected regions of the scree measuring roughly 10x10 m. These regions were selected from orthoimages from the June 2013 flights (4.8). The regions were selected based on average particle size in each.

There were two days of aerial surveys completed. The first day consisted of a total station survey and aerial survey. The total station survey was completed as a method for testing the accuracy of the georeferencing as well as a way to determine accurate distances between points on the orthoimages. Two aerial surveys were completed on the first two (left and middle) selected regions from fig.4.8. The third was not surveyed due to low battery in the UAV. The lighting conditions were overcast and the UAV flew roughly 3-4m above the surface of the scree with the camera positioned to image directly below the drone. The extreme fish-eye lens along with the close proximity and angle of the scree caused problems. These problems are discussed in section 4.3.1. The main

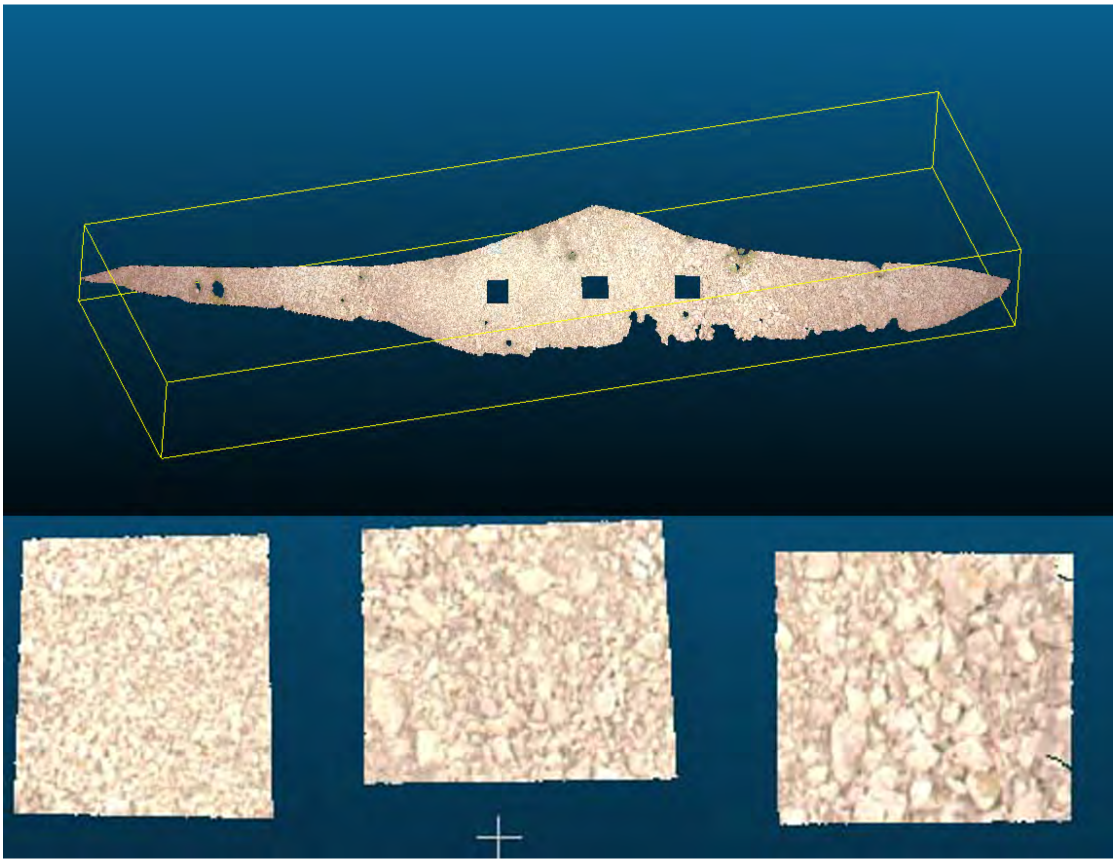

Figure 4.8: These two images show the selected regions to be used for the June 2014 aerial surveys of the Kolsaas scree. They were selected for their differences in particle-size and homogeneity.Top: Orthoimage of the Kolsaas scree with selected repeat survey areas removed Bottom: Selected repeat survey areas measuring roughly 10x10m. The difference in particle-size can be seen

problem was color aliasing near predominantly near the edges but also noticeable near the center of the images. This caused problems when using MicMac.

Due to the problems with the first survey we completed a second survey with a few notable changes. When using the DJI Phantom 2 Vision+ setup we found it important to position the camera normal to the study region. This limited the aliasing near the center of the image. We also concentrated on getting both close (1-2m) as well as distant (> 10m) images in order to ensure sufficient coverage. During this survey the UAV was manually piloted and was set to take an image every three seconds. This results in a more sporadic array of camera positions (fig.4.9) than the precise passes of the June 2013 surveys.

During the image capturing process the light remained overcast. This stayed true for the surveying of the three regions. For the first region we focused on collecting images very near to the scree coming within 1m at certain point. Imaging at this resolution made complete coverage difficult. The second two regions were imaged from a further

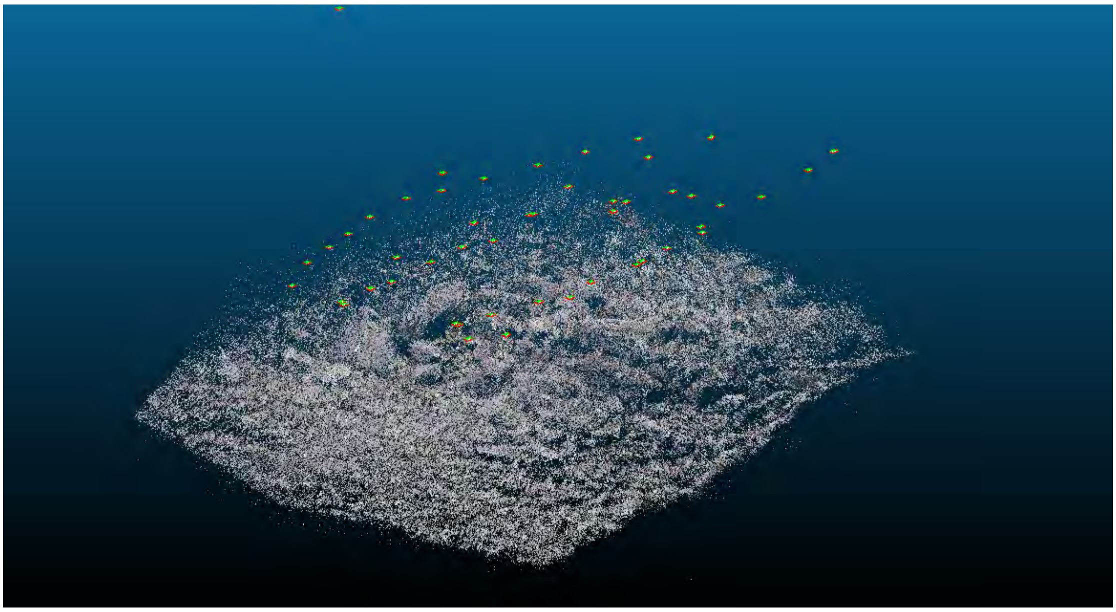

FIGURE 4.9: —Preliminary tie-point cloud for a section 2 of the June 2014 Kolsaas aerial surveys. The camera positions are seen as green/red markers. There is no scalebar as this output is created prior to georeferencing. Siginificant noise can be seen, but the camera positions seem to be correct.

distance. Between surveys we flew the UAV higher and imaged a larger portion of the scree to accurately connect the separate regions in the processing steps. The average resolution of the images used in processing was 1 cm/pixel.

Due to lack of time all the data from these surveys have not been processed. Instead of focusing on the dependency of aerial surveys on grain size homogeneity, the data is used to test repeatability over time. This means that the data was compared with data from 2013 to see if meaningful comparisons could be made.

4.2.2 Terrestrial survey

A terrestrial survey was completed in June 2014. The goal of this survey was to compare the accuracy of the aerial surveys to a close-up survey of a specific boulder. This boulder was chosen due to its prominence in both the 2013 and 2014 aerial surveys (fig.4.10). To properly survey this boulder a series of photographs were taken using a Nikon D7100. A distance of 3-4m was maintained around the boulder. The light conditions were overcast. This survey was a success in that the boulder was modeled, but time ran out for comparison between the boulder it's position in the point clouds.

Maintaining the proper distance was a slight issue as the terrain was rough and access was at times difficult. The survey took roughly five minutes to complete. In total 82 photographs were taken. The locations of these photos are seen in fig. 4.11. When taking

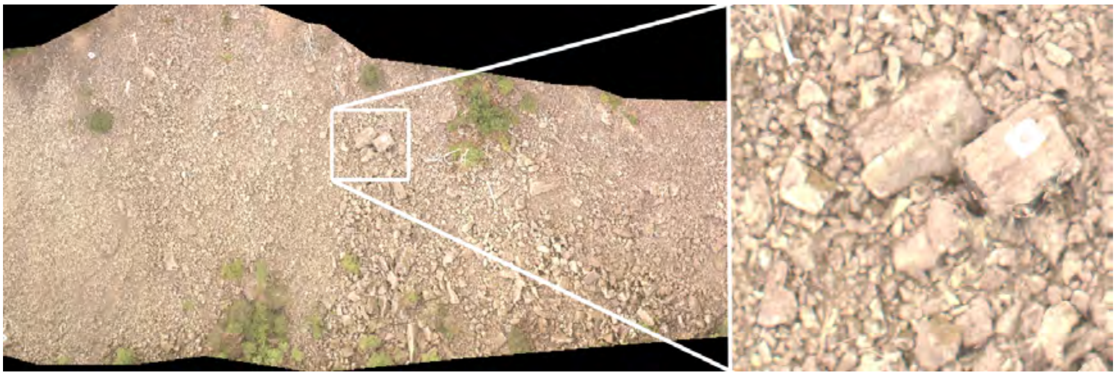

Figure 4.10: Marked is the location of the boulder in the scree field. The large boulder on the right with the ground control marker is the one in used for the terrestrial survey. Although it is not clear in the orthoimage this boulder is laying slightly on top of the other boulder.

images two images were taken from each standing location. One from low pointing up and one from high pointing down. This was done in an attempt to create maximum coverage.

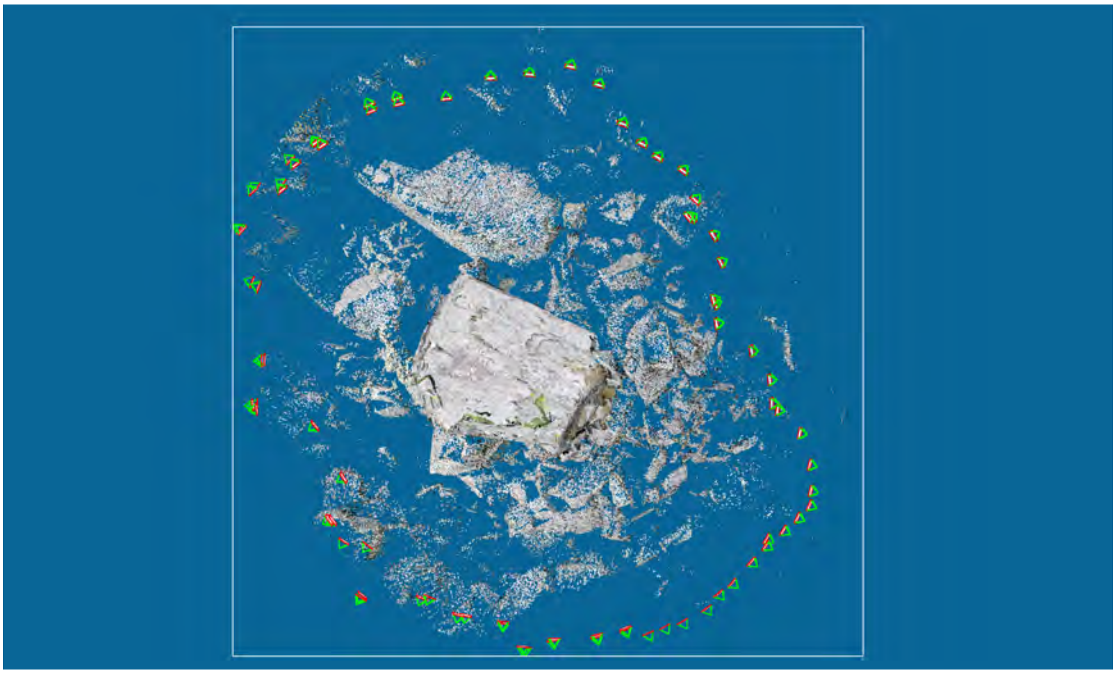

Figure 4.11: Combined apericloud and point cloud for the boulder analysis. The camera locations are marked with green/red markers. At most points two images were taken (one high and one low).

When processing the images the convergent workflow was used. This workflow involves the processing of multiple surfaces. The surfaces are user selected. This is done by selecting "master" images and creating binary masks for defining the region to be processed. For this boulder 6 images were selected. This provided enough coverage of the boulder to create a full point-cloud from the combined data. In an attempt to create full coverage some of the masks were too large. This resulted in noise around the edge of the masked regions. This is evidenced by artifacts around sharp corners (fig. 3.13). To avoid this problem in the future master images would be chosen for the middle section of the flat surfaces to avoid cropping around the edges. To ensure full coverage an image aimed at the corner with clear view on both sides could also be used.

4.3 Data Analysis

The photographs captured from the aerial and terrestrial surveys were processed using the following programs:

MicMac for orthoimage, and point-cloud generation

CloudCompare for DEM creation and point cloud comparison

Matlab Used to compare orthoimages and run grain size analysis

The data analysis can be separated into two main categories. Pre-processing and post-processing. Pre-processing involves the organization of image files and creation of the orthoimage and point-cloud. Post-processing deals with the handling of the results from pre-processing. The individual steps for a MicMac workflow are discussed in chapter 3. All results in this section were created using FraserBasic and mulScale. These are the lower resolution options with faster processing times.

4.3.1 MicMac processing

For the aerial surveys the workflow described in 3 was used. One problem encountered was intense vignetting of the orthoimage. This was due to the slight vignetting on the original images multiplied many times over. The Vodka tool was used to counteract this. Results from Vodka are seen in Figure 3.14. In each case the same workflow was used. The mulScale function was used for Tapioca and FraserBasic was used for Tapas (3.3) The similar results as seen and described in fig. 3.8 the results are virtually the same with significant time saved.

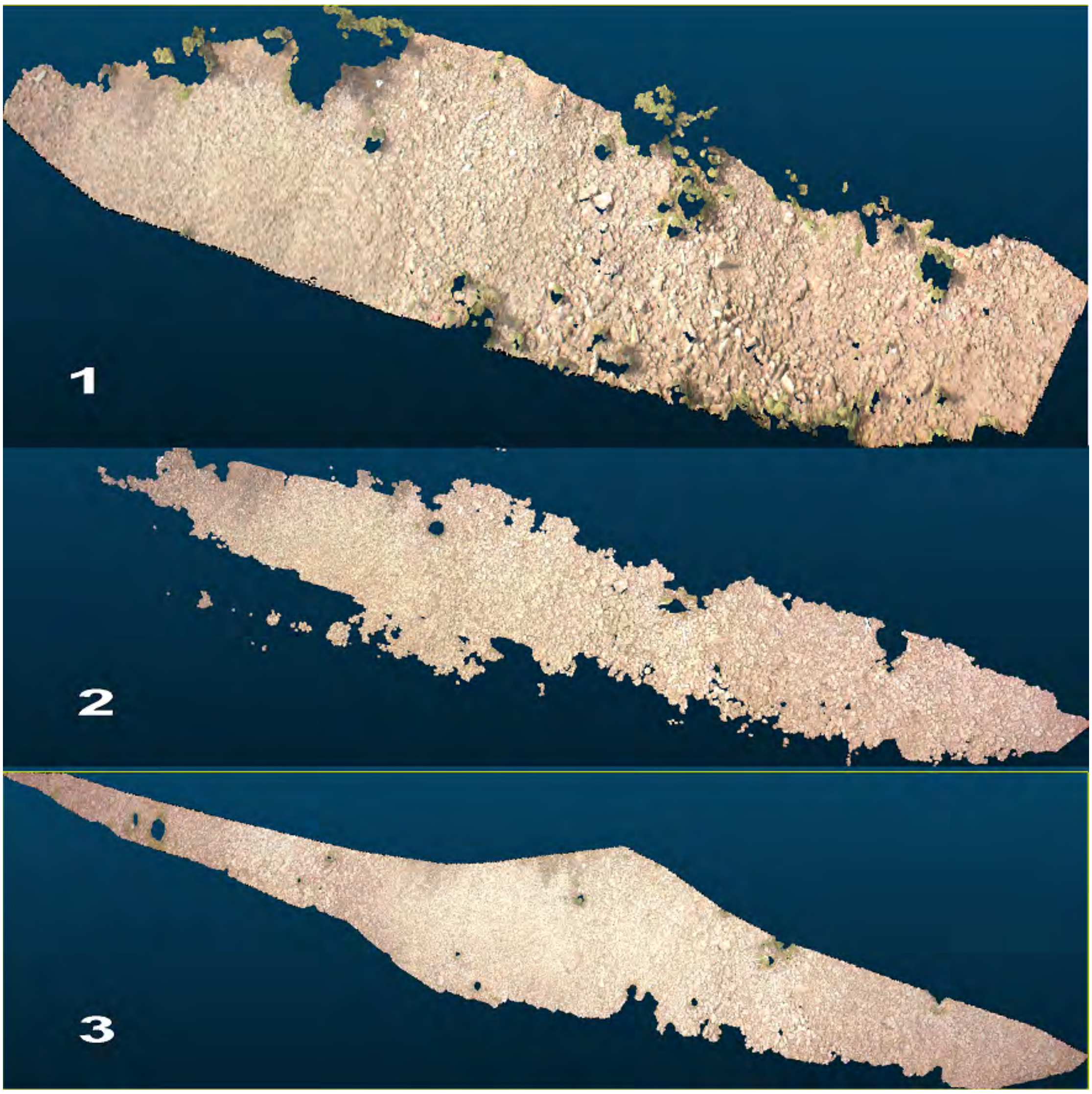

Figure 4.12: Image showing point clouds from the three flights of June 2013. They are labeled according to their flight number. As is evident here, flight 3 have the best results. There are the fewest holes and the greatest coverage. The limited coverage of the first two flights makes full comparison with flight 3 impossible.

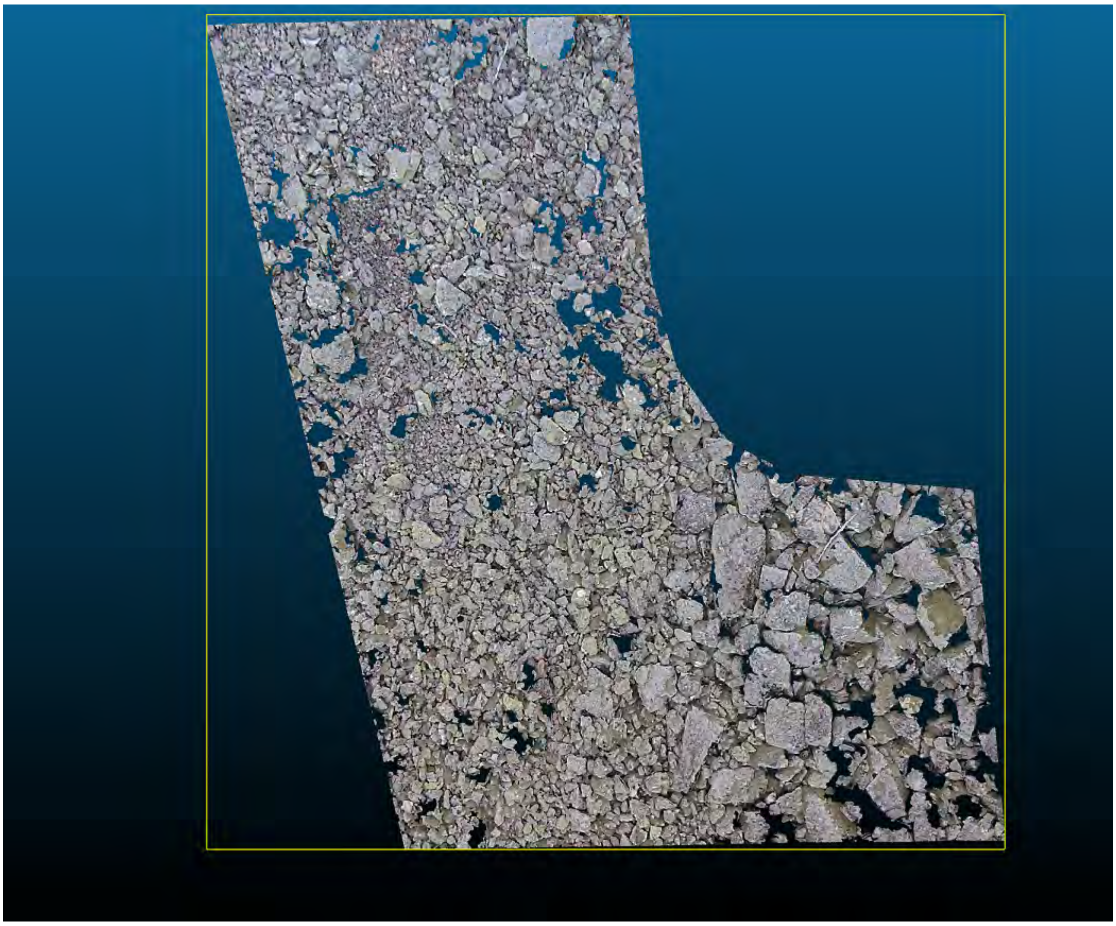

FIGURE 4.13: Image showing point cloud from the 2014 flight. The holes were cause by lack of tie points. The horizontal distance is roughly 25m. For this flight this was the densest part of the point cloud.

As seen in figure 4.12 it is clear to see that MicMac produced the fullest point cloud for flight 3. Flight 1 displayed the lowest amount of coverage and the most holes. In figure 4.12 the length of the flight 1 point cloud is about half that of flight 2. This was expected due to the flight height and low quality of the images from flight 1. The bright sun also may have played a role in the poor results.

The sporadic flight pattern of the UAV in the June 2014 flights made the images difficult to process. To work with these images small groups were selected. Figure 4.13 shows one of these groups. When more images were processed at the same time The holes are due to lack of data. With a more powerful computer or with more time it would have been possible to create a more comprehensive point cloud, but with the resources and time available this point cloud and corresponding orthoimage (Fig. 4.15) will represent the June 2014 flights for this thesis.

Figure 4.14: Image showing orthoimages from the three flights. The color anomaly seen in flight 2 appeared after Vodka processing to remove the vignette. This region was cropped out for analysis.

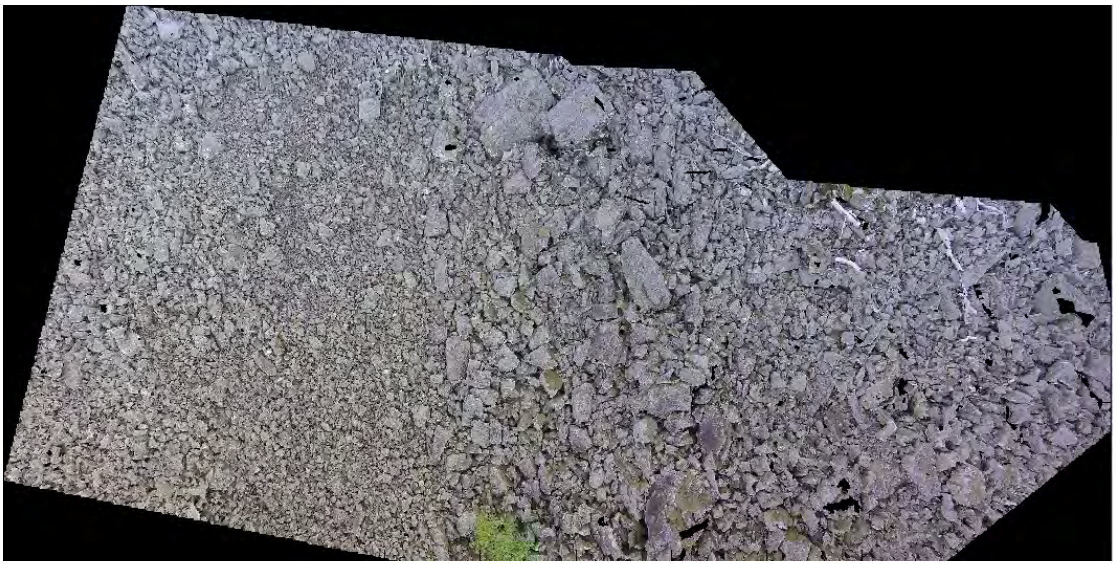

Figure 4.15: Image showing orthoimage from the June 2014 flight. The camera used had a strongly distorted lens. The distortion has been accounted for, but the edges of the orthoimage appear to be stretched.

4.3.2 Orthoimage reproducibility

This section will cover the comparison of orthoimages from the three aerial surveys of June 2013 and the 2014 orthoimage. The goal of this section is to determine the effects that camera, lighting, and angle have on the reproducibility of orthoimages. Comparison is done by matching feature points between images and running cross correlation to see if any movement occurred. Movement seen in orthoimages from the same day shows that the matching of the is not correct, since the scree slope is stable and no movement was seen. To do this analysis a series of MatLab codes were used. The full package of codes will be made available. These codes are modified versions of the matching code matching.m used for grain size analysis. The details will not be discussed in depth. The three orthoimages from the flights (O1,O2,O3 respectively) were compared against each other. The orthoimage from the 2014 survey will be references as O4.

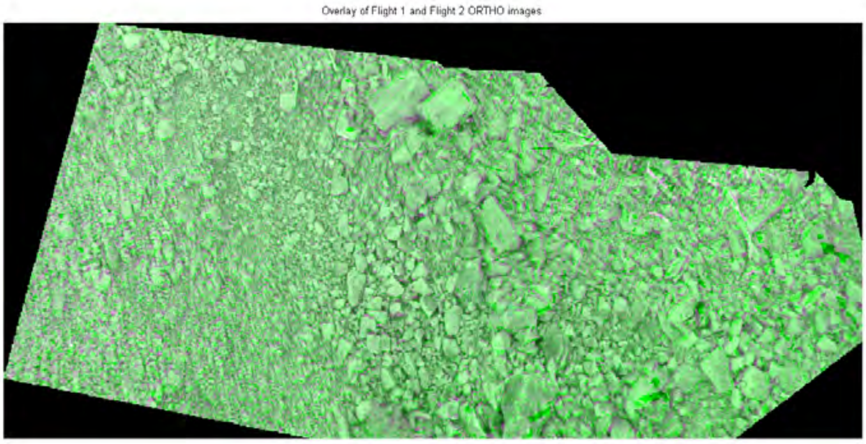

Figure 4.16: Image overlay between O2 and O4. The matching for this image was done by manually selecting feature points. Automated matching showed similar results. The ability to match orthoimages with such high accuracy between completely different surveys is significant.

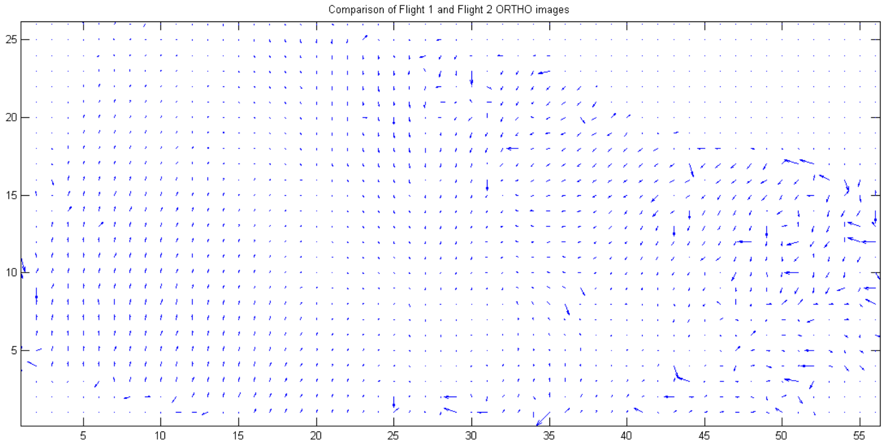

Figure 4.17: Correlation map of the orthoimages O2 and O4. Manual matching techniques were used. Despite the image color differences MATLAB was able to identify points and monitor movement. The movement is believed to be an due to the static state of the scree slope. The maximum translation vector for this plot is 31 cm. The axis are in meters

Figure 4.16 shows the difference in the O2 and O4 after manual matching. Automated matching had similar results. The correlation map in Figure 4.17 shows that the orthoimages are close enough to be recognized by MATLAB. Matching between the 2014 flight and the 2013 flights worked for flights 2 and 3. The resolution of flight 1 was too low to make any correlation. This suggests that the camera used has a limited effect on the creation of orthoimages. The sunny lighting of flight 1 or the slightly out of focus images may be causing the matching to fail.

The small displacements throughout the correlation map (Fig. 4.17) are smallest in the center of the orthophoto. This suggests that the orthoimages are more accurate in the center. Looking at Figure 4.15 slight distortion can be seen near the edges. Aside from distortion, the images must be rescaled, meaning one loses resolution. Perhaps if the resolution was more similar some of the small differences would be eliminated. The resolution of the orthoimages for O2 and O4 are 2.5 cm/pix and 1.1 cm/pix respectively.

Figure 4.18 shows the displacement vectors from cross correlation between the orthoimages from 2013. As with the 2013/2014 comparison it is clear that flight 1 does not match properly. Flights 2 and 3 show correlation. The center of flight 1 shows some correlation near the center when matched with flight 2. Looking at the overlay of the flight 1 and flight 2 orthoimages there is a clear offset (Fig. 4.19). This is evident when looking at GCPs. The matching method used only scales and translates. There is no distortion. This is to preserve the georeferencing. The fact that the flight 1 orthophoto is skewed may be related to the blurry images and different coverage region. Resolution and focus should be key points to remember when capturing images to avoid this problem in the future.

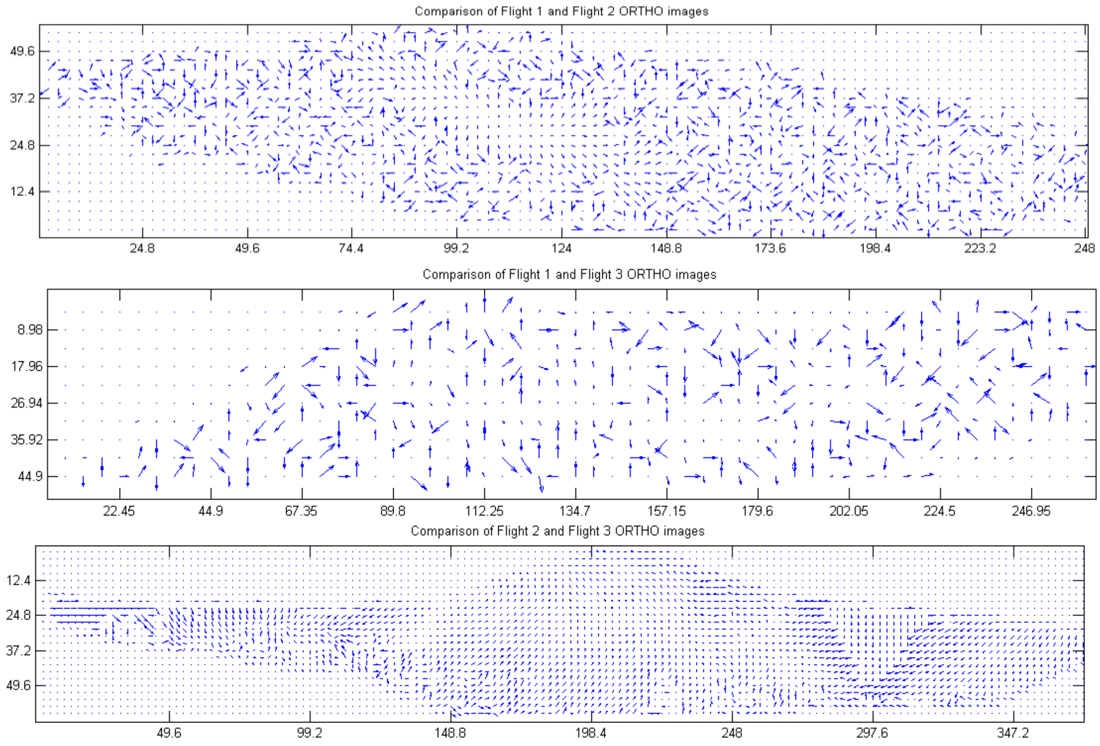

FIGURE 4.18: From top to bottom are displacement vectors between O1/O2, O1/O3, and O2/O3. The maximum vector length for O1/O2 is 2.48 m, O1/O3 is 3.84m, and O2/O3 is 23cm. Each vector represents the average displacement for a 2.2m x 2.2m region of the orthoimage. The axis are in meters. The O1/O3 plot is inversed.

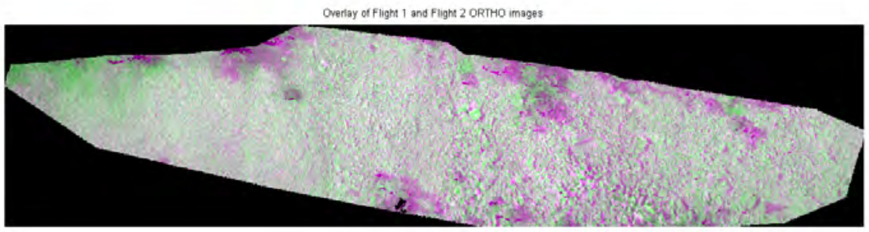

FIGURE 4.19: Overlay image between flight 1 and flight 2 ortho images. The corresponding correlation map is Figure. 4.18. Looking at the GCPs it is clear that matching has failed.

4.3.3 Point cloud comparison

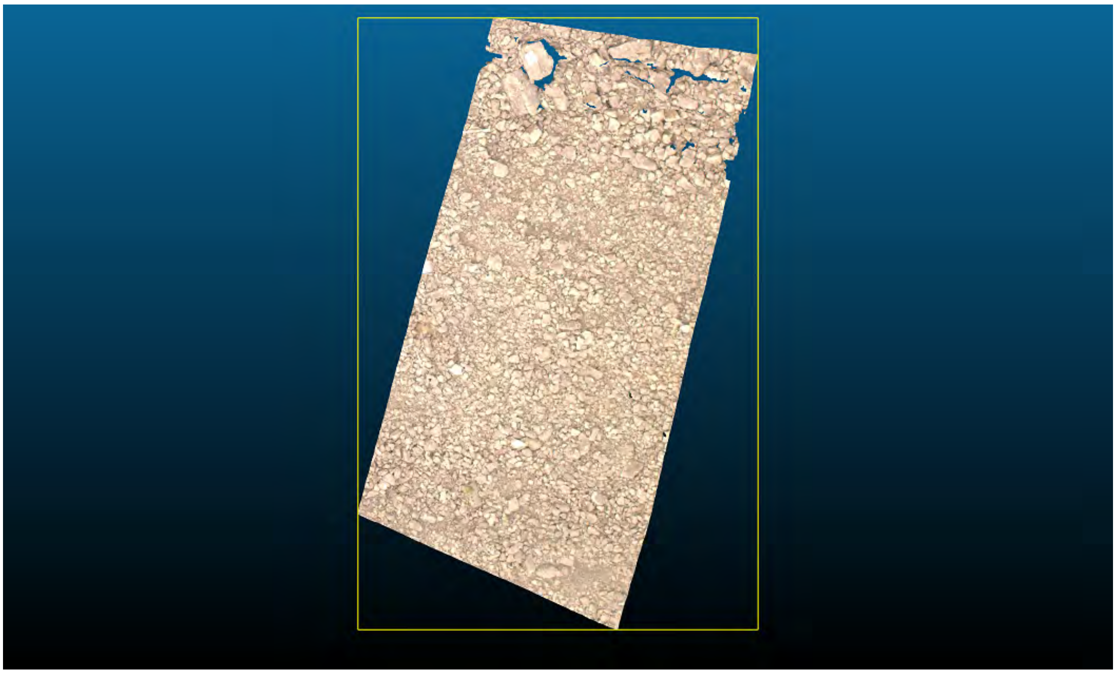

Figure 4.20: Ortho image from CloudCompare processing showing the region used for point cloud comparison. The selected section is 25 m across.

CloudCompare was used for point cloud comparison. The result are displayed as the minimum distance between one point cloud and the other. The average value is taken for a set of pixels. This value is assigned to a pixel in the digital elevation model "DEM". The distances are an absolute value. This is done because the point clouds may intersect and pass through each other. The function name in CloudCompare is "Cloud/Cloud dist.". The point clouds were already oriented when imported into cloud compare. For each comparison a cloud matching algorithm, "Fine Registration", was run to find the best fit. The function uses an iterative sequence to minimize distance values. The transformations used were only rotational and translational. The scale remained constant and there was no skew. This removes any small differences resulting from manual georeferencing between the survey. As seen in Figures 4.21,4.22,4.23 the differences in point clouds are not dependent on grain shape.

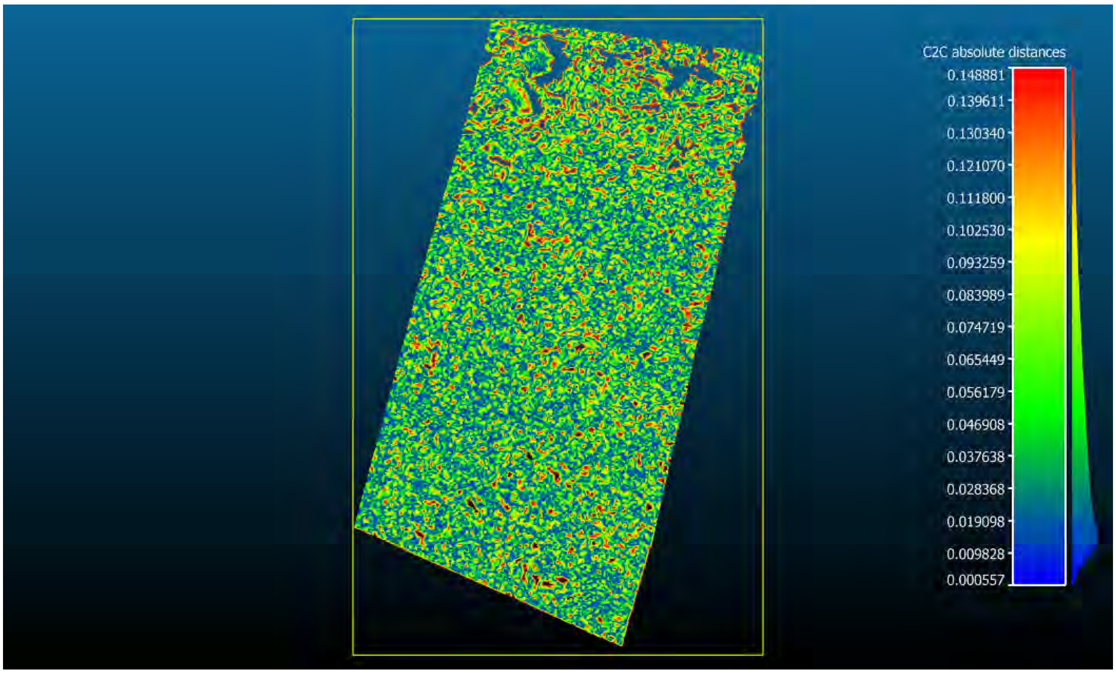

FIGURE 4.21: Point cloud difference between flight 1 and flight 2. Colorbar is in the scale of meters and the right side is a histogram for the displacement of points.

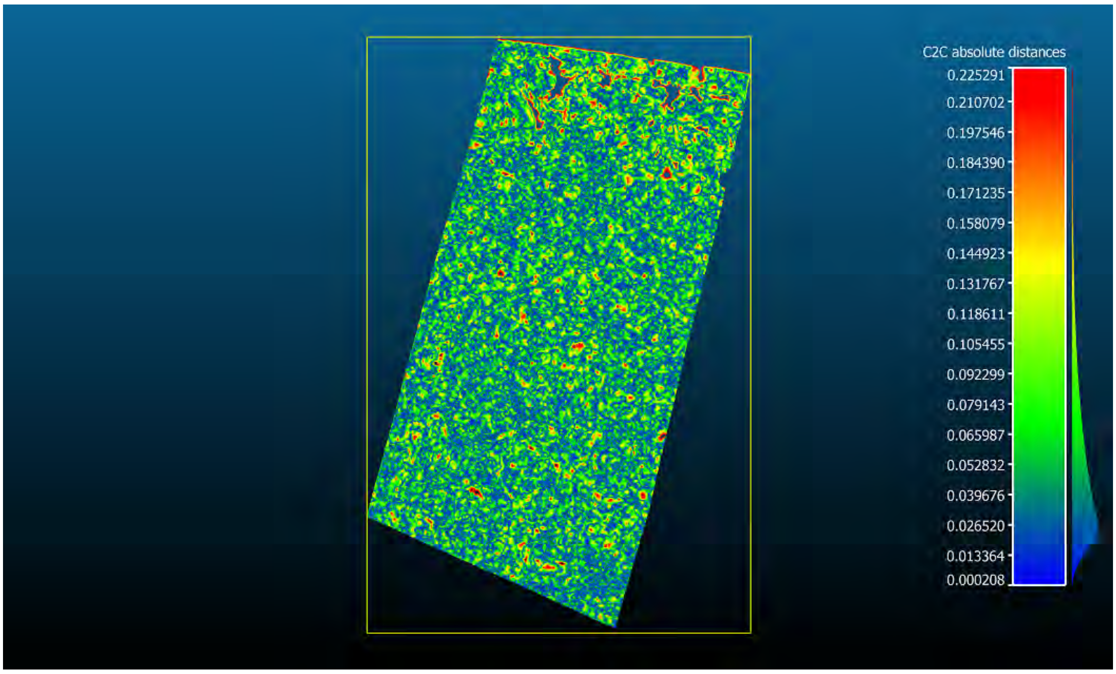

FIGURE 4.22: Point cloud difference between flight 1 and flight 3. Colorbar is in the scale of meters and the right side is a histogram for the displacement of points.

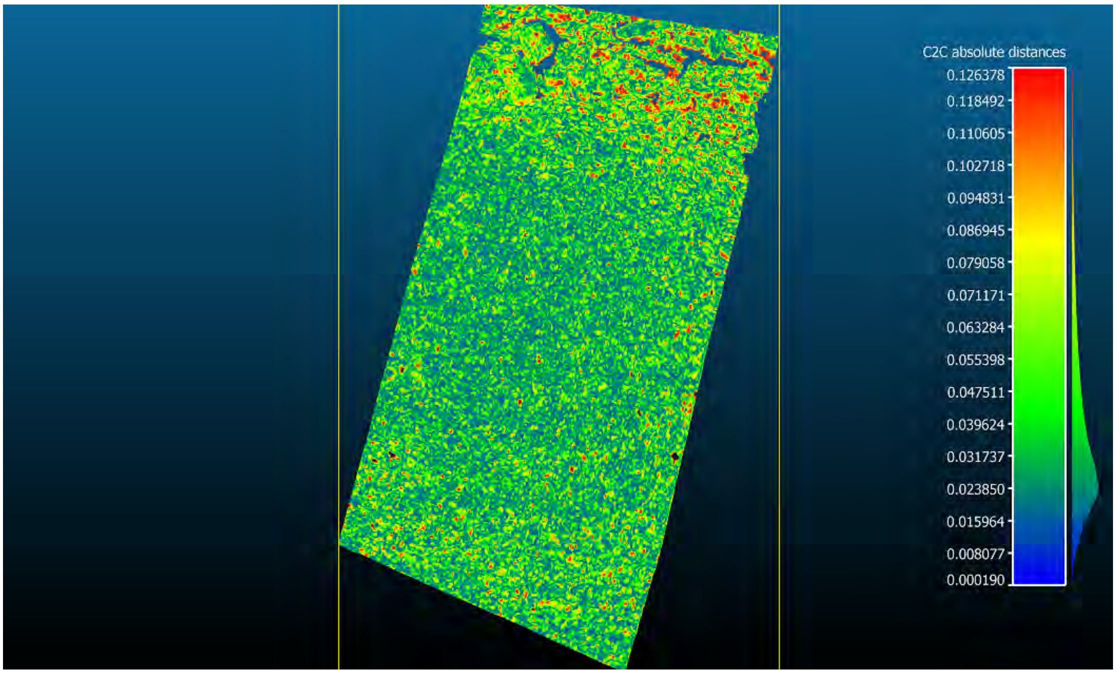

Figure 4.23: Point cloud difference between flight 2 and flight 3. Colorbar is in the scale of meters and the right side is a histogram for the displacement of points.

The colorbar on the right side of the figures shows the offset between point clouds in meters. The right side of the colorbar is a histogram showing number of points with selected offset. The average values for offset are between 1 cm and 3 cm. With respect to the resolution of the original images the results show sub-pixel resolution. The areas with most offset are around the edges of larger particles. This may be due to the different angles of viewing. Line of sight changed between flights. Monitoring very small movement may be difficult to to the noisiness of the results. Monitoring small rock movement would be very difficult.

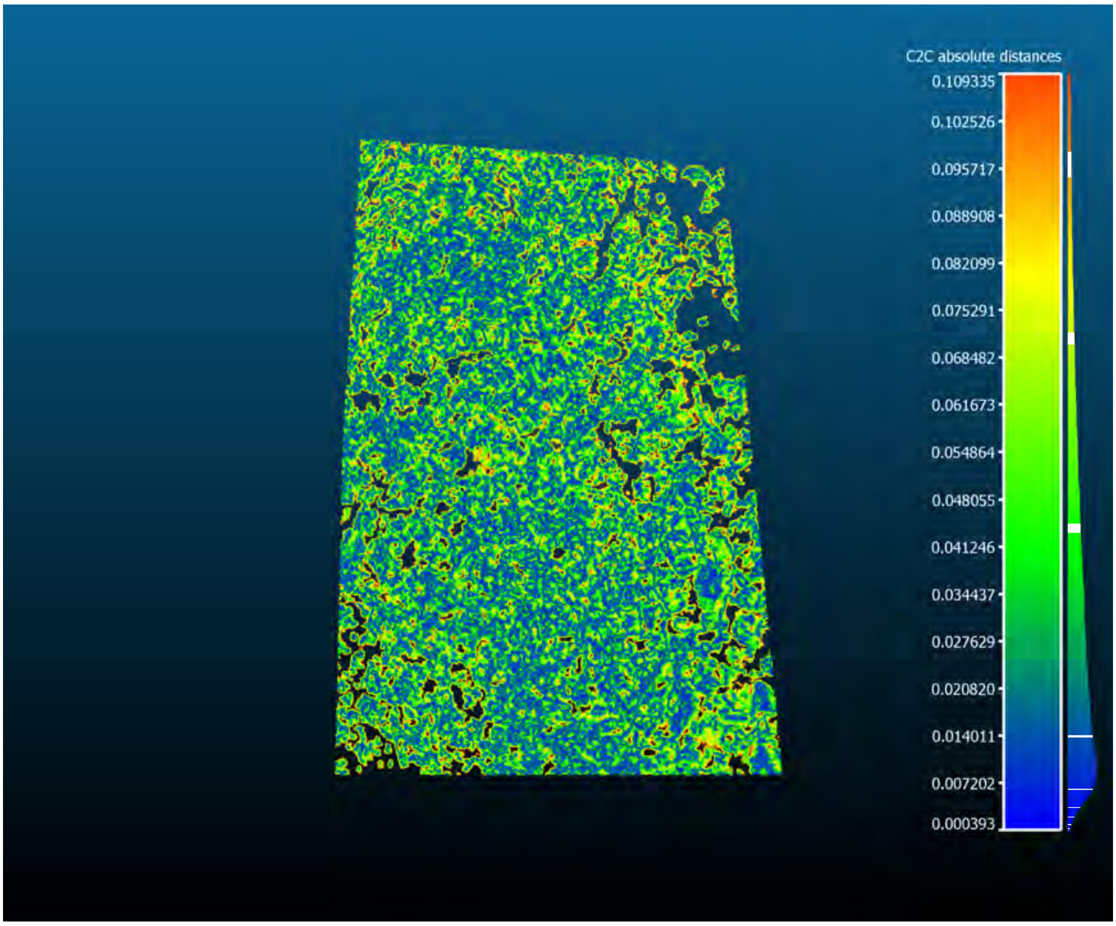

Figure 4.24: Cloud comparison between the June 2014 point cloud and the flight 3 pointcloud. All holes were present in the original point clouds. The colorbar is in the scale of meters.

The point cloud from the June 2014 surveys (Fig. 4.13) is used for determining the dependence on camera, lighting, and survey techniques. The first problem with comparing this point cloud is the presence of holes. These holes can be removed by limiting the maximum range for point cloud comparison values. The June 2014 data was not georeferenced during the survey. Feature points can be selected in CloudCompare to align point clouds. The feature is called "Align". Rotation, translation, and scale are used to fit the point clouds. The point clouds are never skewed. Translation information can be exported. Once the point clouds are aligned using feature points the iterative matching feature, "Fine Registration" can be used to find the optimum fit. A quick visual check will confirm if the point clouds are matching. "Cloud/Cloud dist." is then used to calculate distances. Figure 4.24 shows the results of the cloud comparison. The distances fall under 10 cm with the mode of the data showing 1cm distance. This is the resolution of the data from the June 2014 dataset, and it is much less than the 4 cm/pixel resolution from the flight 3 data. The point cloud quality was not dependent on the camera.

In conclusion, point clouds can be created in different light conditions using different cameras. It is important to ensure proper coverage of the study region to ensure significant coverage. Using the methods described above it is possible to monitor slope morphology over time without a permanent monitoring installation. The results are also independent of camera type. It is recommended to try to maintain equal or higher resolution between surveys to ensure no loss of data quality.

4.3.4 Orthoimage grain size

For extracting grain size information there is a wide range of techniques. Many were tried in this thesis, but only a small portion of the results are displayed. No in-field surveys were completed, as the analysis must be visually assessed for accuracy. Sections of the ORTHO and DEM were selected for analysis so assess the quality of the grain extraction process. The goal is to separate the grains on the visual boundaries seen in the images using both the orthoimages and DEMs. Proper computational results could then be calibrated by size comparisons with in-field surveys, but that was not completed in this thesis.

The basic workflow can be seen in Figure 3.15. Two steps provide results. The watershed.m function and the combine_grains.m function. watershed.m does a good job of defining smaller grains. Edge detection techniques used in combine_grains.m does good job at detecting larger grains. The goal of combine_grains.m is to combine both methods so the large grains and small grains appear on the same grain map.

Figure 4.25: Watershed analysis for ortho (left) vs. Watershed for DEM (right). Flight 1

This is still a work in progress. The images taken in the 2013 surveys are mostly too low resolution to properly image the smaller grains. Figure 4.25 show an excerpt from an unprocessed image. The small grains surrounding th larger grains are barely visible. For this reason, it can be expected that the grain size curves from flights with lower resolution will be under-segmented. A good test of this is to compare the results from the June 2014 survey with a the flights from 2013. The later having much lower resolution. The results in Table 4.3.4 are from the watershed.m function as the combine_grains.m function is still being worked on to produce better results. The resolutions are not the resolution of the images. Then are instead the resolution of the orthoimages. Flight 3 had higher resolution images but flight 1 has a higher resolution orthoimage. The June 2014 flight has by far the lowest mean value. This is due to the large number of small grains accounted for in the processing. The June 2014 showed proper segmentation of grains using watershed.m (Figs. 4.26,4.27). In contrast the flight 3 data does not show the same level of segmentation . The lower resolution makes the small grains rounder and thus harder to identify. The limiting size for grains seems to be 4x4 pixels. Thus the grain size curve is only valid for grains with size over that threshold. It must be noted that the June 2014 data covers a region inside the flight 1,2,3 data. The total coverage area is not the same.

Flight number	Mean (m ^{2})	Standard Deviation	Number of grains	Resolution (m/pixel)
1	0.179	0.175	6456	0.038
2	0.156	0.227	6870	0.025
3	0.166	0.259	6334	0.045
June 2014	0.020	0.0758	9538	0.0106

Table showing grain size distribution data for the watershed.m analysis of orthoimages. The number of grains can be used to compare flights 1,2,3 data as they are for the same region. but the June 2014 survey only covers a portion of the same region.

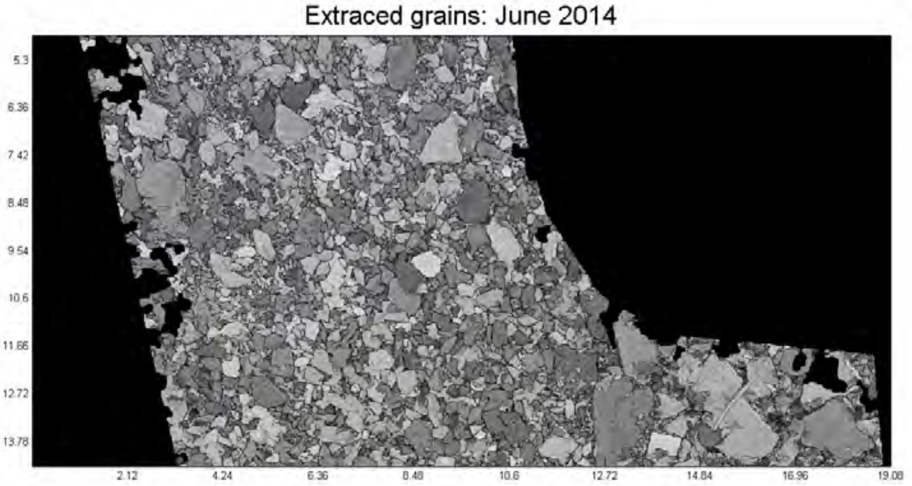

Figure 4.26: Grain boundaries from the June 2014 survey. Grain boundaries found using watershed.m

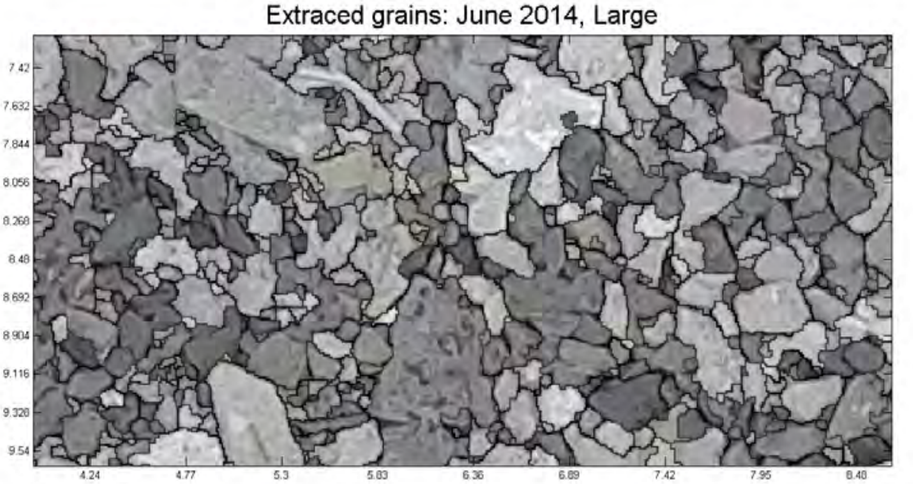

Figure 4.27: Close up view of grain boundaries from the June 2014 survey. Grain boundaries found using watershed.m

In contrast the flight 3 data does not show the same level of segmentation . The lower resolution makes the small grains rounder and thus harder to identify. Figures 4.28 and 4.29 show proper grain segmentation for what is visible. The limiting size for grains seems to be 4x4 pixels. Thus the grain size curve is only valid for grains with size over that threshold. The higher the resolution of the image the finer the grain size distribution will be. This is seen in Table 4.3.4, with the exception of flight 3. This can be attributed to the lack of focus in the flight 1 images. Comparing cumulative distribution plots of grain size data shows the same trend (Fig. 4.30). Data from DEMs analysis showed similar results (Fig. 4.31). However in this case the 2013 flights did not show correlation to resolution. This may be attributed to the inaccuracy of DEM segmentation.

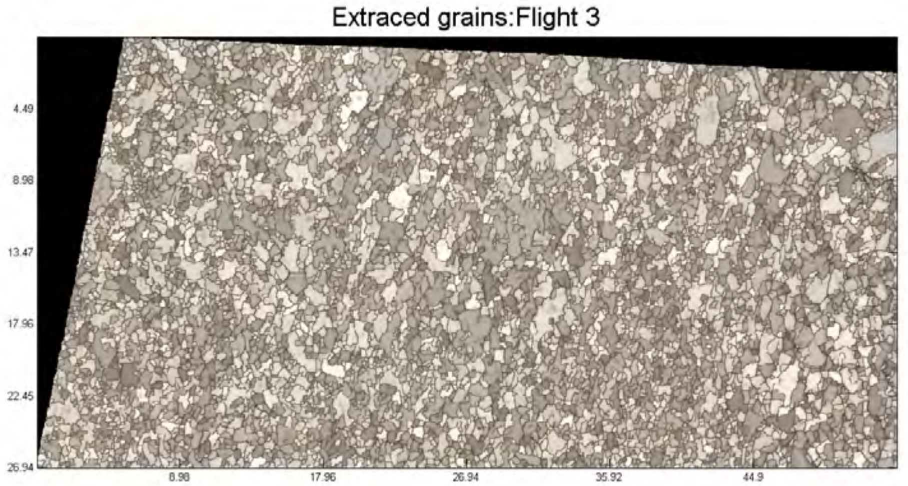

Figure 4.28: Grain boundaries from the flight 3 survey. Grain boundaries found using watershed.m

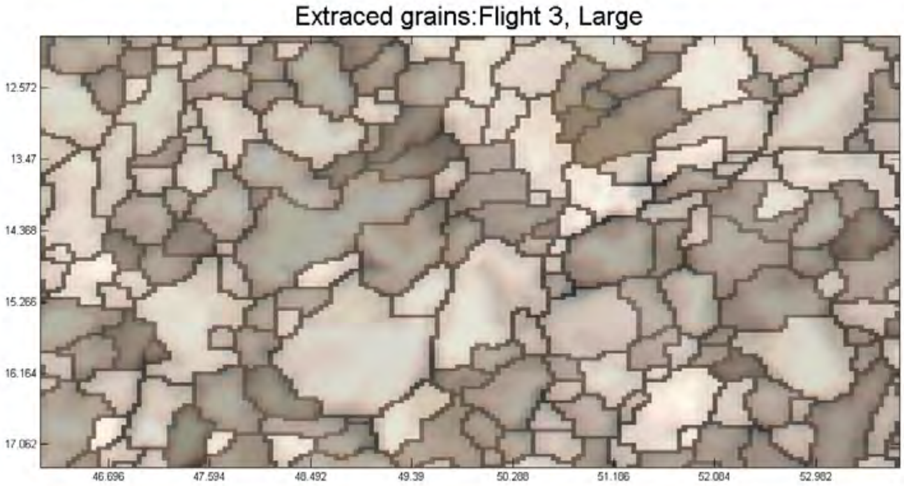

Figure 4.29: Close up view of grain boundaries from the flight 3 survey. Grain boundaries found using watershed.m This is nearly the same location as Figure 4.27.

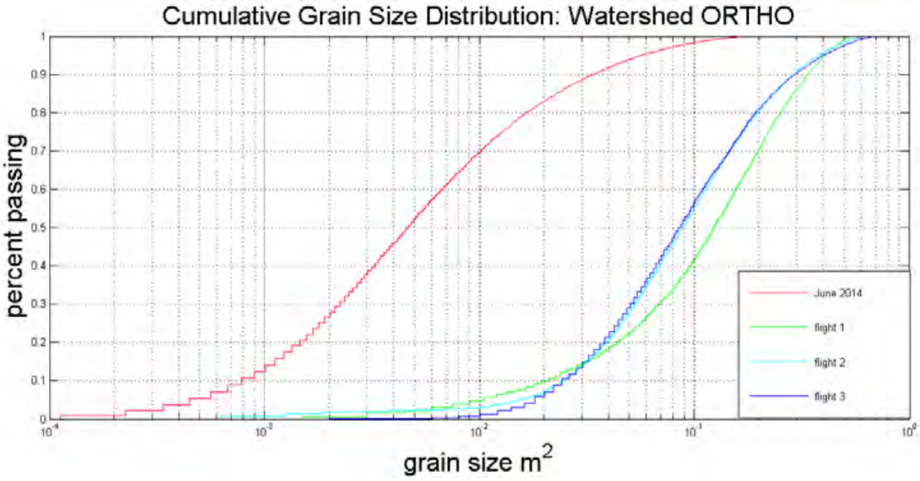

Figure 4.30: Cumulative grain size distribution of orthoimages. Data comes from watershed segmentation. Note that the June 2014 survey shows the smallest grain size distribution. This can be attributed to the higher resolution of the imaging.

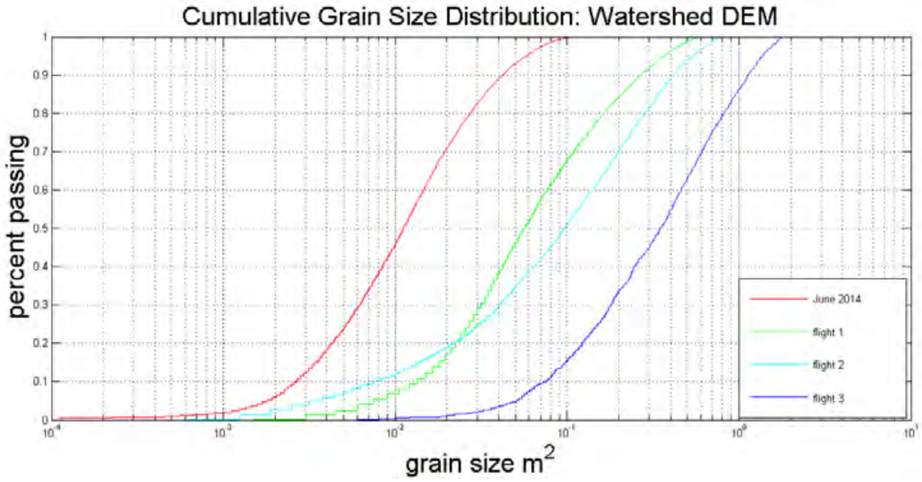

FIGURE 4.31: Cumulative grain size distribution of DEMs. Data comes from watershed segmentation. Note that the June 2014 survey shows the smallest grain size distribution. This can be attributed to the higher resolution of the imaging.

The difference between orthoimage segmentation and DEM segmentation is very clear. For accurate grain size analysis orthoimage segmentation outperforms DEM segmentation. Certain values need to be set when processing DEMs with the watershed.m function. The most important is the watershed_threshold (variable name in watershed.m). This defines the minimum indentation this can be considered a watershed. Low values will result in over-segmentation, high values will do the opposite. Certain image filters can enhance the visible boundaries on an orthoimage. This is not possible with the DEM. That is why the DEM results from watershed.m analysis are so different from the orthoimage results (Table 4.3.4). A comparison of the difference in grain separation using watershed.m is seen in Figure 4.32. The same region is being analyzed in each. The DEM results properly segment some of the larger grains; the small grains are under-segmented. From visual analysis, the orthoimage segmentation is better.

Flight number	Mean (m^2)	Standard Deviation	Number of grains
1	0.134	0.222	8189
2	0.204	0.288	5089
3	0.574	0.0607	1847
June 2014	.0218	0.0430	8309

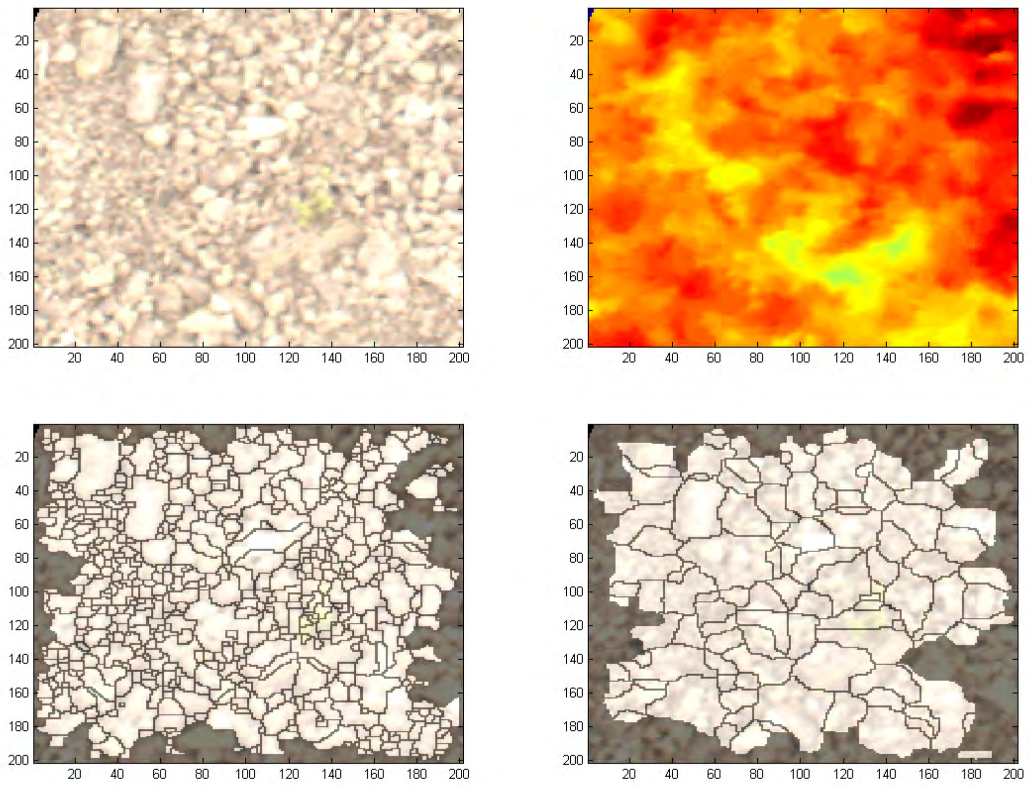

Figure 4.32: Segmentation of the same region using watershed.m on an orthoimage and DEM. The DEM under-segments the region.

Table showing grain size distribution data for the watershed.m analysis of DEMs. The number of grains can be used to compare flights 1,2,3 data as they are for the same region. but the June 2014 survey only covers a portion of the same region.

Separating and viewing ever grain is good for determining the proper values for the input variables. For larger regions it can be useful to map showing changes in average grain size. With respect to landslides, having a grain size map over a depositional fan could give information relating to flow dynamics or composition. This was completed by dividing an orthoimage into many small "pixels" and finding the average grain size for each. Figure 4.33 shows an example of this using the flight 3 orthoimage. The basic regions showing large and small grains are correct, however regions with the largest grains are not as visible. This may be because the algorithm for determining average grain size removes boundary grains from the pixels used. This reduces the average grain size. Larger pixels result in loss of detail. More research can be done on this.

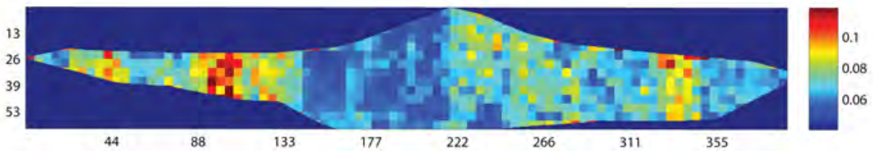

Figure 4.33: Figure showing average grainsize per area. This is a preliminary result. It correlates to the actual changes in grain size. The orthoimage used is from flight 3

4.3.5 Point cloud roughness

This step was completed to show the possibility of using roughness as an output. The roughness is calculated by giving a kernel size. This defines the region around a given pixel to analyze. The best fit plane in this region is calculated and the roughness is the distance between the center point and the best fit plane of its neighbors.

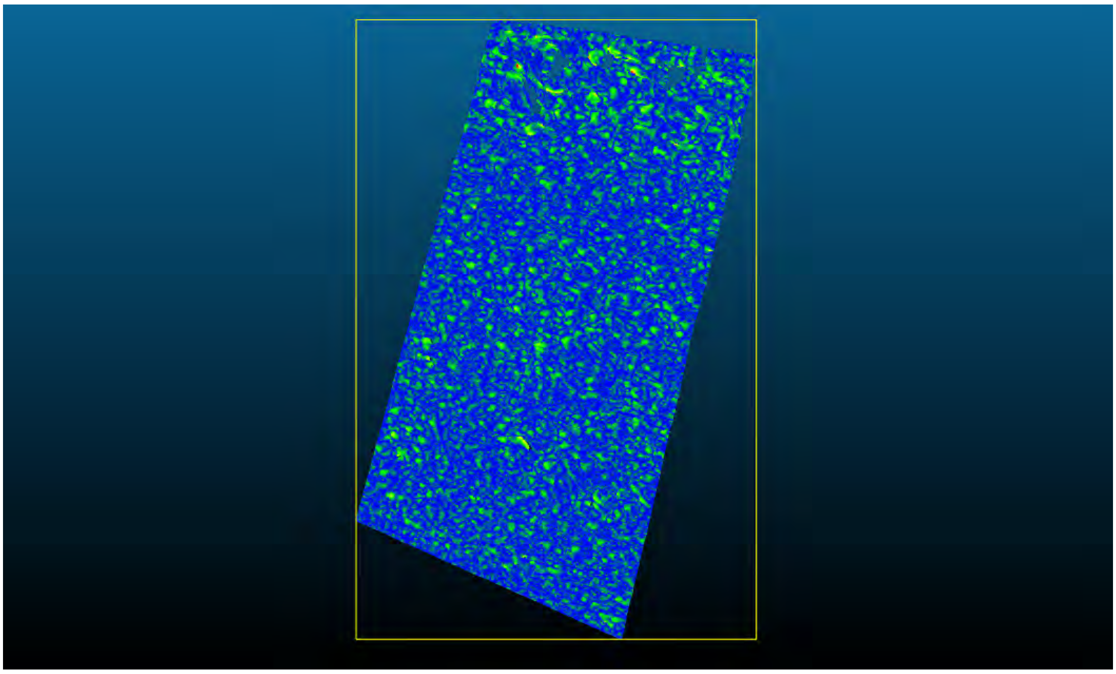

Figure 4.34: Roughness for flight 1 DEM.

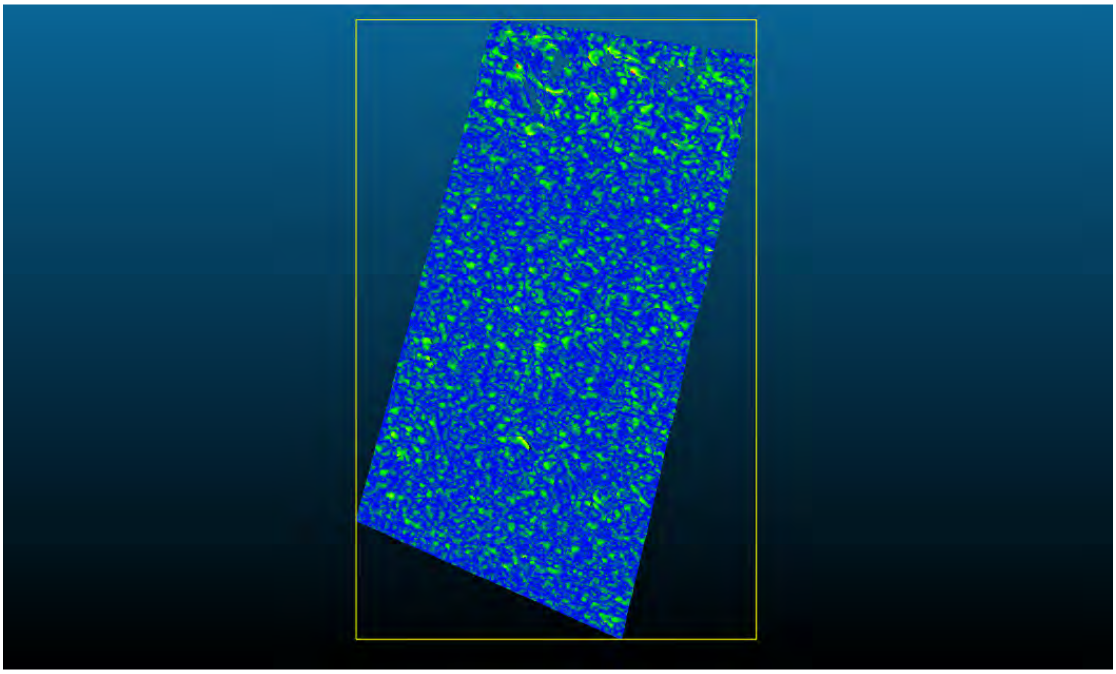

Figure 4.35: Roughness for flight 2 DEM.

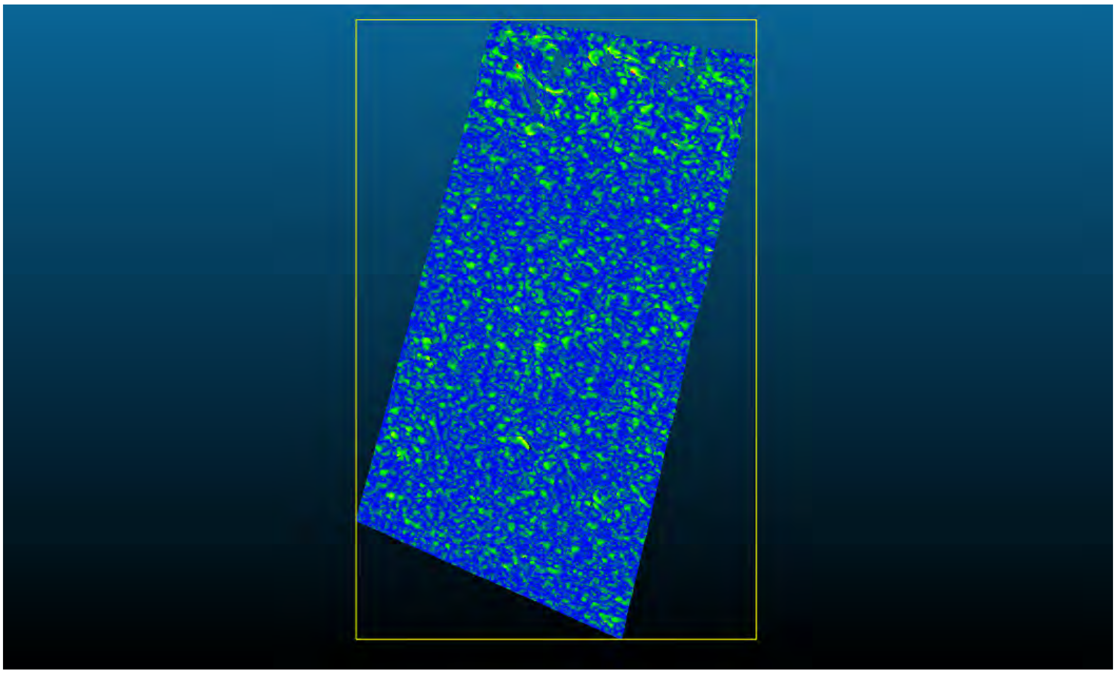

Figure 4.36: Roughness for flight 3 DEM.

The similarity between the roughness plots (Figs 4.34,4.35,4.36) show that this could be a possible course of further study. It is possible that roughness could be used to separate grains or be used to calculate grain size.

4.3.6 Cliff

As seen here, the a point-cloud was successfully calculated for the cliff. However, there are lots of holes and thus no further analysis will be completed. The fact that there are large holes after being imaged from 30 degrees to vertical shows the importance of proper imaging techniques. To properly image this cliff A UAV should be used with the camera normal to the cliff. Multiple passes at varying heights will ensure proper coverage.

FIGURE 4.37: Flight three DEM with overlying cliff section.

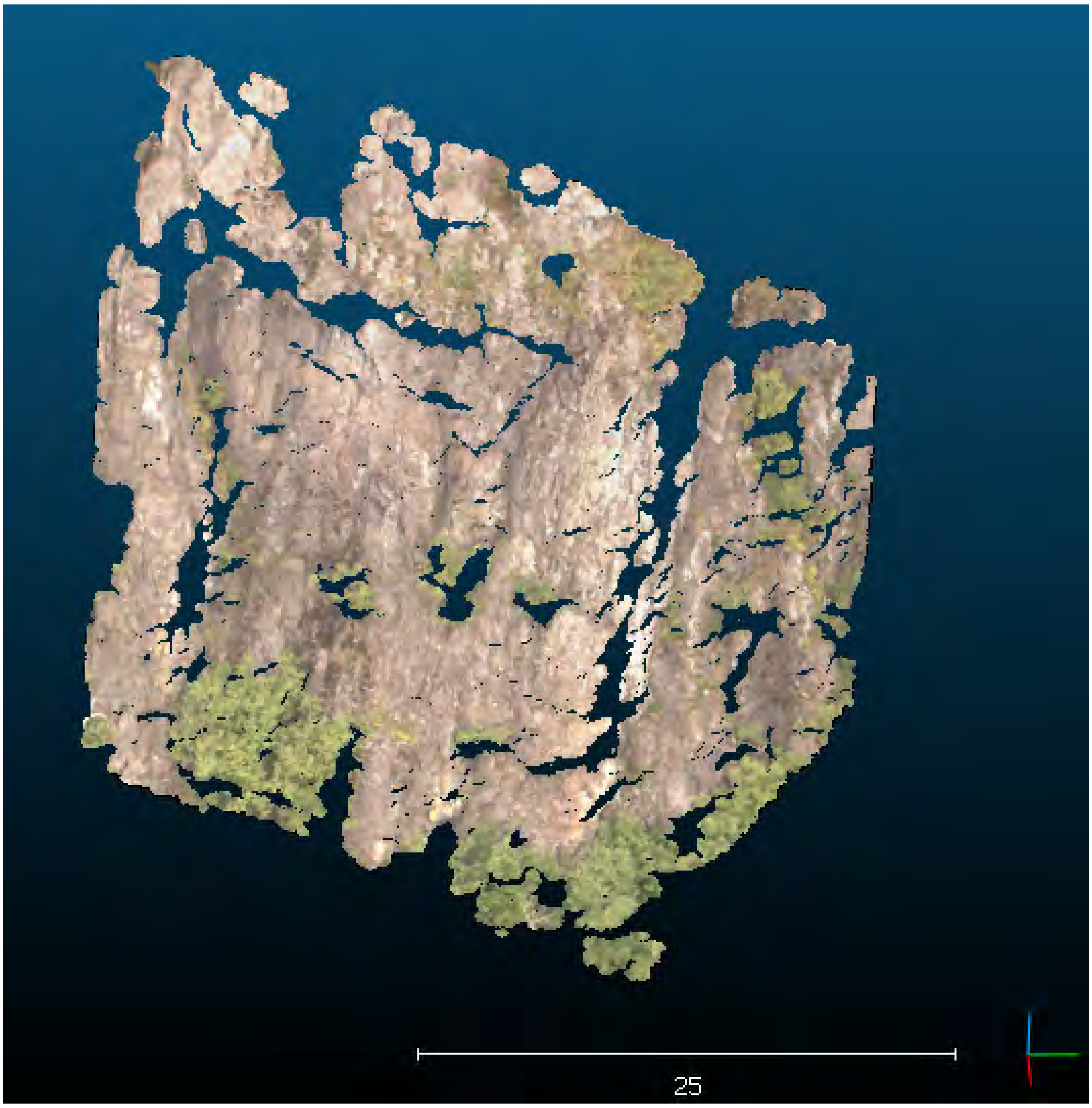

FIGURE 4.38: Closeup of the section of the cliff with the least amount of holes.

4.4 Discussion

The results from the Kolsaas field surveys are very promising. With the methods described it is possible to set up repeatable surveys to monitor changes with time. The results from preliminary surveys suggest sub-pixel accuracy between UAV surveys of the scree slope. Imaging technique is very important for obtaining quality results. It is maintain a constant distance, focus properly, and ensure adequate overlap between images.

The MATLAB code for analyzing grainsize still needs work, but is showing accurate results. Grain size segmentation works best using orthoimages. The dependency of grain size distribution on image resolution should be investigated further. It may be possible to predict real grain size from knowing partial grain size and resolution. This study did not have enough data to investigate this. Investigation to the effect of in-field contours may be important to investigate as well. This was not an issue at Kolsaas, but could definitely be an issue in other regions.

The problem of the flight 1 orthoimage not matching with the flight 2 and flight 3 images suggests that it has been skewed. This most likely means the vector normal to the orthoimage is different for flight 1. A possible way to avoid this is to select the bounding points for a study area and use the same points im MicMac processing every time. This would keep the orthoimage oriented properly.

The results thus far show repeatability is not dependent solely on equipment but also on technique.

Chapter 5

Future Work

5.1 Application to Active Slide

5.2 Fjaerland: glacial lake outburst flood

In order to confirm the repeatability of the photogrammetric procedures outlined in this thesis a survey was completed on an active slide location in Fjaerland, Norway. This location was the site of a glacial lake outburst flood (GLOF), resulting from the breech of a moraine dammed lake in 2004. The details of this slide are throughly described in Breien (2005) and Breien et al. (2008). Monitoring of the moraine could potentially help predict future debris flows.

The material associated with the sliding event was composed of predominantly glacial deposits. The depositional fan is composed of sub-angular granite/gneiss blocks (fig. 5.1). Most of the material throughout the slide path is similar to that seen in the fan. There are a few areas with exposed bedrock through the debris flow path. The top of the debris flow is a moraine. This moraine was built by the Little ice age of 1750. There is a smaller inner moraine (fig. 5.2) thought to have been created in 1930 during a glacial surge and retreat (Orheim (1970)).

A geophysical study by Lecomte et al. (2008) suggests that the 1750 moraine is partially saturated and that the 1930 moraine has an ice core. The absence of an ice core in the 1750 moraine makes it less likely to deform with time. Monitoring of the 1930 ice-core moraine could prove advantageous for understanding the morphology of ice-core moraines and potential points of weakness in the moraine.

Figure 5.1: Image looking up the Fjaerland debris flow from the base of the depositional fan. Photo taken fall 2013. The fan is composed of sub-angular blocks of granite and gneiss.

5.2.0.1 Slide history and future

The slide history in Fjaerland dates back centuries, but only recently have there been recorded events of glacial lake outburst floods. The first being in 1924 and the second being in 1947. The largest event was the 2004 slide. Comparing images from 1906 and 2001 it is clear to see that a portion of the moraine has been removed and that sliding a failure has Breien (2005).

It is believed that the breach scar seen in 5.3 is related to the failure in 1947. The slide of 2004 was the largest slide on record. The breach of the moraine removed much of the material. The walls on either side of the breach are quite steep and when walking over them I noticed they were quite unstable. According to a conversation with a local it is believed that the walls are eroding down and filling the bottom of the breach. Monitoring of this is crucial for determining the possibility of a new slide. Just to the inside of the breach is a smaller ice core moraine. Erosion of this moraine may also add to a build up of material in the breach zone. This ice-core moraine was actively eroding while the field study was taking place.

Figure 5.2: Image showing the moraine dammed lake. The moraine seen is a result of the 1750 little ice age (Orheim (1970)). The area highlighted in blue is the ice-cored moraine created during the glacial surge of 1930. The breach of the GLOF occurred on the right side of the moraine. The new moraine dammed lake can be seen (photo: fall, 2013).

Figure 5.3: Images of the moraine at Fjaerland. The left image is from 1906 the right is from 2001. A slight breach can be seen in the 2001 photo. In 2004 this notch opened to the ground. This figure is from Breien (2005).

5.2.1 Field methods

The field study consisted of four main survey regions. The river path, a cliff, the breach, and the moraine. Each trial was created to test the possibility of walking in field surveys of photogrammetry.

The river path is was the river gully where the 2004 slide passed through. The walls of the gully varied in composition with position on the hill. The majority of the walls were composed of rounded to sub-rounded grains with sizes from sand to 2m. There were also some larger ¿5m blocks. The goal of this part of the study was to see if convergent and aerial methods could be used to accurately map river gullies. The ability to routienly survey regions like this would allow for the calculation of volume change and erosion/deposition amount if two surveys were completed pre and post-slide.

A series of cliffs are located roughly 350 m downstream from the moraine. The cliffs are around 300 m vertical. The object of the cliff survey was not related to landslide or flood dynamics. It was a trial to see the power of terrestrial photogrammetry on cliff faces from a distance. The ability to image a cliff from hundreds of meters away on foot with limited lateral movement could prove to be a powerful tool when access is limited.

The breach was the main focus of this study. The ability to set up a method for repeated analysis of the moraine would help monitor the growth of a new dam. Comparisons of temporal data for the breach walls would help determine their stability as well

In the same way monitoring the breach is important temporal measurements of the moraine are also crucial for determining moraine morphology other possible weakpoints. Monitoring of the inner ice-core moraine would give important information about melt rates and ice-core moraine morphology.

Field methods were similar to those used during the aerial surveys at Kolsaas. The same principals were used to ensure adequate coverage over the study regions. One main difference was the inability to change the angle of the camera with respect to the survey region. When imaging the river gully and the moraine it was impossible to complete the survey from a vantage point normal to the surface. Another drawback of imaging of foot is the difficulty associated with imaging the same section from different angles. Most the surveys consisted of one path of images taken in a line. This limits the angular coverage which was available with aerial surveys at Kolsaas

Both ”aerial” and ”convergent” (3.3) survey methods were used in Fjaerland. Remember, aerial refers to imaging method and that all surveys in Fjaerland were terrestrial. Aerial methods were used for most of the surveys, convergent methods were used for the center of the river gully and the moraine breach.

5.2.1.1 Terrestrial field mapping

This section will discuss the difficulties and advantages of terrestrial photogrammetry experienced in Fjaerland. The main advantage is the speed at which surveys can be completed and the portability of the equipment. One camera was used for all the surveys and no other equipment was needed. To ensure better results I would recommend taking

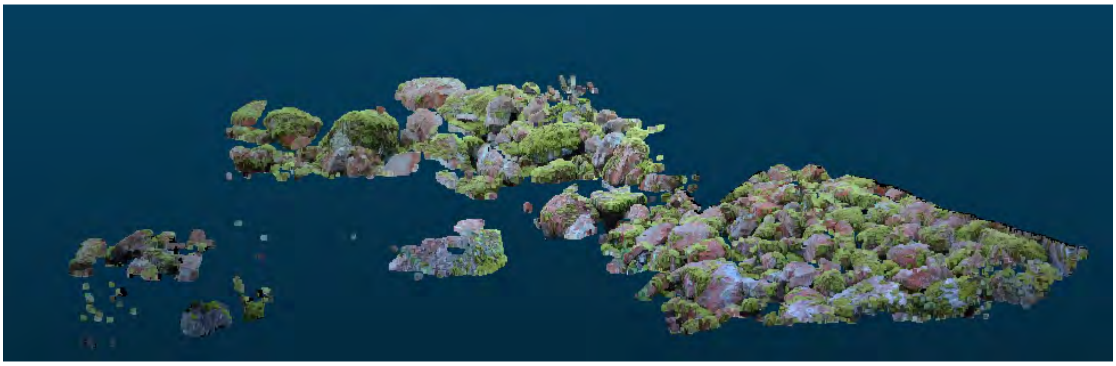

Figure 5.4: Point cloud resulting from photogrammetric analysis of 6 images taken from the bottom of the depositional fan (fig.5.1). This is from the point of view of the camera. The data appears to be usable for determining a limited particle size distribution of the region.

a tool for creating scale and a gps. However, this survey was completed in one afternoon and one morning, and the goal was to test software and the ability to set up easily repeatable and accurate methods for surveys.

One major disadvantage of terrestrial field mapping is the limited angles from which one can take photographs. A survey of the debris at the bottom of the tongue was attempted. It was immediately clear that from the low angle a full survey would be next to impossible. Using a set of 6 images taken from the access road a point-cloud was created for the bottom tongue. The fan has an average slope of 8-10 degrees (Breien (2005)). When viewed from the relative position of the camera it looks to show usable data. However when viewed from a vantage point normal to the fan it is clear the data is not a valid representation of the fan. This is due to line of sight problems, from such a low angle large boulders block the view to other rocks behind them. This is similar to the line of sight issues discussed previously in association to LiDAR. A quick aerial survey using an UAV could potentially cover this same region in a matter of minutes. Thus it is not enough to use a photogrammetry program to create an orthoimage. To ensure data quality both an orthophoto and a point cloud should be made.

This same problem experienced at the depositional tongue was also encountered in the river gully. The larger the rocks the greater the problem as they shadowed more of the region behind them. The grainsize distribution also appears to have an effect. Although this was not studied in depth, it appears that the more consistent size of grains makes this less of an issue. Further study is needed to determine if this is true.

Another difficulty associated with terrestrial surveys was the access. Around the bottom of the river gully there were lots of trees. This made imaging from the banks difficult. Surveys of the banks were completed from the bottom. This caused some of the same line of sight issues as mentioned above. For the cliff the issue was that the access trail

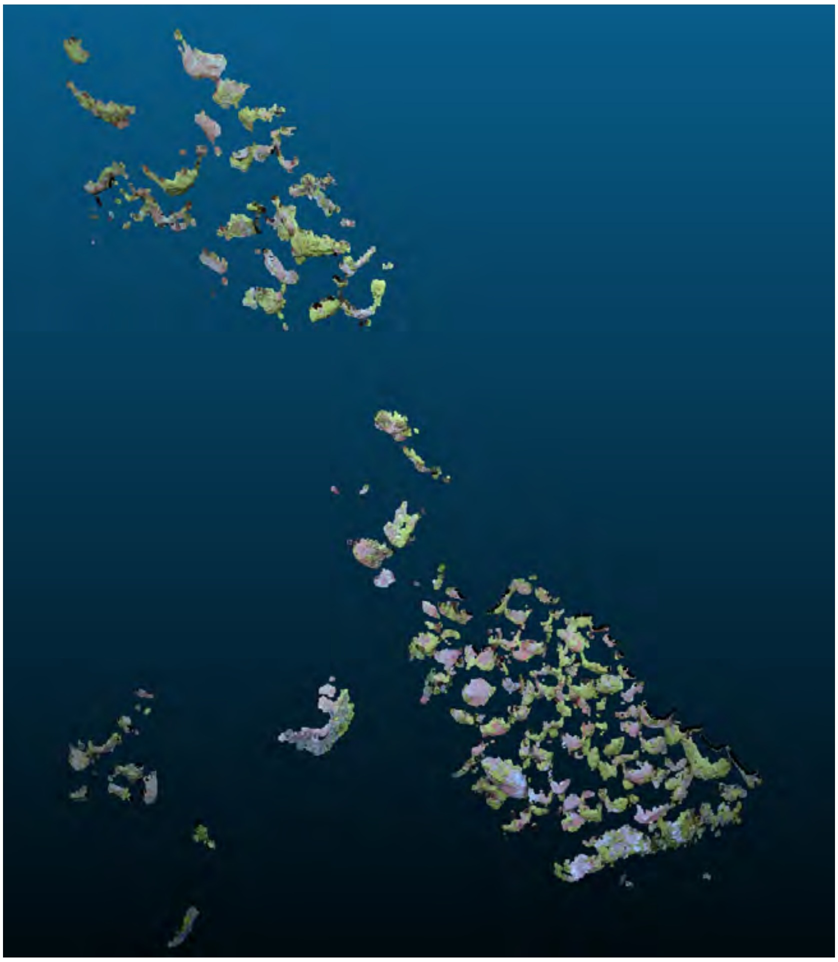

Figure 5.5: Point cloud resulting from photogrammetric analysis of 6 images taken from the bottom of the depositional fan (fig.5.1). This is from the point of view normal to the fan. From this angle it is clear the data is not adequate for any accurate analysis.

didn't approach the cliff. This caused the survey to be carried out roughly 200 m away. This wasn't much of an issue for a wide survey, but if detail is required than a high zoom value must be used. For this it may be better to have a tripod to eliminate image blur and ensure proper overlap.

With the moraine itself the best place to image it was from fairly close up. A few times terrain made it difficult to keep a constant distance. In full light this is not an issue as a high f-stop value can be used ensuring the largest depth of field. In low light this could result in out of focus images. Another issue encountered was the changing lighting conditions. The curved moraine cause drastic changes in lighting when imaging the outside of the moraine. This resulted in the need for multiple surveys. A distant aerial survey of the entire region using fewer pictures would enable a much faster computational analysis. The survey of the outer moraine consisted of 364 images. This amount of images would take a substantial amount of time to process. For this reason only certain sections of the moraine were processed. To create an overview of the entire moraine a wider, and ideally aerial, survey would be recommended. The low weight of UAV's such as those used at Kolsaas would make this easy to complete.

For the purpose of this study, terrestrial surveys proved to be good enough to create repeatable data. Stationed cameras from positions similar to those in this study could potentially give real time data of the region. For in depth analysis and to ensure spatial accuracy aerial surveys would be ideal.

5.2.2 Photogrammety results

The goal of this section is to show the potential associated with in terrestrial photogrammetry. There are only a few preliminary results. Figures 5.6, 5.7, 5.8 are three possible locations for future study. The cliff give an opportunity to create plane recognition software or maybe a rockclimbing guide. The ice-core moraine is an active landform which would be very interesting to monitor at steady intervals. The south side breach wall is important as erosion from this wall will actively re-dam the lake. Monitoring of this feature could prove to be important. These three features took no longer that five minutes a piece to image. That includes the unpacking/packing of equipment and note taking.

Figure 5.6: Point cloud of a cliff. This was imaged from roughly 200 meters away. The cliff is 50 m high. This point cloud show great detail.

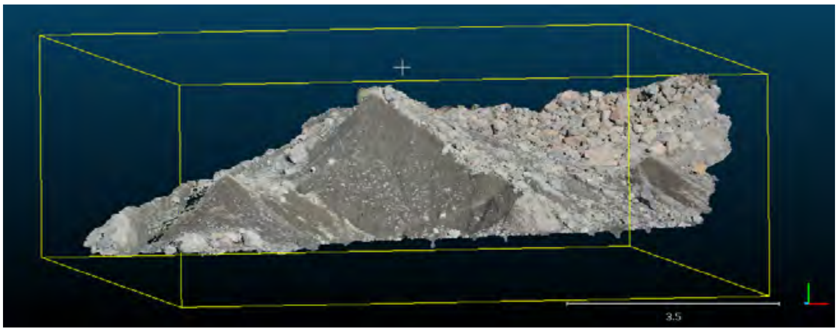

Figure 5.7: Point cloud of an ice-core moraine. Temporal monitoring of this would give information for erosion rates.

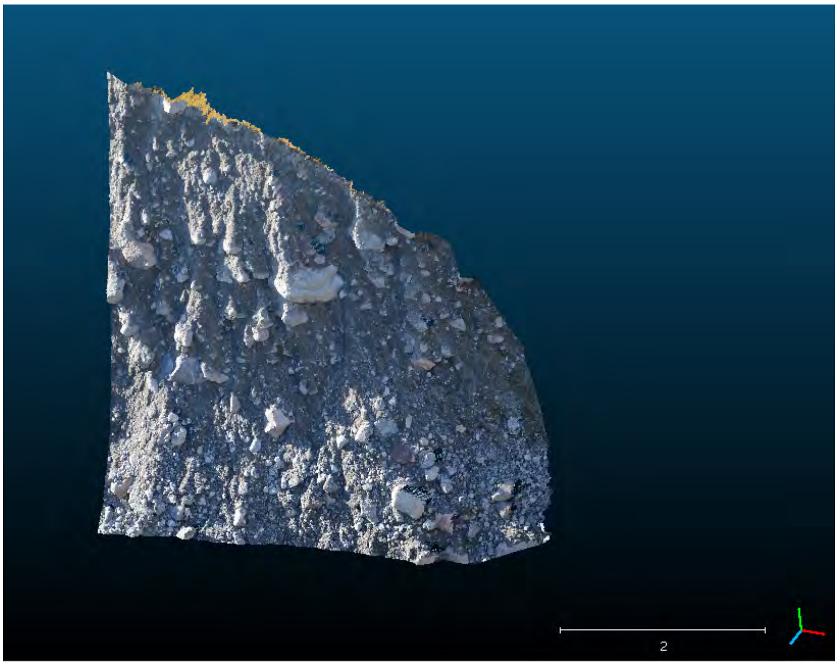

Figure 5.8: Point cloud of the south wall on the south side of the breach. This point cloud is composed of 4 images.

Chapter 6

Conclusions

6.1 Conclusions

The creation of a workflow for photogrammetric analysis of a landslide like environment was successful. The results showed sub-pixel accuracy is possible using different equipment image resolutions. This proves the method is reproducible. The data from the photogrammetric analysis can serve many purposes. The grain size analysis program created for this thesis successfully creates grain size distribution curves. However, the dependency on image resolution should be tested to verify the results.

The foundation built in this thesis can serve as a starting point for future studies and surveys

Bibliography

Abellán, a., Jaboyedoff, M., Oppikofer, T., and Vilaplana, J. M. (2009). Detection of millimetric deformation using a terrestrial laser scanner : experiment and application to a rockfall event. pages 365–372.

Abellán, a., Vilaplana, J. M., Calvet, J., García-Sellés, D., and Asensio, E. (2011). Rockfall monitoring by Terrestrial Laser Scanning – case study of the basaltic rock face at Castellfollit de la Roca (Catalonia, Spain). *Natural Hazards and Earth System Science*, 11(3):829–841.

Angeli, M.-G., Pasuto, A., and Silvano, S. (2000). A critical review of landslide monitoring experiences. *Engineering Geology*, 55(3):133–147.

Barraud, J. (2006). The use of watershed segmentation and GIS software for textural analysis of thin sections. *Journal of Volcanology and Geothermal Research*, 154(1-2):17–33.

Bertin, S., Friedrich, H., Delmas, P., Chan, E., and Gimel'farb, G. (2014). Dem quality assessment with a 3d printed gravel bed applied to stereo photogrammetry. *The Photogrammetric Record*, 29(146):241–264.

Bitelli, G., Dubbini, M., Zanutta, A., Scanning, L., and Sensing, R. (2003). TERRESTRIAL LASER SCANNING AND DIGITAL PHOTOGRAMMETRY TECHNIQUES TO MONITOR LANDSLIDE BODIES. pages 1–6.

Blasio, F. V. (2011). *Introduction to the Physics of Landslides*. Springer Netherlands, Dordrecht.

Breien, H. (2005). *On the dynamics of debris flows*. PhD thesis.

Breien, H., Blasio, F. V., Elverhø i, A., and Hø eg, K. (2008). Erosion and morphology of a debris flow caused by a glacial lake outburst flood, Western Norway. *Landslides*, 5(3):271–280.

Buckley, S. J., Howell, J., Enge, H., and Kurz, T. (2008). Terrestrial laser scanning in geology: data acquisition, processing and accuracy considerations. *Journal of the Geological Society*, 165(3):625–638.

Burns, R. (1993). Richard Burns, PLS Caltrans Geometronics Introduction.

Buscombe, D. (2013). Transferable wavelet method for grain-size distribution from images of sediment surfaces and thin sections, and other natural granular patterns. *Sedimentology*, pages n/a–n/a.

Butler, J. B., Lane, S. N., and Chandler, J. H. (1998). ASSESSMENT OF DEM QUALITY FOR CHARACTERIZING SURFACE ROUGHNESS USING CLOSE RANGE DIGITAL. *Photogrammetric Record*, 16(October):271–291.

Butler, J. B. and Place, D. (2002). Automated extraction of grain-size data from gravel surfaces using digital image processing Acquisition automatique des données de granulométrie des surfaces de gravier par un procédé d ' imagerie numérique. 39(4):1–11.

Butterworth, M. (2012). Digital camera calibration method. *US Patent 8,094,195*, pages 266–272.

Clery, I. (2013). InterfaceMicMac User Documentation. pages 1–55.

Collins, B. D. and Stock, G. M. (2012). GeoCongress 2012 © ASCE 2012 3021. pages 3021–3030.

Corsini, a., Borgatti, L., Cervi, F., Dahne, a., Ronchetti, F., and Sterzai, P. (2009). Estimating mass-wasting processes in active earth slides – earth flows with time-series of High-Resolution DEMs from photogrammetry and airborne LiDAR. *Natural Hazards and Earth System Science*, 9(2):433–439.

Cruden, D. M. and Masoumzadeh, S. (1987). Accelerating creep of the slopes of a coal mine. *Rock Mechanics and Rock Engineering*, 20(2):123–135.

Dons, J. and Gyory, E. (1967). PERMIAN SEDIMENTS , LAVAS , AND FAULTS IN THE KOLSÅS AREA W OF OSLO. *Norsk Geologisk Tidsskrift*, 47:57–77.

Eckardt, A., Börner, A., and Lehmann, F. (2009). The Bright Future of High Resolution Satellite Remote Sensing – Will Aerial Photogrammetry Become Obsolete ? pages 127–134.

Georgantas, A. (2012). An Accuracy Assessment of Automated Photogrammetric Techniques for 3d Modeling of Complex Interiors. *...Archives of the ...*.

Girod, L. (2012). The use of SfM technologies in geosciences: MicMac for geologists. Technical report, University i Oslo.

Goor, B. V. (2011). *Change detection and deformation analysis using Terrestrial Laser Scanning.* PhD thesis.

Heritage, G. L. and Milan, D. J. (2009). Terrestrial Laser Scanning of grain roughness in a gravel-bed river. *Geomorphology*, 113(1-2):4–11.

Hodge, R., Brasington, J., and Richards, K. (2009). In situ characterization of grain-scale fluvial. 968(April):954–968.

Javernick, L., Brasington, J., and Caruso, B. (2014). Modeling the topography of shallow braided rivers using Structure-from-Motion photogrammetry. *Geomorphology*, 213:166–182.

Koch, M. and Kaehler, M. (2009). Combining 3D laser-Scanning and close-range Photogrammetry-An approach to Exploit the Strength of Both methods. *Making History Interactive. Computer Applications . . .*, pages 1–7.

Komamura, F. and Yamamori, T. (1988). On the Forecast of Time to Failure of Slope (II) the. 3:11–17.

Larsen, B., Olaussen, S., Sundvoll, B., and Heeremans, M. (2008). The Permo-Carboniferous Oslo Rift through six stages and 65 million years. *Episodes*, (March):52–58.

Lato, M., Kemeny, J., Harrap, R., and Bevan, G. (2013). Rock bench: Establishing a common repository and standards for assessing rockmass characteristics using LiDAR and photogrammetry. *Computers & Geosciences*, 50:106–114.

Lato, M. J., Bevan, G., and Fergusson, M. (2012). Gigapixel Imaging and Photogrammetry: Development of a New Long Range Remote Imaging Technique. *Remote Sensing*, 4(12):3006–3021.

Lato, M. J., Diederichs, M. S., and Hutchinson, D. J. (2010). Bias Correction for View-limited Lidar Scanning of Rock Outcrops for Structural Characterization. *Rock Mechanics and Rock Engineering*, 43(5):615–628.

Lato, M. J. and Vöge, M. (2012). Automated mapping of rock discontinuities in 3D lidar and photogrammetry models. *International Journal of Rock Mechanics and Mining Sciences*, 54:150–158.

Lecomte, I., Thollet, I., Juliussen, H., and Hamran, S. (2008). Advances in Geosciences Using geophysics on a terminal moraine damming a glacial lake : the Flatbre debris flow case , Western Norway. pages 301–307.

Lowe, D. G. (2004). Distinctive Image Features from Scale-Invariant Keypoints. *International Journal of Computer Vision*, 60(2):91–110.

Martín, S., Uzkeda, H., Poblet, J., Bulnes, M., and Rubio, R. (2013). Construction of accurate geological cross-sections along trenches, cliffs and mountain slopes using photogrammetry. *Computers & Geosciences*, 51:90–100.

MathWorks (2014). MathWorks: Image Processing Toolbox.

Mora, P., Baldi, P., Casula, G., Fabris, M., Ghirotti, M., Mazzini, E., and Pesci, A. (2003). Global Positioning Systems and digital photogrammetry for the monitoring of mass movements: application to the Ca' di Malta landslide (northern Apennines, Italy). *Engineering Geology*, 68(1-2):103–121.

Niethammer, U., James, M., Rothmund, S., Travelletti, J., and Joswig, M. (2012). UAV-based remote sensing of the Super-Sauze landslide: Evaluation and results. *Engineering Geology*, 128:2–11.

Nitsche, M., Turowski, J. M., Badoux, A., Rickenmann, D., Kohoutek, T. K., Pauli, M., and Kirchner, J. W. (2013). Range imaging: a new method for high-resolution topographic measurements in small- and medium-scale field sites. *Earth Surface Processes and Landforms*, 38(8):810–825.

Oppikofer, T. (2009). Characterization and monitoring of the Åknes rockslide using terrestrial laser scanning. *Natural Hazards ...*, 3:1003–1019.

Orheim, O. (1970). *Glaciological investigations of Store Supphellebre, West-Norway.* Number 151. Norsk Polarinstitutt.

Pandey, S. N. (1987). *Principles and Applications of Photogeology.* New Age International.

Petley, D., Mantovani, F., Bulmer, M., and Zannoni, a. (2005). The use of surface monitoring data for the interpretation of landslide movement patterns. *Geomorphology*, 66(1-4):133–147.

Petley, D. N. (2004). The evolution of slope failures: mechanisms of rupture propagation. *Natural Hazards and Earth System Science*, 4(1):147–152.

Pierrot-Deseilligny, M. (2013). MicMac, Apero, Pastis and Other Beverages in a Nutshell.

Pierrot-deseilligny, M., Luca, L. D. E., and Remondino, F. (2011). Automated image-based procedures for accurate artifacts 3d modeling and orthoimage generation. *Geoinformatics FCE CTU*, 6:291–299.

Pierrot-Deseilligny, M. and Paparoditis, N. (2006). A multiresolution and optimization-based image matching approach: An application to surface reconstruction from SPOT5-HRS stereo imagery. *Archives of Photogrammetry, ...*

Pierrot-desseilligny, M. and Clery, I. (2008). APERO, an open source bundle adjustment software for automatic calibration and orientation of sets of images . Laboratoire Informatique Paris Descartes , équipe SIP. (snavely).

Pollefeys, M., Vergauwen, M., and Cornelis, K. (2001). Structure and motion from image sequences. *Proc. Conference on . . . .*

Schenk, T. (1997). Towards automatic aerial triangulation. *ISPRS Journal of Photogrammetry and Remote Sensing*, 52(3):110–121.

Schenk, T. (2005). Introduction to photogrammetry. *The Ohio State University, Columbus.*

Snavely, N., Seitz, S. M., and Szeliski, R. (2007). Modeling the World from Internet Photo Collections. *International Journal of Computer Vision*, 80(2):189–210.

Stumpf, A., Malet, J.-P., Kerle, N., Niethammer, U., and Rothmund, S. (2013). Image-based mapping of surface fissures for the investigation of landslide dynamics. *Geomorphology*, 186:12–27.

Tarolli, P. (2014). High-resolution topography for understanding Earth surface processes: Opportunities and challenges. *Geomorphology*, 216:295–312.

Tonon, F. and Kottenstette, J. (2006). Laser and photogrammetric methods for rock face characterization. *Report on a workshop held in Golden, Colorado.*

Travelletti, J. and Malet, J. (2010). Multi-temporal terrestrial photogrammetry for landslide monitoring. *. . . of mountain risks . . .*, pages 1–9.

Trevisani, S., Cavalli, M., and Marchi, L. (2009). Variogram maps from LiDAR data as fingerprints of surface morphology on scree slopes. *Natural Hazards and Earth System Science*, 9(1):129–133.

Triggs, B., Mclauchlan, P., Hartley, R., and Fitzgibbon, A. (2000). Bundle Adjustment — A Modern Synthesis 1 Introduction. 34099:1–71.

Turner, D., Lucieer, A., and Watson, C. (2012). An Automated Technique for Generating Georectified Mosaics from Ultra-High Resolution Unmanned Aerial Vehicle (UAV) Imagery, Based on Structure from Motion (SfM) Point Clouds. *Remote Sensing*, 4(12):1392–1410.

Varnes, D. (1984). Landslide hazard zonation: a review of principles and practice.

Verdú, J. M., Batalla, R. J., and Martínez-Casasnovas, J. a. (2005). High-resolution grain-size characterisation of gravel bars using imagery analysis and geo-statistics. *Geomorphology*, 72(1-4):73–93.

Westen, C., Asch, T., and Soeters, R. (2005). Landslide hazard and risk zonation—why is it still so difficult? *Bulletin of Engineering Geology and the Environment*, 65(2):167–184.

Wieczorek, G. and Snyder, J. (2009). Monitoring slope movements. *Geololgical Monitoring*, (11):245–271.

Wolter, A., Stead, D., and Clague, J. J. (2014). A morphologic characterisation of the 1963 Vajont Slide, Italy, using long-range terrestrial photogrammetry. *Geomorphology*, 206:147–164.

Xu, Q., Yuan, Y., Zeng, Y., and Hack, R. (2011). Some new pre-warning criteria for creep slope failure. *Science China Technological Sciences*, 54(S1):210–220.

Yen, T.-J. (2003). *A Qualitative Profile-based Approach to Edge Detection by Ting-jen Yen*. PhD thesis.